UCLouvain

École polytechnique de Louvain

Numerical simulation of a supersonic ejector: influence of the geometry and study of a transient scenario

Author: **Alexandre SOENEN**
Supervisors: **Yann BARTOSIEWICZ, Matthieu DUPONCHEEL, Grégoire WINCKELMANS**
Readers: **Romain DEBROEYER, Philippe CHATELAIN**
Academic year 2020–2021
Master [120] in Mechanical Engineering

Acknowledgements

Completing a master thesis is primarily seen as an individual process. But this work cannot be carried out without being well surrounded. This is the reason why I want to thank all the people who helped me to come to the end of this unique adventure.

Firstly, I would like to express my deepest appreciation to Prof. Yann Bartosiewicz for supervising me in this study and for making this master thesis possible. I want to thank him for his involvement, his continuous support and his encouragement throughout the all work. His expertise in this field, as well as his scientific publications for more than twenty years, have been a great help. I want also to thank my two other supervisors - Prof. Grégoire Winckelmans and Prof. Matthieu Duponcheel - for their availability, their constructive comments and their attentive listening during the endless presentations; without their guidance and persistent help, this dissertation would not have been possible. I would like to thank these members of the jury for taking the time to read this document and for providing a critical opinion.

In addition, I want also thank Prof. Philippe Chatelain for his availability and for accepting to be one of the readers of this master thesis.

I especially want to thank Romain Debroeyer for his wise advice when I was lost and confused in my work. All our discussions put me back on the right path and helped me find motivation in the slower moments. I am very grateful for his time devoted to me, for his availability and for his reactivity. I wish him the best for his PhD and his professional life.

I want to express my gratitude to Aidan Wimshurst for his knowledge sharing in numerical simulation and its rules of good practice. I also thank Prof. Rajesh Bhaskaran, for his explanatory tutorials while I was discovering the simulation tool. Thanks to them for their work and their valuable time.

Even though they were not directly involved in my study activities, the support of the other engineering students contributed greatly to complete this thesis. Their sharing of tips and knowledge was of great help in writing this master thesis and in searching for documentation.

Last but not least, I warmly thank my fantastic parents, my sister and my brother for their unconditional support from the first to the last day of my studies. I could never have done it without them.

Abstract

The purpose of supersonic ejectors consists in the mixing of two fluids with different stagnation pressures in order to obtain a fluid at an intermediate pressure. These passive devices have been widely used at the beginning of the last century for steam locomotives and in refrigeration cycles. Nowadays, even if some domains are less promising than others, the future of the supersonic ejector is not compromised due to the large range of applications, notably in power stations, in the food industry or in aerospace engineering.

For more than twenty years, many efforts have been made to characterize the mixing mechanisms at play in such devices. Hence, a better understanding of these flow phenomena is necessary in order to identify the limitations of the ejector and the potential improvements. In 2018, the research of Lamberts et al. [29] greatly improved the scientific understanding of mixing and choking phenomena within supersonic ejectors. In particular, they developed an original exergy based approach to investigate the exchange between both streams, and a compound-choking theory to predict the performance of the ejector. This master thesis is a continuation of their work and aims to adapt their analysis to the axisymmetric case. The objective is to compare it to the rectangular case of Lamberts et al. [29] and investigate the influence of the geometry using 2D RANS numerical simulations. To the author's knowledge, such analysis has never been proposed before. Based on the results, an improved axisymmetric ejector was presented with better performance.

Moreover, few studies on transient phenomena have been carried out, and this thesis constitutes a first approach in the field of unsteady flows. Many transient scenarios are possible, but this paper focuses on the valve closure at the secondary inlet. This study case is directly related to the vacuum generator, in the high-altitude test facilities. In this work, two operating modes have been identified: the *un-started* mode and the *started* mode, as well as an optimal vacuum performance. Depending on the mode, the transient scenarios differ in time response, flow structure and evacuation performance.

Nomenclature

Abbreviations

AR	Aspect ratio	[–]
CFD	Computational Fluid Dynamics	
CFL	Courant-Friedrichs-Lewy	[–]
COP	Coefficient of performance	[–]
EP	Evacuation performance	[–]
ER	Entrainment ratio	[–]
ERS	Ejector refrigeration systems	
FMG	Full multi-grid	
HAT	High-altitude test	
NXP	Nozzle exit plane	[m]
RANS	Reynolds-Averaged Navier-Stokes	
RNG	Re-Normalisation Group	
RSM	Reynolds Stress model	
SST	Shear Stress Transport	

Alpha numeric symbols

$\dot{m}$	Mass flow rate	[kg/s]
$\mathbf{q}$	Heat flux vector field	[J/(m$^2\cdot$ s)]
$\mathbf{v}$	Velocity vector field	[m/s]

A	Cross-sectional area	[m^2]
A^*	Cross-sectional area set by chocked condition	[m^2]
A_1	Cross-sectional area of the exit of the primary nozzle	[m^2]
A_m	Cross-sectional area of the mixing duct	[m^2]
A_o	Cross-sectional area of the outlet	[m^2]
A_t	Cross-sectional area of the throat of the primary nozzle	[m^2]
c_p	Heat capacity at constant pressure	[$J/(kg \cdot K)$]
e	Specific internal energy	[J/kg]
e_t	Specific total energy	[J/kg]
h	Specific static enthalpy	[J/kg]
H_1	Height of the exit of the primary nozzle	[m]
H_m	Height of the mixing duct	[m]
H_t	Height of the throat of the primary nozzle	[m]
h_t	Specific total enthalpy	[J/kg]
k	Specific turbulence kinetic energy	[J/kg]
M	Mach number	[–]
M_{eq}	Equivalent Mach number of the compound-choking theory	[–]
p	Static pressure	[Pa]
p^*_{out}	Critical back pressure	[Pa]
Q	Heat flux	[W/m^2]
R	Specific gas constant	[$J/(kg \cdot K)$]
s	Specific entropy	[$J/(kg \cdot K)$]
T	Static temperature	[K]
x	Horizontal/axial coordinate	[m]

x_c	Axial coordinate corresponding to $M_{eq} = 1$	[m]
y	Vertical/radial coordinate	[m]
y^+	Dimensionless wall distance	[–]

Greek letters

β	Compound-flow indication	[m^2]
δ	Relative error	[%]
ϵ	Turbulent kinetic energy dissipation rate	[m$^2/s^3$]
γ	Specific heat ratio	[–]
κ	Thermal conductivity	[W/(m $\cdot$ K)]
μ	Molecular viscosity	[Pa $\cdot$ s]
ω	Specific turbulence dissipation rate	[1/s]
ρ	Density	[kg/m^3]
τ	Viscous stress tensor	[Pa]
θ	Absolute deviation	[%]

Operators

$\bar{\cdot}$	Time average
$\hat{\cdot}$	Density-weighted (or Favre) average
$\cdot'$	Fluctuating quantity of time average
$\cdot''$	Fluctuating quantity of the density-weighted average

Subscripts

0	Reservoir conditions
1	Index associated to the primary stream
2	Index associated to the secondary stream
exp	Experimental value

mixing	Associated to the mixing duct
out	Associated to the outlet of the ejector
ref	Reference conditions
wall	Associated to the exterior wall

Contents

Chapter 1

Introduction

1.1 Context

Supersonic ejectors are engineering devices used to entrain and compress a fluid stream. They appeared for the first time in the steam locomotives at the beginning of the last century. Indeed, this jet device works as a pipe blast. The ejector directs the exhaust steam though a nozzle in order to reduce the flue gas pressure and increase the draught on the fire. This slight improvement significantly increased the locomotive power. From that point onward, considerable attention is being paid to this jet device and much effort has been devoted to optimize its performance. Nowadays, the use of ejectors have been extended to other applications, such as in power plants to remove non-condensable gases, in propulsion as thrust boosters, in refrigeration cycles to mix the streams, in boiling nuclear reactors to circulate the coolant... Whatever the application, the physical principle is rather simple and similar: a primary fluid at high pressure and temperature is accelerated into a nozzle to convert its pressure/thermal energy into kinetic energy. This high velocity jet exhausting this primary nozzle entrains a secondary stream to a higher pressure. In contrast to other fluid machinery, the ejectors present many advantages like no moving parts, no direct mechanical energy input and less maintenance requirements. Because of its simplicity and efficiency, this jet device made traditional pumps obsolete.

Another fundamental field of usage for ejectors was found in the steam refrigeration system. The idea was to use the ejector to produce a low-pressure reservoir in which water could be evaporated and subtract heat at low temperature. From 1910 to the early 1930s, steam jet refrigeration systems were successful. Despite a promising start, these applications almost disappeared when the first synthetic refrigerants were introduced during the 1930s. A few decades later, the increase in refrigeration demand and the rise in awareness of ozone depletion in 1974 prompted research toward new and environmentally safe technologies. As a result, ejector refrigeration systems have seen a resurgence of interest. However, this system presented a lower thermodynamic efficiency and need to be optimized. Nowadays, even if some domains are less promising than others, the future of the supersonic ejector is not compromised due to the large range of applications. One recent example is the use of ejectors to create vacuum condition in high-altitude test facilities (HAT), for testing upper stage rocket motors. Indeed, the conventional method of using vacuum pumps may not provide the required vacuum level due to the enormous mass flux ejected by the rocket motor. Maintaining a low vacuum pressure remains a challenging task for the engineer, and the supersonic ejector represents an encouraging solution.

From the 2000s onwards, the number of scientific publications on supersonic ejectors has steadily grown over the years. The main reason lies in the democratization of the computer simulation, which contributes significantly to the understanding of the flow phenomena in supersonic ejectors. Nevertheless, some fundamental issues are still unresolved, and this master thesis aims to fill the knowledge gap in some areas. Indeed, due to the constant change of application, further results are expected. At present, since the supersonic ejector is most often found in refrigeration systems, this field of application will be studied in more detail in this manuscript.

1.2 Ejectors in a refrigeration system

One of the most promising applications is the use of supersonic ejectors as a fluid-driven compressor in an ejector refrigeration system (ERS), shown in Fig. 1.1. In this system, the primary fluid (top cycle) is first heated up in a generator (or boiler). The secondary fluid (bottom cycle) is vaporized at low pressure in an evaporator in order to extract the refrigeration effect. Subsequently, the primary fluid (1) and secondary fluid (2) mix within the ejector and is sent to the condenser (3). After this operation, once in the liquid state, the fluid is divided into two flows: the first goes to the evaporator through an expansion valve (4), and the second is pumped back toward the generator (5). Although the mechanical energy is saved by replacing the pump with an ejector between the evaporator/condenser, the development of such systems is limited due to the efficiency and instability of the ejector.

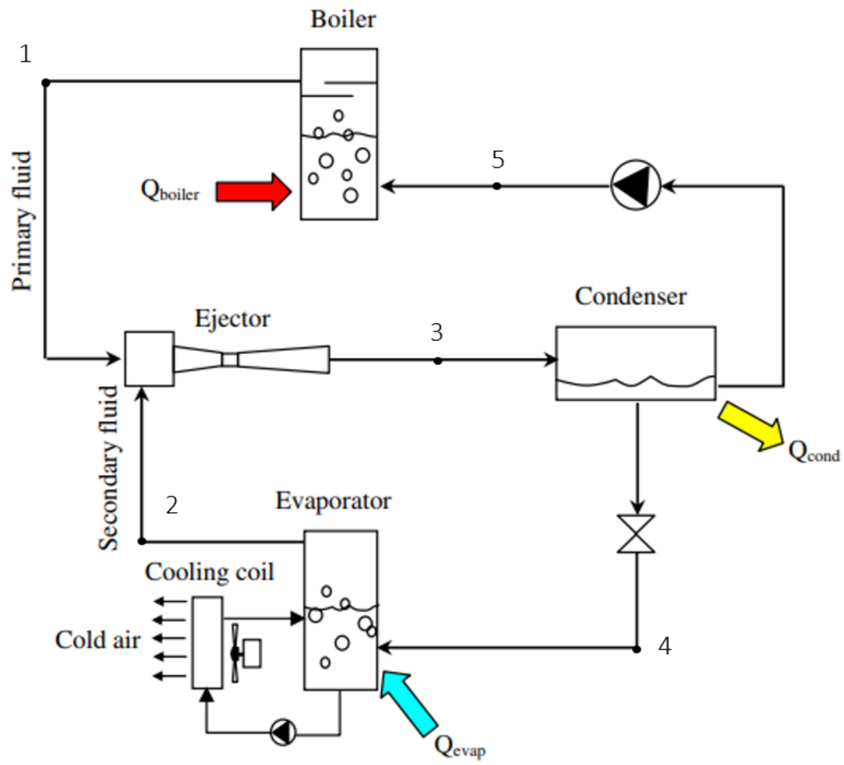

Figure 1.1: A schematic view of a steam jet refrigeration cycle [38].

These ejector refrigeration systems are a promising alternative to compressor-based technologies due to its mechanical simplicity, the limited maintenance needs, low operation cost and no refrigerant limitations. However, the low coefficient of performance (COP) does not allow competing with the vapour-compressor cycle. Since this coefficient is highly related to the ejector behaviour, its optimization must be properly studied. Indeed, the performance of the ERS cycle is written as

$$COP = \frac{\dot{Q}_{evap}}{\dot{Q}_{boiler} + \dot{W}_{pump}} = \frac{\dot{m}_2}{\dot{m}_1}\frac{h_2 - h_4}{h_1 - h_5} \tag{1.1}$$

where $\dot{Q}_{evap}$ is the evaporator power, $\dot{Q}_{boiler}$ the motive heat power in the boiler, and $\dot{W}_{pump}$ the generator feed pump power.

In order to improve the refrigeration system, its performance is related to the mass flow ratio $\dot{m}_2/\dot{m}_1$ and the enthalpy differences $(h_2 - h_4)$ and $(h_1 - h_5)$. These differences depend directly on the fluid and operating conditions. Therefore, for a fixed fluid and working conditions, the global performance depend mainly on the entrainment ratio and its precise estimation for different boundary conditions, is of fundamental importance. This ratio is linked to the supersonic ejector and its phenomena inside.

1.3 Ejector Phenomena

Although the supersonic ejector is a simple device, its internal working principle is more complex. The typical layout of a supersonic ejector is shown on Fig. 1.2. The primary (or motive) flow is fed through a primary nozzle (in red), which is shaped as a converging/diverging duct in order to accommodate a supersonic flow at the exit. The secondary (or suction) flow is fed thought the secondary inlet (in blue) that surrounds the primary nozzle. At the exit of the primary nozzle, the two streams come into contact and mix within the mixing chamber/duct (in orange). Their velocities are highly different and hence, a transfer of momentum accelerates the secondary flow and decelerates the primary flow. As the primary flow is supersonic, a sequence of oblique shocks appears along the mixing zone, undergoing multiple reflections. Subsequently, the mixed stream decelerated in a supersonic diffuser (in orange) in order to convert its kinetic energy and reach the outlet pressure, an intermediate pressure between the primary and secondary inlet pressure.

As shown on Fig. 1.2, the supersonic ejector consists of two inlet channels including a primary nozzle, a mixing duct and a diffuser. The indices 1 and 2 refer to the primary stream and secondary stream, respectively.

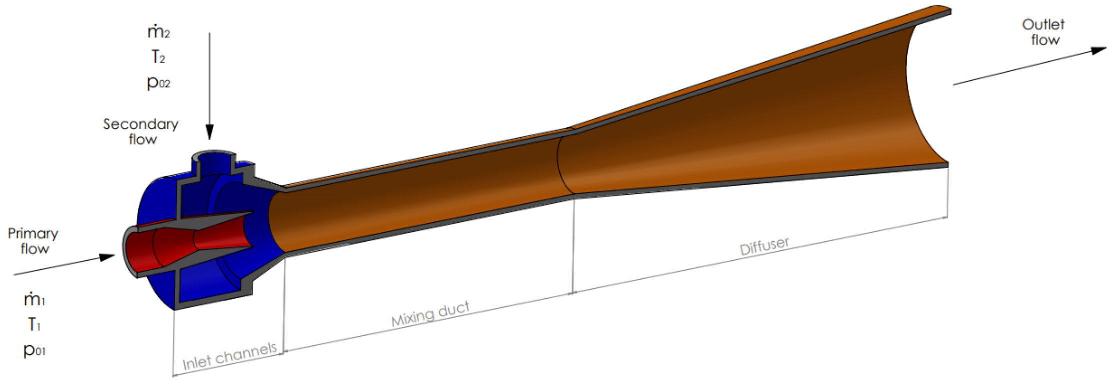

Figure 1.2: Typical layout of a supersonic ejector

Contrary to the other fluid machinery, the supersonic ejector have many advantages like no moving part and no direct transmission of mechanical work. Flow energy is transmitted directly through the two streams, which avoids rotating blades, bearing, lubrication and therefore requires less maintenance.

Obviously, the interaction between the flows at different velocities induces some limitations and specific losses. Indeed, in the diffuser, the supersonic flow decelerates to subsonic velocity through a second shock train. Ideally, the velocity should decrease continuously but in practice, a shock take place in the diffuser. In this condition, the ejector flow rates are insensitive to any increase in the outlet pressure. When the outlet pressure increases, the shock moves towards the inlet side of the ejector, in the mixing duct. The ejector works in a stable condition as far as the shock is located in the mixing duct. As the chock reaches the inlet of the mixing duct, the ejector experiences its best performance. However, beyond a critical outlet pressure, the flow becomes subsonic, and the mass flow rate becomes dependent on downstream condition. The ejector is unstable, decreasing the performance, which in most applications, is not recommended.

At this stage, different global parameters have already been introduced and may be defined : the entrainment ratio $ER = \dot{m}_2/\dot{m}_1$, the ratio between the secondary ($\dot{m}_2$), and the primary ($\dot{m}_1$) mass flow rates and the compression ratio p_{out}/p_{02}, the ratio between the outlet (p_{out}) and secondary (p_{02}) pressure. The aforementioned operating mode can be quantified using these two ratios. As a result, the performance of a supersonic ejector is usually presented by a characteristic curves which represents the evolution of the entrainment ratio versus the compression ratio, as shown in Fig. 1.3.

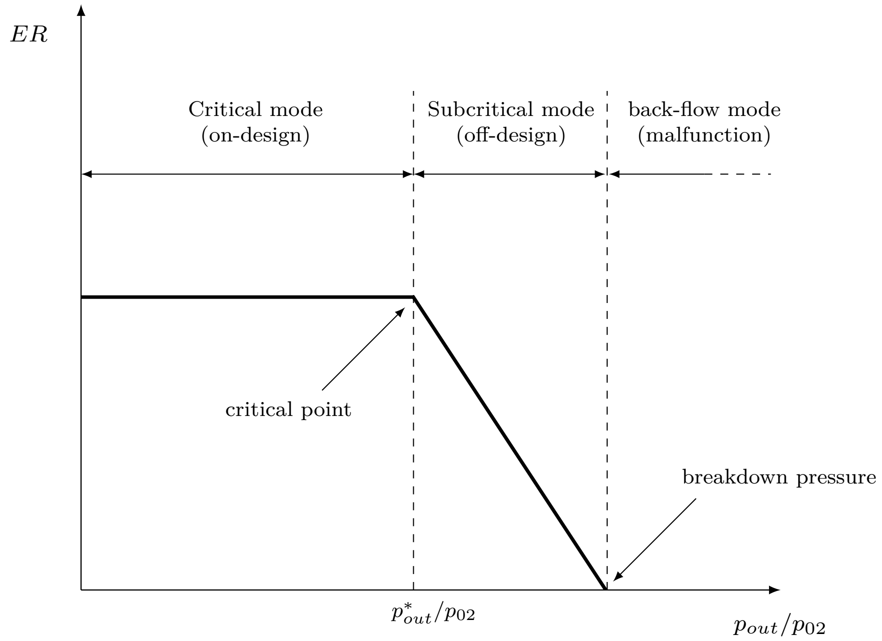

Figure 1.3: Typical characteristic curve of a supersonic ejector

For a given combination of primary and secondary conditions, different modes can be distinguished. The characteristic curve has a first horizontal part and a second sharply decreasing part. The critical point, the so-called critical back pressure, p^*_{out}, conjugates the maximum entrainment ratio with the maximum compression ratio. As shown in Fig. 1.3, three operational modes can be differentiated :

- **The critical mode**: for a certain range of the back pressure, both flows are choked within the mixing duct or within the diffuser. The entrainment ratio remains constant. The ejector flow rates are insensitive to any change downstream the flow and depends only on the inlet conditions. The ejector is said to operate in on-design condition.

- **The subcritical mode**: beyond a certain critical back pressure, the mixing flow unchokes and becomes sensitive to outlet conditions. The entrainment ratio decreases rapidly until it reaches zero, where the back pressure equals a breakdown value. Between the critical and the breakdown pressure, the ejector is said to operate in off-design condition.

- **The back-flow mode**: The ejector starts malfunctioning, which means that a further increase of the back pressure may cause backflow to appear at the secondary inlet. The secondary flow is no more entrained by the primary flow within the ejector.

In summary, the performance of a supersonic ejector is unrelated to the outlet boundary conditions until a critical point, p^*_{out}. A precise estimation of this value is necessary to determine the different operational mode, and at large scale, the coefficient of performance of the refrigeration system. Due to a lack of understanding of the complex flow phenomena at play within the ejector, the estimation of the entrainment ratio and the critical back-pressure is complicated, and the mathematical model is not efficient. Indeed, the modelling of mixing phenomena by equations remains a difficult task. For this reason, numerical simulations based on Computational Fluid Dynamics (CFD) have been used by many authors for predicting the behaviour of the supersonic ejector under varying operating conditions and/or geometries.

1.4 Literature survey

1.4.1 Computational Fluid Dynamics

From the 2000s onwards, the number of publications involving Computational Fluid Dynamic (CFD) approach for supersonic ejectors, has steadily grown over the years. As usual, when a computational method is applied, an initial validation is needed to verify the correspondence between the experiments and the numerical simulations. At that time, the literature survey has revealed that in many cases, the CFD models are validated using global parameters. The authors validated their model with the entrainment ratio [3, 37, 45, 42, 38] and the relative error (δ) of the entrainment ratio is computed to quantify the CFD/model accuracy:

$$\delta = \frac{|ER_{CFD} - ER_{exp}|}{ER_{exp}} \tag{1.2}$$

Unfortunately, Hemidi et al. [20] demonstrated that the validation of a global performance parameter, such as the entrainment ratio, is not sufficient for a correct assessment, even tough a wide range of operational condition is tried out. Indeed, different local flow phenomena can obtain the same entrainment ratio. Therefore, an absolute deviation (θ) involving the N local-quantities ϕ (i.e., wall static pressure profiles) is introduced to validate the model.

$$\theta = \frac{1}{N}\sum_{i=1}^{N} \frac{|\phi_{CFD,i} - \phi_{exp,i}|}{\phi_{exp,i}} \tag{1.3}$$

δ and θ have been selected to comply to the convention proposed by Besagni et al. [6].

Concerning the turbulence modelling, the Reynolds Averaged Navier-Stokes (RANS) approach is generally the method used. Many authors have shown that the choice of the turbulence approach has a large sensitivity depending on the ejector operations. In 2005, Bartosiewicz et al. [4] compared for the first time the performance of six RANS models (k-ϵ *Standard*, k-ϵ *Realizable*, k-ϵ *RNG*, k-ω *Standard*, k-ω *SST*, *RSM* — air) in order to obtain the most suitable turbulence model. The conclusion was that k-ϵ *RNG* and k-ω *SST* models were the best suited to predict the shock phase, strength, and mean line of pressure recovery; in particular, k-ω *SST* showed better performances in terms of stream mixing. In 2009, Hemidi et al. [20] (k-ϵ *Standard*, k-ω *SST* — air) found that k-ϵ *Standard* provided best result ($\delta < 10\%$) especially for the on-design conditions than the k-ω *SST* ($\delta = 10-20\%$). Furthermore, it has been highlighted that for exactly the same entrainment ratio prediction, both models could provide very different local flow structures. In 2015, Del Valle et al. [17] (k-ϵ *Standard*, k-ϵ *Realizable*, k-ϵ *RNG*, k-ω *SST*, *RSM* — R134a) investigated the performance of a R134-a ejector. k-ω *SST* was found to be the most accurate model ($\delta = 15.2\%; \theta = 5.5\%$) which slightly superior to Zhu et al. [45] and Sriveerakul et al. [42] ($\delta < \pm 10\%$). Nevertheless, Del Valle et al. obtained a lower average deviation with the $k - \epsilon$ *Standard* ($\delta = 19.9\%; \theta = 4.7\%$). The same year, Mazzelli et al. [32] (k-ϵ *Standard*, k-ϵ *Realizable*, k-ω *SST*, *RSM* — air) concluded that the k-ω *SST* model is generally the best performing whereas ϵ-based models are more accurate at low motive pressure. The next year, in 2016, Croquer et al. [12] (k-ϵ *Standard*, k-ϵ *Realizable*, k-ϵ *RNG*, k-ω *SST* — R134a) studied a 2D axisymmetric R134a ejector et compared to the experimental data of Del Valle et al. [17]. As a result, k-ϵ *Standard* with standard wall functions performs the best, with a relative error of $\delta = 4.3\%$. The advanced version of the $k - \epsilon$ model did not improve the predictions of the entrainment ratio ($\delta > 6\%$). However, $k - \epsilon$ models predict the same normal shock wave, while k-ω *SST* captures the detailed structure of the shock train.

All these studies allow to state that turbulence modelling is not a fully answered question for ejector operation and flow physics predictions. Indeed, different authors applied different methods on different geometry, and a complete validation is missing so far. Besagni et al. [6] close the knowledge gap by assessing the performances of a CFD approach over a wide range of ejectors designs, working fluids and boundary conditions. To this end, the study poses precise guidelines to be applied in future research activities for the mesh criteria, geometrical modelling, solvers and turbulence models. Finally, $k - \omega$ *SST* has shown the best agreement with the experimental measurements concerning both global and local flow quantities, with an average entrainment ratio error of 14% and a maximum of 20%, under on-design operating mode. But in the interested case of air as working fluid, Besagni et al. [6] have obtained this following model validation outcomes: $k - \omega$ *SST*

($\delta_{\text{on-design}} = 1.2\%$, $\delta_{\text{off-design}} = 29.1\%$, $\theta = 14.7\%$) and $k - \epsilon$ *RNG* ($\delta_{\text{on-design}} = 1.1\%$, $\delta_{\text{off-design}} = 26.6\%$, $\theta = 16.3\%$). Both turbulence models have close relative error and absolute deviation. In order to achieve the equivalent CFD accuracy, this proposed guideline is applied in this manuscript.

1.4.2 Geometrical modelling

Concerning to the geometrical modelling, many CFD approaches for supersonic ejectors are mainly two-dimensional, either rectangular or axisymmetric, but it does not reflect the reality. In 2007, Pianthong et al. [37] compared for the first time an axisymmetric and a 3D simulation of a steam ejector. It is shown that the axisymmetric model is quite capable of producing similar results to the three-dimensional model, and both results are in acceptable agreements with the experimental data. Sharifi et al. [39] and Gagan et al. [16] confirmed a few years later the same outcomes and concluded that there is no need to use a full three-dimensional simulation for further studies of axisymmetric ejector. However, in 2015, Mazzelli et al. [32] simulated a two-dimensional and three-dimensional for a rectangular cross-section ejector and obtained significant discrepancies between both models. Good agreement is found across all 2D and 3D models at on-design condition (two-dimensional : $\delta = 2.9\%$; three-dimensional : $\delta = 1.9\%$), while the prediction at off-design condition is only acceptable with 3D models (two-dimensional : $\delta = 42.8\%$; three-dimensional : $\delta = 14.6\%$). These results confirm the importance of wall effects. Nowadays, there are few studies that really addresses in-depth the comparison between rectangular and axisymmetric case. The manuscript aims to close the knowledge gap in this domain.

1.4.3 1D model

Since the 1940s, many authors have tried to develop a 1D model to predict the ejector performances over a large range of operation. The advantage consists on the easy implementation of the 1D model into a system model to predict overall performance of an ejector refrigeration systems.

In 1942, Keenan et al. [25] were the first to present a mathematical model for a constant area mixing ejector (without a diffuser). The purpose of the study was to test the utility and validity of a method of analysis based on ideal gas dynamics and the principles of conservation of mass, momentum, and energy. A few years later, in 1950, the same authors Keenan et al. [26] introduced the concept of a constant pressure mixing ejector and obtained better performance for the analytical model. The mixing was assumed to occur at constant pressure. However, this model could not give detailed information on the choking phenomena. Later, in 1958, Fabri et al.

[15] proposed that the induced secondary stream is assumed to accelerate as it flows along the primary jet and reaches unity Mach number at the section of maximum expansion of the primary flow, as shown on Fig. 1.4. This hypothetical section is so-called “aerodynamic throat”, “effective area” or “critical section”, which limits the secondary mass flow rate. This choking model was called the *Fabri-choking* theory in the literature [14, 27, 30]. In 1977, Munday et al. [33] postulated also a fictive throat and assumed that the mixing process starts beyond the hypothetical throat with uniform pressure. And over the years, the *Fabri-choking* model was always used as the baseline of all state-of-the-art simplifies models to predict the performance of supersonic ejectors. [9, 10, 18, 22, 36, 40, 44]. Authors obtained acceptable average deviations for on design mode ($\delta = 2.6\%$ in [40], $\delta = 7.0\%$ in [18], $\delta = 1.2\%$ in [9]) but failed to predict at subcritical mode ($\delta = 15 - 50\%$ in [40], $\delta = 20.0\%$ in [9]).

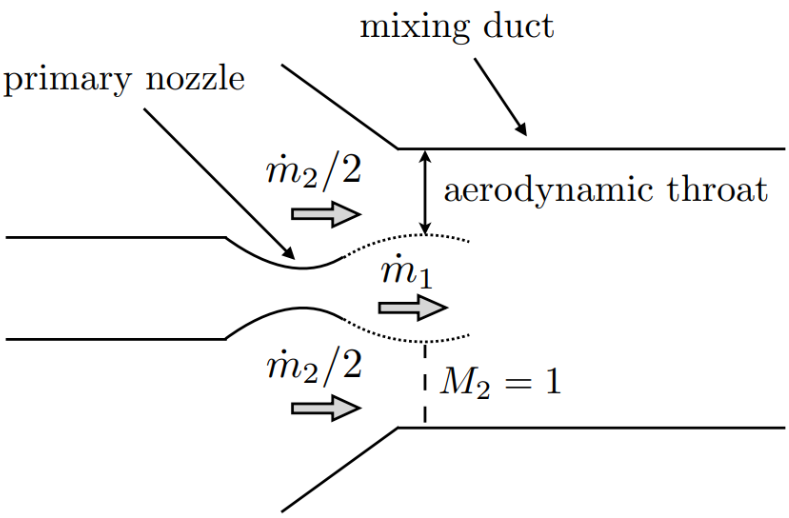

Figure 1.4: Schematic diagram for the model of the Fabri-choking [27].

However, another theory has also emerged since the 1950s. The same year as Fabri et al. [15] (1957), Pearson et al. [35] presented a theory based on a wave velocity argument to predict the nozzle performance. The obtained choked condition showed that when the nozzle jet consists of two non-fixed mixed flows of different total pressure, one flow is supersonic (the one with the greater total pressure) while the other is subsonic. Hoge et al. [21] (1965) achieved an equivalent result. A decade later, Bernstein et al. [5] used this condition to develop a one-dimensional theory for analysing the behaviour of one or more gas streams flowing through a single nozzle. This compound-compressible flow theory shows that the behaviour of each

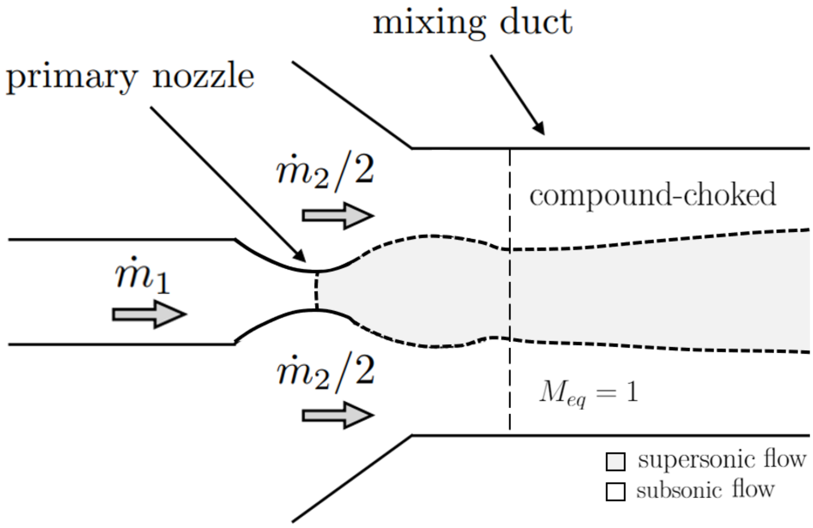

Figure 1.5: Schematic diagram for the model of the Compound-choking.

stream is influenced by the presence of the other streams. It was found that a two-stream compound-compressible nozzle flow may be choked with a subsonic stream if the other one is supersonic, as the combination of the two streams may behave like a sonic stream, know as the *compound-choking* theory. An equivalent Mach number (M_{eq}) is thus defined for the two streams flow. As may be seen on Fig. 1.5, a schematic diagram is presented for the compound-choking model.

Recently, some authors implemented this theory as an explanation of the entrainment limitation in supersonic ejectors. In 2017, Lamberts et al. [28] achieved better performance with the compound-choking theory ($\delta = \pm 10\%$) compared to state-of-art 1D models relying on the *Fabri-choking* assumption. Last year, Croquer et al. [13] achieved the same result (*Compound-choking* theory $\delta = 5.3\%$; *Fabri-choking* theory $\delta = 17.5\%$). This theory become a promising model to explain the flow phenomena in the ejector. In this manuscript, this theory is implemented and studied for an adapted axisymmetric ejector of Lamberts et al. [28].

1.4.4 Transient scenario

As discussed in the previous section, for the 50s past years, authors have been trying to model the behaviour of a supersonic ejector in a stationary mode using mathematical model and later CFD methods. However, the author of the present manuscript did not find comprehensive studies referring to the transient mode. Indeed, authors are mainly interested in the stationary mode of the ejector.

In 2008, Park et al. [34] numerically investigated the starting and terminating transients of a small-scale high-altitude test (HAT) facility to simulate vacuum ignition tests of rocket motors. They investigated in detail the effects of diffuser length and pre-evacuation state, but not the flow mechanism associated with the transient process. The year after, Lijo et al. [31] analysed the transient flow through the vacuum ejector system with limited mass supply from the secondary chamber. The results obtained showed that the one and only condition in which a continuous mass entrainment can be possible in such types of ejectors is the generation of a recirculation zone near the primary nozzle exit. In 2011, Du Clou et al. [11] proposed the first analytical model to optimize the ejector geometry and the unsteady performance. The authors highlighted that the performance model did not include the mixing of the transient primary and secondary stream, due to the lack of one-dimensional theory at this time. A few years later, Jafarian [23] investigated for the first time transient phenomena with a linear variation of the primary flow pressure. The results showed that as the slope of the motive flow pressure profile increases as much as twice, the secondary flow rate increases by 40%. Unfortunately, the poor explanation of the numerical simulation, the high transient time step of 1.0 [ms] and 1.5 [ms] as well as the single global validation requires a critical opinion on their results. Recently, Arun et al. [2] studied the effect of geometric configuration on the starting transients in vacuum ejector. The focus was mainly put on the various geometric ratio. After a net increase in primary pressure, the secondary pressure decreases and the authors showed up that a rapid evacuation happens when the initial recirculation bubble splits up. In 2018, Karthick et al. [24] studied only experimentally the ejector behaviour by varying the secondary flow rate. Their results and schlieren images could be used for further validation.

Last year, Bharate et al. [8] improved considerably the understanding of the starting transients in second throat vacuum ejectors. Its extensive study allowed to accurately describe the flow mechanism in the transient mode. Indeed, the authors characterized the vacuum generation with four distinct stages : gradual evacuation process, transition region, rapid evacuation and gradual evacuation This study will be a good basis for this manuscript. Over the 10 last years, a few authors investigated the transient scenarios and more precisely the vacuum ejector scenario due to the interest in HAT facilities. However, there is actually no study related to the other scenario : increasing of the outlet pressure, decreasing of the primary inlet pressure, and even less an analytical model. This manuscript tries to close the knowledge gap for one of the other scenario.

1.5 Research issues and objectives

The literature review shows an increasing improvement in understanding of both mixing and the choking phenomena taking place in supersonic ejector. Nowadays, new methodologies provide a better estimate for the characteristic curve, such as the *compound-choking* theory. Nevertheless, a fundamental issue is still unresolved, already raised previously :

- The comparison between a rectangular and axisymmetric ejector.
- The analysis of transient scenarios.

At the present time, few literature provides numerical and experimental data on these subjects. Research efforts over the past ten years have focused mainly on the stationary case. Therefore, this thesis aims at gaining insights into these domains for supersonic axisymmetric ejector.

The first goal of this thesis is to provide better understanding of the supersonic axisymmetric ejector and its difference with the rectangular supersonic ejector. Hence, numerical results are thoroughly analysed and compared to investigate the reason of their difference. These results highlight the importance of quantifying and locating transfers and irreversibility. Since the *compound-choking* theory is a promising 1D model to explain the flow phenomena in the ejector, it is interesting to examine its ability to predict the mode of operation depending on the geometry: rectangular or axisymmetric.

The second objectives consist of the development and the analysis of a rapid change at the ejector boundaries. As evidenced by the literature survey, the transient results for supersonic ejector are still unknown in the scientific paper. Therefore, this thesis is a first approach in this unsteady flow study area. In this paper, one transient scenario is highlighted: decreasing of the secondary mass flow. This case studies were inspired by the industrial world, which has an interest in these results. Indeed, the decrease in the secondary mass can be related to a valve closure. In the high-altitude test facilities (HAT), this scenario is very similar to a vacuum generator, and the obtained results in this manuscript can be extended to this application.

1.6 Structure of the manuscript

In order to achieve the objectives, the manuscripts are divided into 3 chapters:

- **Chapter 2 : Methodology**

  This chapter is devoted to a thorough description of the methodology and the numerical methods. First, the focus is put on the adaptation of a rectangular supersonic ejector into an axisymmetric supersonic ejector. This new axisymmetric geometry maintains lengths and area ratios, allowing to compare it to the rectangular case, developed in the Chapter 3. Secondly, the numerical methods are presented in detail from the RANS equations to the flow solver and to the study of the computational domain. In this section, the fluids properties and the turbulence model are described in depth, as well as the boundary conditions. The last section is devoted to the verification of the numerical simulation.

- **Chapter 3 : Comparison between the rectangular and axisymmetric ejector**

  Chapter 3 is dedicated to the comparison of a rectangular ejector with its complementary axisymmetric ejector and provides an explanation of the difference in the results. In a first step, a comparison on a global and local scale is carried out, as well as with the experimental data of Lamberts et al. [28]. In a second step, the exergy analysis is performed to explain the difference in the characteristic curve. An approach has been proposed to quantify and locate the transfer of exergy and the irreversibility within each ejector. Following this analysis, an improved axisymmetric ejector is presented. Finally, the third section is devoted to the comparison of the two geometries with a 1D model (*compound-choking* theory), including the heating of the primary flow.

- **Chapter 4 : Analysis of 2 transient scenarios**

  In Chapter 4, the focus is on transient scenarios, and more specifically on the closure of the valve at the secondary inlet. It generates a vacuum chamber in the secondary channel, such as in high-altitude test facilities. Before presenting any results, further details are given on the calculation method and an error estimation is made to assess the accuracy of the CFD. In the next sections, the transient results are presented in depth, from the evacuation performance to the response time. Due to the two identified mode of operation (*un-started* and *started* mode), two valve closures have been performed, one in each mode. Finally, the last section is devoted to the comparison of the structure of the flow between the two scenarios.

Chapter 2

Methodology

2.1 Introduction

In this chapter, the methodology and the numerical methods used in this present paper are presented in detail. In the first section, the focus is put on ejector geometries and the adaptation of a rectangular supersonic ejector into an axisymmetric supersonic ejector. The following section is devoted to the numerical methods, including the equations, the fluids properties and the numerical parameterization such that the flow solver, the computational domain and the boundary conditions. Finally, the chapter ends up with the verification and validation of the simulation with the numerical data obtained by Lamberts et al. [27].

2.2 Ejector geometries

2.2.1 Rectangular ejector

The rectangular ejector that has been simulated corresponds to the rectangular ejector of the upgraded experimental setup available at UCL and described in details in Lamberts et al. [29]. This upgraded installation aims to improve the previous setup of Mazzelli et al. [32] that presented one main disadvantage.

The drawback concerns the shape of the primary nozzle. Indeed, the converging-diverging geometry consisted in two inclined plans and due to the sharp throat, strong compression waves propagate downstream leading to a non-uniform flow at the exit of the primary nozzle, as highlighted by Lamberts et al. [29]. Therefore, they applied the method of characteristics to design an upgraded shape for the primary nozzle. This new geometry provides a smooth throat, characterized by a continuous circular arc with a unique radius of curvature, $R = 500.0$ [mm], as shown in Fig. 2.1. The height of the throat remains unchanged, $h_t = 6.0$ [mm] as well as the height of the primary exit nozzle, $h_1 = 8.0$ [mm].

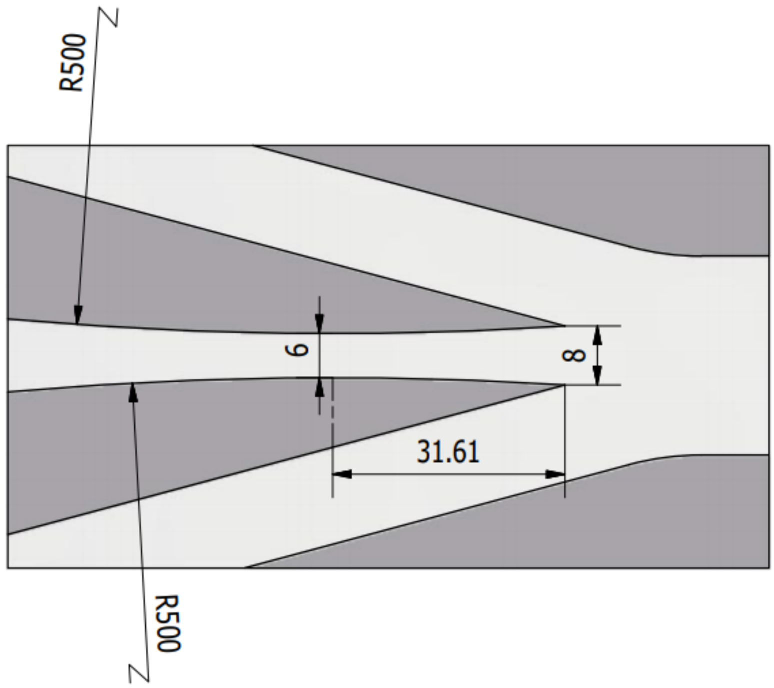

Figure 2.1: Dimensioned drawing of the new primary nozzle geometry. All dimensions are in mm [27].

Regarding the secondary nozzle and the mixing chamber, it has essentially the same geometry as the previous one. Fig. 2.2 shows the dimensioned drawing of this upgraded rectangular ejector used as reference and modelled in the numerical simulations for the rectangular case of the present paper. Instruments for the measurements of the static pressure are also visible at different locations along the wall of the ejector. Indeed, several holes have been drilled in the top wall along the mixing duct and at the entry of the diffuser. However, these small diameter holes are not taken into account in the numerical simulations and the top wall is considered as a flat plane.

2.2.2 Axisymmetric ejector

Concerning the axisymmetric case, the ejector mainly used in the present work is an adaptation of the upgraded rectangular supersonic ejector into an axisymmetric supersonic ejector. This new geometry maintains the lengths and the area ratios as in the rectangular case. The objective is to compare our axisymmetric results

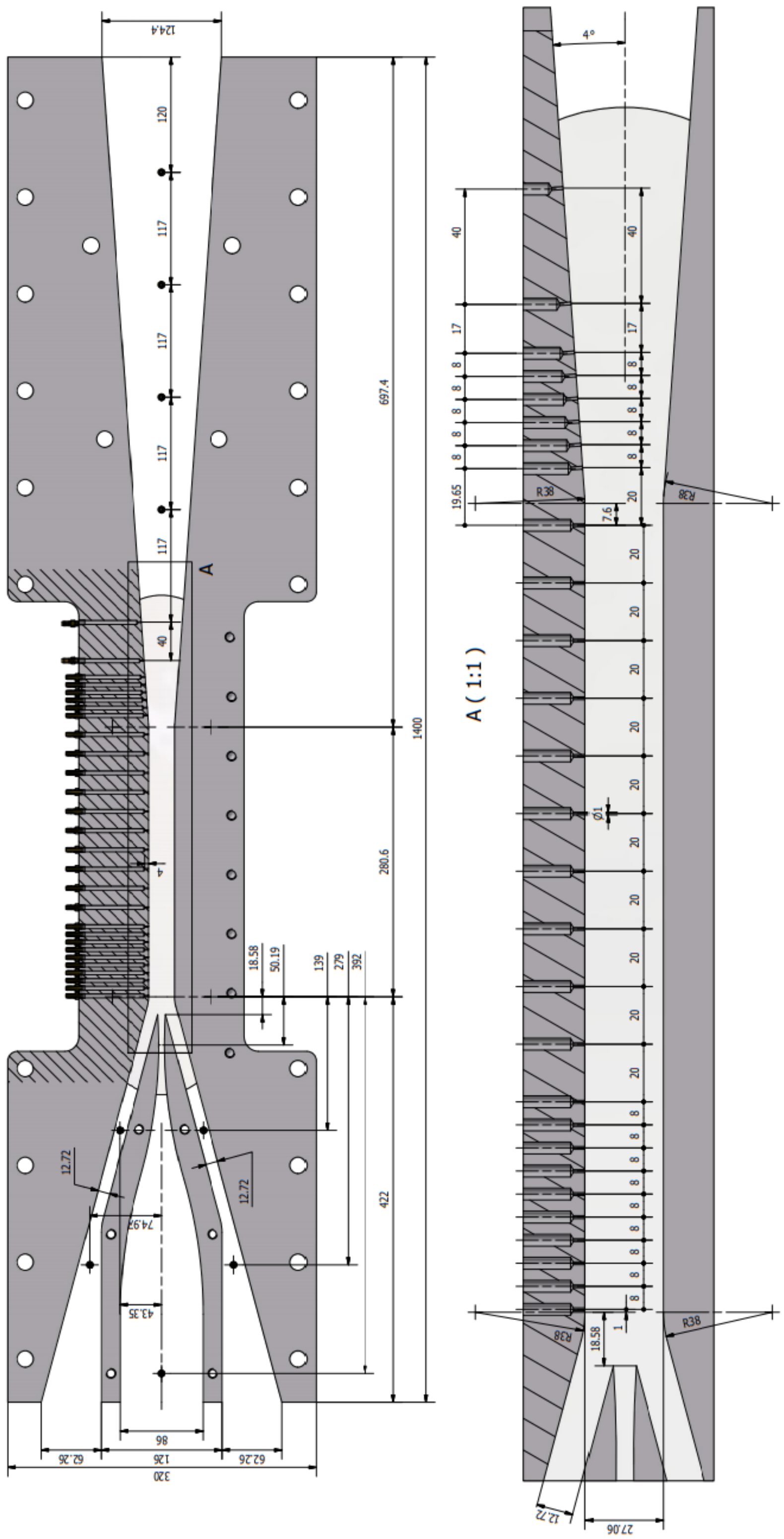

Figure 2.2: Dimensioned drawing of the rectangular ejector used as reference and modelled in the numerical simulations. All dimensions are in mm [27].

with the experimental and numerical data obtained by the upgraded installation of Lamberts et al. [29].

The primary nozzle has a converging-diverging geometry. As may be seen in Fig. 2.3, the radius of the primary nozzle throat, the radius of the primary nozzle exit and the radius of the mixing duct are noted r_t, r_1, and r_m, respectively. The section at this corresponding location is indicated as A_t, A_1 and A_m. The flow being sonic at the throat, the mass flow rate is limited in the primary nozzle. Hence, the section at this point is maintained constant between the two geometries. In the rectangular ejector, the corresponding height is 6.0 [mm] and the cross-section is 50.0 [mm]. By area conservation, $r_t = 9.77$ [mm]. Regarding the two others radius, the values are computed with the area ratios conservation, $A_1/A_t \simeq 1.33$ and $A_m/A_t \simeq 4.51$. The values are written as follows : $r_1 = 11.28$ [mm] and $r_m = 20.75$ [mm]. The cylindrical coordinate system is also shown in Fig. 2.3, as well as its origin, located on the ejector centreline at the entry of the mixing duct.

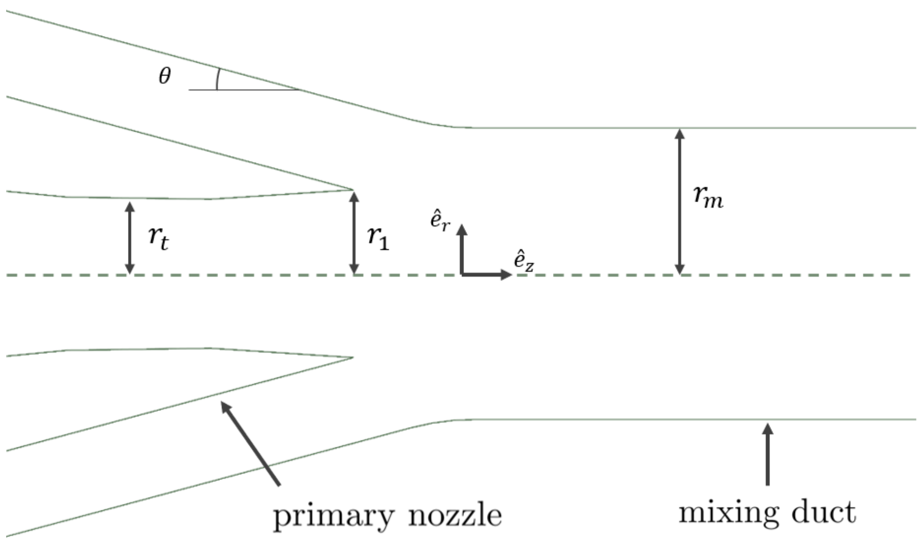

Figure 2.3: Definition of the geometrical parameters

The mixing duct of constant area extends from 0.0 [mm] to 280.6 [mm]. In the divergent part, the outlet diverging angle decreases to the value of 1.95° preserving the same length of the divergent 697.4 [mm] and the same outlet area ratio, $A_o/A_t \simeq 20.74$. Regarding the secondary nozzle, the inlet converging angle, θ, is 15°. The detailed dimensioned drawing of the axisymmetric ejector used in this manuscript is shown in Fig. 2.4. Only one half of the ejector is modelled because of axisymmetric assumptions.

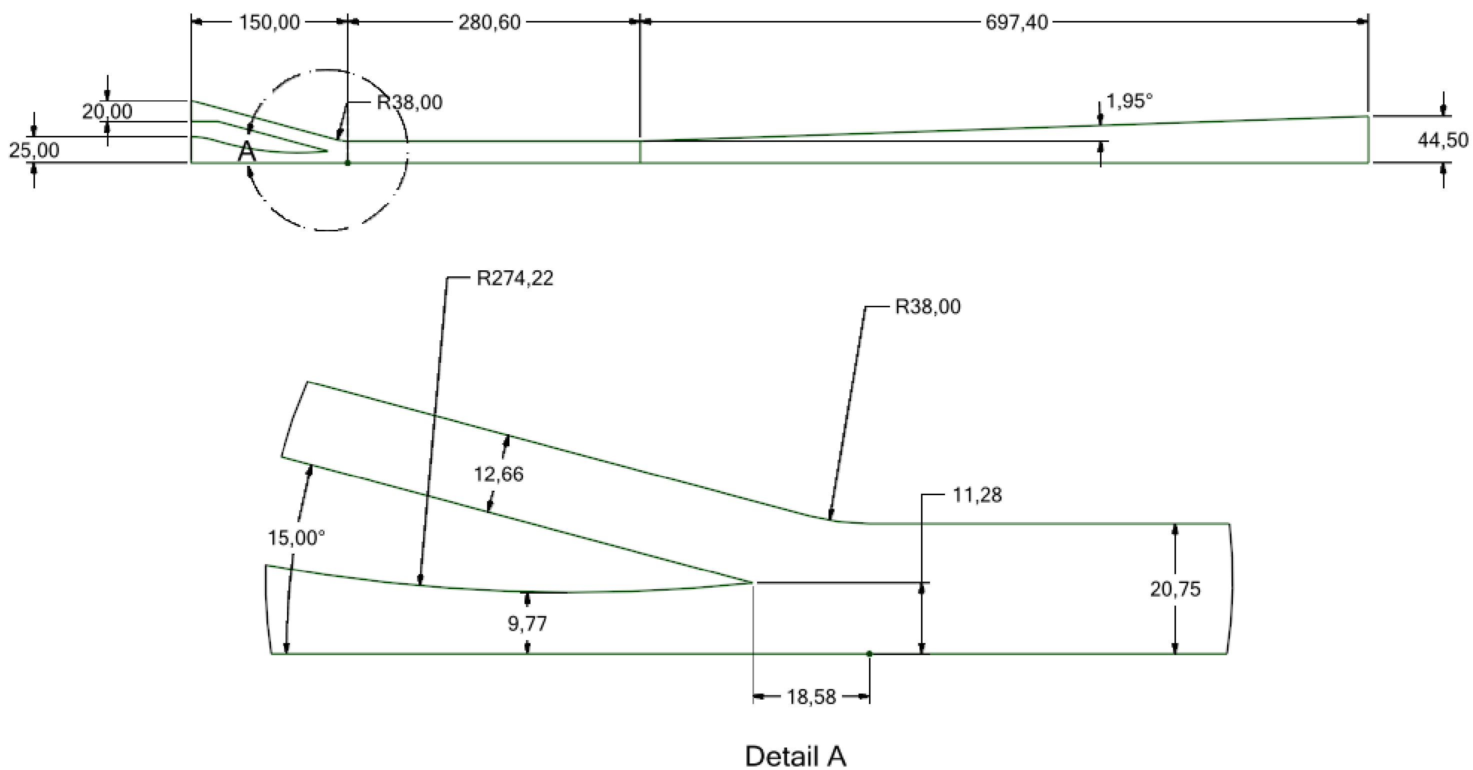

Figure 2.4: Dimensioned drawing of the axisymmetric ejector used throughout the manuscript. All dimensions are in mm.

2.3 Numerical method

2.3.1 Averaged equation

The flow field is simulated by solving the compressible Reynolds-Averaged Navier-Stokes equations (RANS). Depending on the geometry, either 2D axisymmetric or planar equations are used. The conservative form of these averaged equations is written as follows, in the absence of the body force, and for any frame of reference:

$$\frac{\partial \rho}{\partial t} + \nabla \cdot (\overline{\rho}\hat{\mathbf{v}}) = 0 \qquad \text{(mass)} \tag{2.1}$$

$$\frac{\partial}{\partial t}(\overline{\rho}\hat{\mathbf{v}}) + \nabla \cdot (\overline{\rho}\hat{\mathbf{v}}\hat{\mathbf{v}}) = -\nabla\overline{p} + \nabla \cdot (\bar{\boldsymbol{\tau}} + \bar{\boldsymbol{\tau}}^t) \qquad \text{(momentum)} \tag{2.2}$$

$$\begin{aligned}\frac{\partial\left(\bar{\rho}\hat{e}_t\right)}{\partial t} + \nabla \cdot (\hat{\mathbf{v}}\bar{\rho}\hat{h}_t) &= -\nabla \cdot (\bar{\mathbf{q}} + \bar{\mathbf{q}}^t) + \nabla \cdot (\bar{\boldsymbol{\tau}}\hat{\mathbf{v}} + \bar{\boldsymbol{\tau}}^t\hat{\mathbf{v}}) \\ &+ \nabla \cdot (\overline{\boldsymbol{\tau}\mathbf{v}''} - \frac{1}{2}\overline{\rho\mathbf{v}''\mathbf{v}''\mathbf{v}''}) \qquad \text{(energy)}\end{aligned} \tag{2.3}$$

where two methods of averaging are used. According to the concept of Reynolds-averaging, a time dependant quantity ϕ is decomposed into a mean and a fluctuating part such that $\phi = \bar{\phi} + \phi'$. The mean quantity is defined as the conventional time-average value over a time period, $\bar{\phi} = \frac{1}{T}\int_t^{t+T}\phi(t)dt$. While the second averaging method consists in using the density-weighted (or Favre) average by introducing a mass-averaged quantity $\hat{\varphi} = \overline{\rho\varphi}/\bar{\rho}$, where $\bar{\rho}$ represents the Reynolds-averaged density. The corresponding fluctuating quantity is indicated with φ'' such that $\varphi = \hat{\varphi} + \varphi''$.

Most commonly, in the averaged equations, approximations are made for the time-averages of the viscous stress tensor ($\bar{\boldsymbol{\tau}}$) and of the heat flux ($\bar{\mathbf{q}}$):

$$\bar{\boldsymbol{\tau}} \simeq \mu(\hat{T})\left[\left(\nabla\hat{\mathbf{v}} + \nabla\hat{\mathbf{v}}^{\mathrm{T}}\right) - \frac{2}{3}\nabla \cdot \hat{\mathbf{v}}I\right] \tag{2.4}$$

$$\bar{\mathbf{q}} \simeq -\kappa(\hat{T})\nabla\hat{T} \tag{2.5}$$

with μ, κ, the molecular viscosity and the thermal conductivity. The additional term $\bar{\boldsymbol{\tau}}^t$ represents the Reynolds stress tensor. The Boussinesq assumption states that the Reynolds stress tensor is linked to the kinetic energy of the fluctuating turbulent field, $k = \overline{\rho\mathbf{v}''\mathbf{v}''}/2\bar{\rho}$ and can be written in the following way

$$\bar{\boldsymbol{\tau}}^t \simeq \mu_t\left[\left(\nabla\hat{\mathbf{v}} + \nabla\hat{\mathbf{v}}^{\mathrm{T}}\right) - \frac{2}{3}\nabla \cdot \hat{\mathbf{v}}I\right] - \frac{2}{3}\bar{\rho}kI \tag{2.6}$$

with μ_t, the eddy viscosity provided by the turbulence model.

In an analogous way for the averaged equation of energy, the additional turbulent heat flux, given by $\bar{\mathbf{q}}^t = c_p\overline{\rho\mathbf{v}''\mathbf{T}''}$ is modelled simply by taking it to be proportional to the temperature gradient of the mean flow.

$$\bar{\mathbf{q}}^t \simeq -k_t \nabla \hat{T} = -\frac{c_p \mu_t}{\mathrm{Pr}_t} \nabla \hat{T} \tag{2.7}$$

where the turbulent Prandtl number Pr_t is often taken as a constant value, $Pr_t \sim 0.9$ valid for fluid such as air. Moreover, in the averaged energy equation, the quantities $\hat{e}_t$ and $\hat{h}_t$ represent the Favre-averaged specific total energy and total enthalpy of the flow given by:

$$\hat{e}_t = \hat{e} + \frac{\hat{\mathbf{v}}\hat{\mathbf{v}}}{2} + k \tag{2.8}$$

$$\hat{h}_t = \hat{h} + \frac{\hat{\mathbf{v}}\hat{\mathbf{v}}}{2} + k \tag{2.9}$$

where $\hat{\mathbf{v}}\hat{\mathbf{v}}/2$ is called the specific mean-flow kinetic energy, K, and k is defined as the specific kinetic energy of the fluctuating turbulent field. Finally, the contributions of some additional terms are neglected. Simplifications are made by ignoring the molecular diffusion, $\overline{\boldsymbol{\tau}\mathbf{v}''}$ and the turbulent transport of turbulence kinetic energy, $\frac{1}{2}\overline{\rho\mathbf{v}''\mathbf{v}''\mathbf{v}''}$. This approximation is good for flows with supersonic Mach number, which follows from the fact that $k \ll \hat{h}$. From this latter assumption, the $\frac{2}{3}\bar{\rho}kI$ term is generally neglected in the expression of $\bar{\boldsymbol{\tau}}^t$ and the turbulence kinetic energy is often ignored in the calculations of $\hat{e}_t$, $\hat{h}_t$.

2.3.2 Flow solver

The finite volume code Ansys Fluent (Release 2021 - R1) has been used to solve the RANS equations for turbulent compressible flow. As reported by Besagni et al. [6], the $k-\omega$ SST and $k-\epsilon$ RNG models have shown the best agreement to simulate the turbulent behaviour in a supersonic ejector. These models are well known in the literature, and a detailed description of their mathematical structure is not presented in the present paper. For further information about their implementation in the commercial code Ansys Fluent, the reader should refer to [1]. All the considered models have been used in their original implementation without further modifications. Nevertheless, some additional options are selected to take into account the compressibility effects and the viscous heating of our supersonic flow. In this present study, the transient scenario is simulated with the $k-\epsilon$ RNG model due to its fast convergence and its low computational time. While for the stationary case, the $k-\omega$ SST model is recommended and captures a more detailed flow structure than the $k - \epsilon$ RNG.

Regarding the discretization of the governing equations, a second-order upwind numerical schemes have been used for the spatial discretization to limit the numerical diffusion. Second-order schemes are also selected for the turbulence quantities. Gradients are evaluated by the Least Squares approach. A two-step approach is adopted for the initialization : the hybrid initialization and a full multi-grid (FMG) initialization. In Ansys Fluent, density-based and pressure-based algorithms are available. Both solvers are adapted for high-velocity compressible flows. The pressure-based solver with Coupled algorithm has been adopted since it is described in the literature as far more stable than density-based solver. The Coupled algorithm applied solves the continuity and momentum equations simultaneously. The selected pseudo transient option was enabled, which was found to speed up the steady-state solution. Moreover, no Courant-Friedrichs-Lewy (CFL) condition is required to stabilize the solution. The numerical solution is considered converged when the normalized difference of mass flow rates at the inlets and at the outlet were $< 10^{-5}$ on the last 50 iterations. Calculations are also stopped when all residuals are stable and reach a value of at least four orders of magnitude less than the initial value.

2.3.3 Computational domain

For both geometries, the mesh generation process has been handled with Ansys Fluent tools. Depending on the study case, the grid structure of numerical domain differs from the turbulence model. Indeed, for the $k - \omega$ SST model (stationary case), the flow is wall-resolved and a fine mesh is required to resolve the viscous sub-layer ($y^+ < 1$). While the $k - \epsilon$ RNG model (transient scenario) requires a near wall modelling (i.e. Enhanced Wall treatment in this simulation) and the first grid cell need to be in the region of $30 < y^+ < 300$. As shown in Fig. 2.5 and Fig. 2.6, the grid structures of the numerical domain are structured. Two geometrical parameters are identified to characterize each mesh fully : (i) the vertical/radial parameter is the mixing chamber cell throat size, expressed as the number of cells in the mixing chamber, (ii) the horizontal/axial parameter is the aspect ratio of the cells (AR). The Table 2.1 resumes the mesh structure details for each study case.

The independence of the results from the grid density has been performed by comparing the profile of the Mach number on the axis of the ejector for the meshes described above and a refined mesh. The finer meshes were obtained by further refinement only in the axial direction, yielding a mesh of approximately 350,000 cells for the $k - \omega$ SST case and a mesh of approximately 100,000 cells for the $k - \epsilon$ RNG case. As may be seen in Figs. 2.7 and 2.8, the differences between both

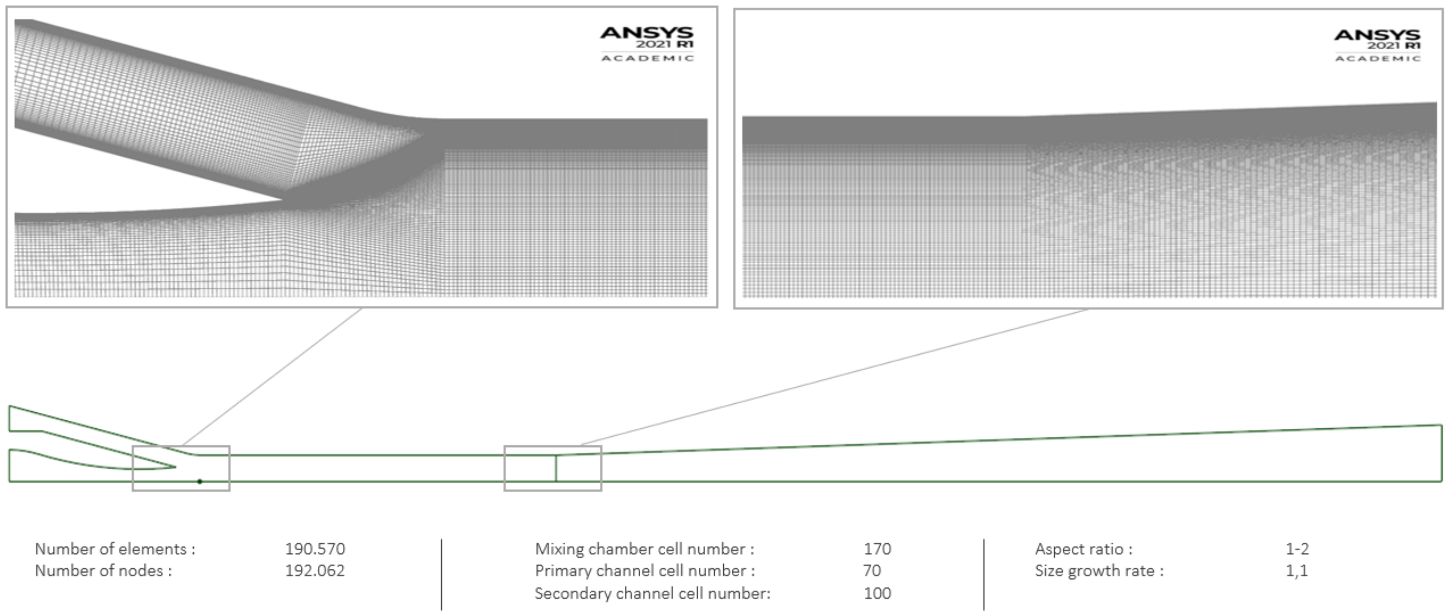

Figure 2.5: Grid structure of the axisymmetric ejector for the stationary simulations

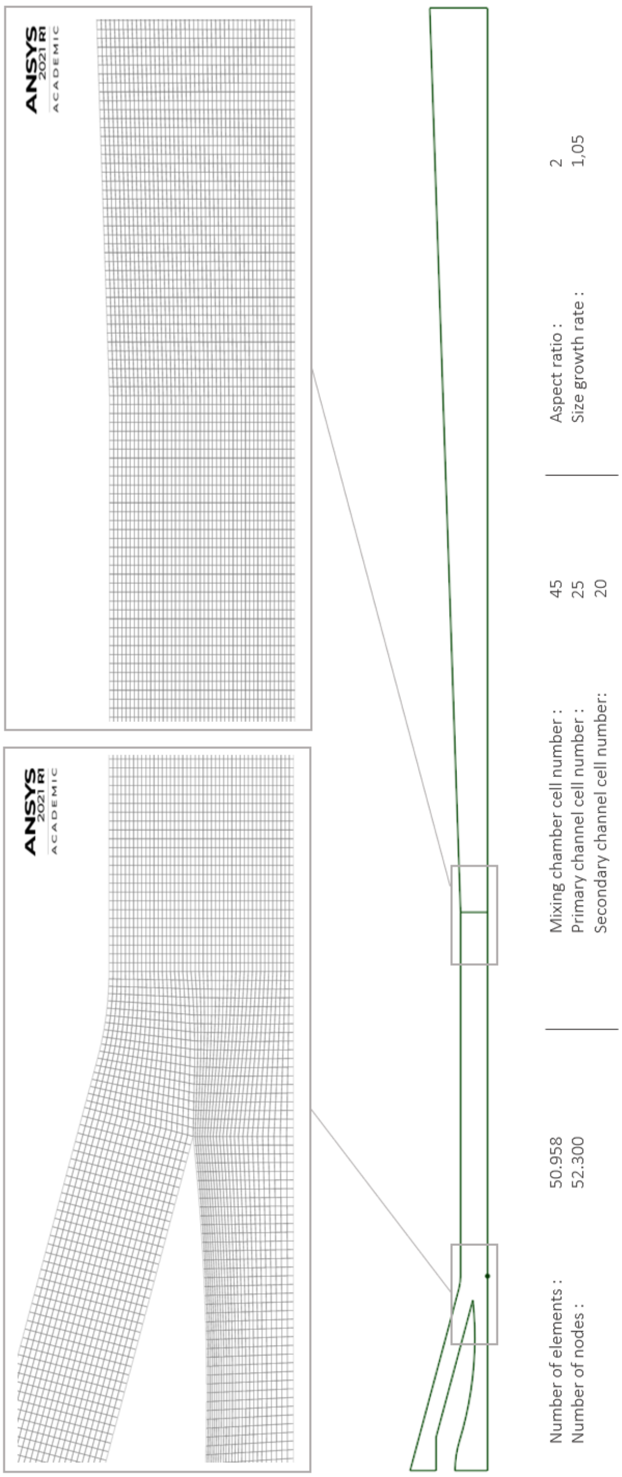

Figure 2.6: Grid structure of the axisymmetric ejector for the transient scenario simulations

	Stationary case	Transient scenario
Turbulence model	$k-\omega\ SST$	$k-\epsilon\ RNG$
Wall parameter	$y^+ < 1$	$30 < y^+ < 300$
(i) Nb. of cells in mixing chamber	170	45
(ii) AR	1-2	2
Number of elements	190,570	50,958

Table 2.1: Mesh structure details

simulations are negligible. Moreover, $k-\omega\ SST$ model predicts a more detailed shock train, as mentioned above. With regard to the entrainment ratio, the relative gap between both normal and finer meshes is in the order of 0.8% for the $k-\omega\ SST$ model and of 0.6% for the $k-\epsilon\ RNG$ model. Even if the finer mesh presented more sweeping oscillation, the numerical simulations analysed in this paper have been carried out on the normal mesh, which is fully appropriate.

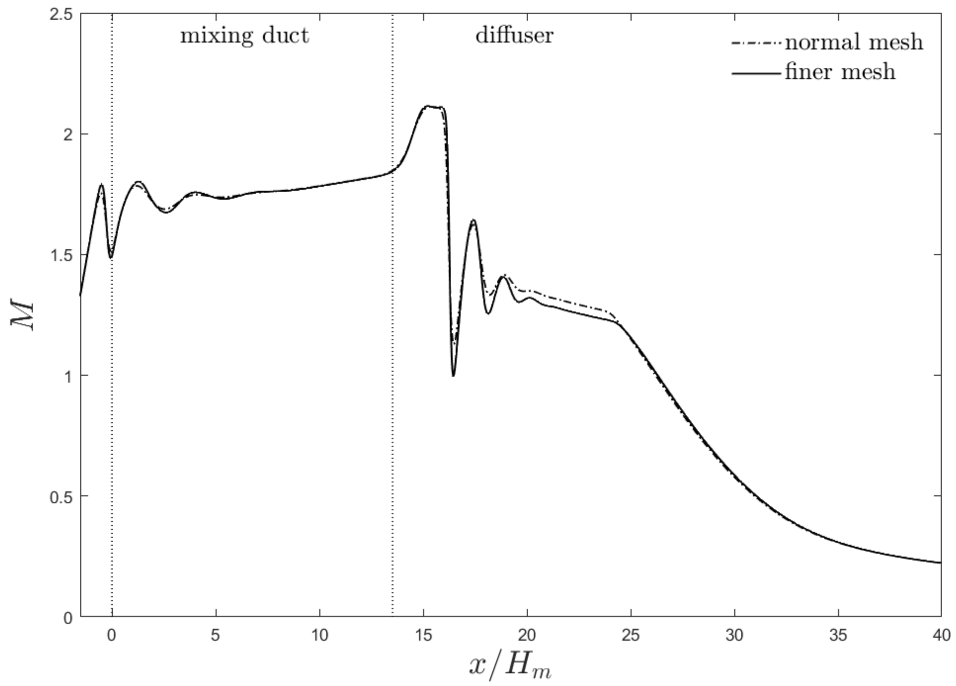

Figure 2.7: Mach number profiles along the axis of the ejector: $k-\epsilon\ RNG$ model (wall modelling) - $p_{01}/p_{02} = 3.61$ and $p_{out}/p_{02} = 1.20$.

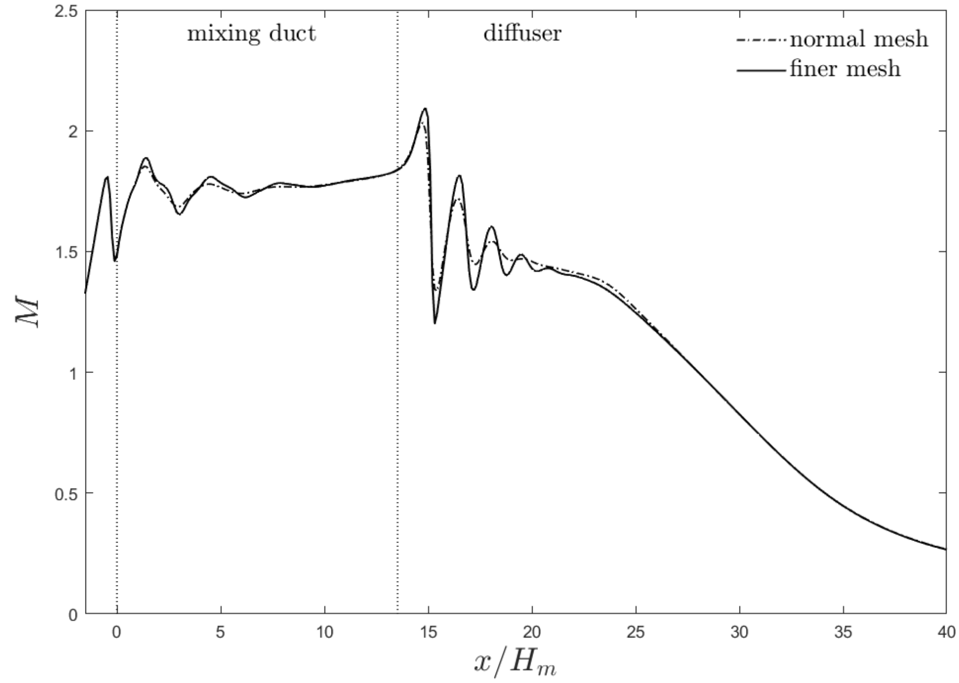

Figure 2.8: Mach number profiles along the axis of the ejector: $k-\omega$ SST model (wall-resolved) - $p_{01}/p_{02} = 3.61$ and $p_{out}/p_{02} = 1.20$.

2.3.4 Working fluid

The working fluid employed in the benchmark is air, and the ideal gas assumption has been considered. The thermophysical properties of air, provided by the Fluent database, have been used and have been considered as constant (see Table 2.2). The density has been evaluated using the ideal gas law $\bar{p} = \bar{\rho}R\hat{T}$.

Thermophysical properties of air	
Density [kg/m^3]	Ideal gas
Cp (Specific Heat) [J/(kg · K)]	1006.43
Thermal conductivity [W/(m · K)]	0.0242
Molecular viscosity [kg/(m · s)]	1.7894e-05
Molecular weight [kg/(kmol)]	28.966

Table 2.2: Air properties

2.3.5 Boundary conditions

Three boundaries conditions are imposed. The flow being subsonic at the inlet boundary, the pressure and the temperature are specified and have been assigned as the stagnation conditions : p_{01} and T_{01} for the primary flow and p_{02} and T_{02} for the secondary flow. No slip boundary conditions are imposed at the walls of the geometry. Since no heat exchange occurs with the external environment, all the walls are modelled as adiabatic. The outlet boundary condition is implemented as a pressure boundary condition, p_{out}. Regarding the turbulence boundary conditions, the turbulence intensity (5%), and hydraulic diameter d_h, have been chosen. This diameter depends on the corresponding intake pipe and is used to obtain the turbulence length scale defined by $\ell = 0.07 d_h$.

2.4 Verification and validation

To validate the present 2D simulation, the numerical results are compared to those obtained by Lamberts et al. [29]. Both rectangular simulations are performed with the same geometry, same turbulence model ($k - \omega\ SST$) but with a different solver and grid structure. As demonstrated by Hemidi et al. [20], different local flow phenomena can obtain the same entrainment ratio. Therefore, the present numerical results must be validated at global and local scale.

2.4.1 At global scale

In the first approach, the validation of a global performance parameter, such as the entrainment ratio, is performed. The comparison between the numerical characteristics curves is shown in Fig. 2.9. Due to the lack of CFD data of Lamberts et al. [29], only one value of the primary stagnation pressure is considered: $p_{01} = 3.50$ [bar] and remains constant for all the operating points. The stagnation pressure of the secondary stream is almost equal to the atmospheric pressure, since it is directly take from the atmosphere in the experiment. As mentioned by Mazzelli et al. [32] and Lamberts et al. [28], small variations of the secondary stagnation pressure were observed in the experiment when changing the back-pressure in the off-design regime. Indeed, the orifice plate used for the measurement of the secondary mass flow rate induces a pressure drop which increases with the mass flow rate and varies slightly in the off-design regime. This variation of p_{02} has been taken into account for the validation of the numerical results. The exact boundary conditions for each simulated case can be found in Table 2.3 along with the corresponding numerical results. In addition, experimental results are also presented in Fig. 2.9.

With regard to the entrainment ratio, the present numerical results are very close to the those reported in [29] all over the range of the back-pressure. The overall deviation was found to be less than 0.9%, validating the CFD accuracy of the present simulation. As highlighted by Lamberts et al. [29], the numerical simulations slightly overestimate the experimental entrainment ratio for the on-design regime : $\delta_{\text{on-design}} = 6.5\%$ and for the off-design regime : $\delta_{\text{off-design}} = 27.3\%$. As shown by Mazzelli et al. [32] and Lamberts et al. [29], these discrepancies are mainly due to 3D effects.

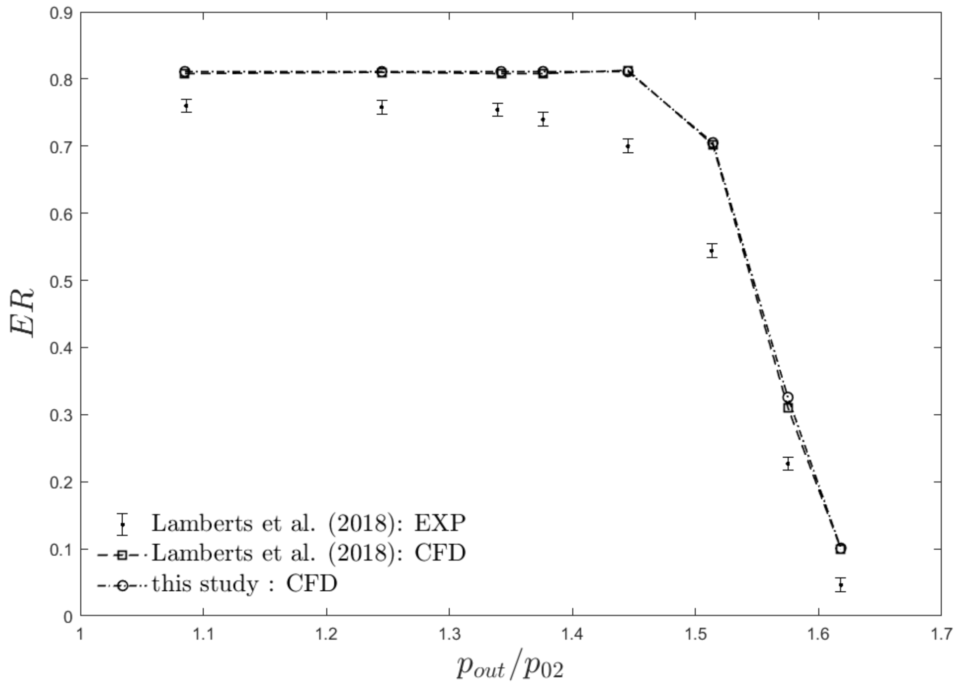

Figure 2.9: Comparison of numerical and experimental characteristic curves for $p_{01} = 3.50$ [bar]

2.4.2 At local scale

As mentioned at the beginning of this section, a second approach is used to confirm the present numerical results. The 2D rectangular simulation must be validated at local scale. Hence, the static pressure profile at the wall is investigated as there is the only numerical data available. The comparison between the present numerical results and the data of Lamberts et al. [29] is shown in Fig. 2.10, for the corresponding pressure ratio : $p_{01}/p_{02} = 3.63$, $p_{out}/p_{02} = 1.24$. The two pressure

Pressure condition [bar]			Mass flow rates [kg/s]		
p_{01}	p_{02}	p_{out}	m_1	m_2	ER
3.50	0.969	1.051	2.401	1.947	0.811
	0.969	1.206	2.401	1.947	0.811
	0.969	1.300	2.401	1.947	0.811
	0.969	1.333	2.401	1.947	0.811
	0.969	1.400	2.401	1.947	0.811
	0.987	1.495	2.401	1.692	0.705
	1.000	1.575	2.401	0.782	0.326
	1.050	1.626	2.401	0.242	0.101

Table 2.3: Tabulated values of exact boundary condition applied to 2D rectangular simulation and the corresponding results

profiles overlap perfectly. As a result, the present 2D simulation is validated locally and globally according to the numerical results of Lamberts et al. [29] and can be used for other simulations when the data is missing. As observed on Fig. 2.10 with the experimental data, the numerical simulation fails to predict the value of the static pressure acting on the wall of the mixing duct. Indeed, the CFD model underestimates the static pressure. This topic is investigated in more detail in the next chapter.

In conclusion, this chapter covers the parameterization of the numerical simulations, useful for those who wish to verify the results. The geometry of the axisymmetric ejector has been obtained by conserving the area ratio of the rectangular ejector. To meet the two main objectives of the thesis, two turbulence models were implemented: $k - \omega\ SST$ model for the comparison between the two geometries and $k - \epsilon\ RNG$ model for the transient scenario analysis. Finally, in order to validate the numerical simulation, a study of the mesh and the results at global and local scales shows the convergence of the solution and the equivalence with the numerical results of Lamberts et al. [27]. As a result, the methodology of this paper is validated and provides corrects results for the study.

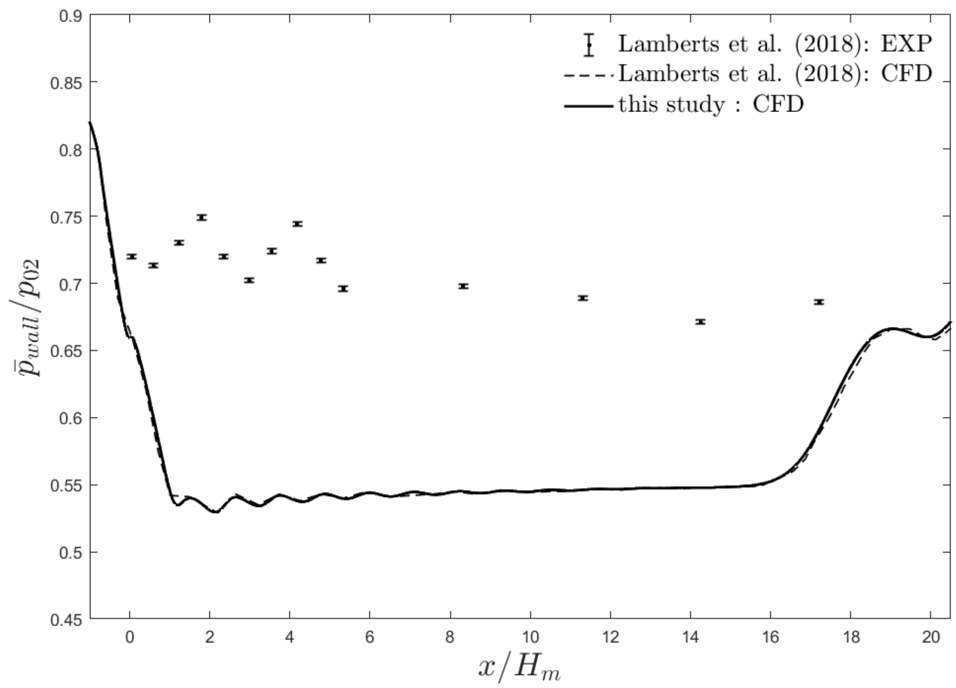

Figure 2.10: Comparison of pressure profiles from the numerical results at the wall of the secondary nozzle for $p_{01}/p_{02} = 3.63$, $p_{out}/p_{02} = 1.24$

Chapter 3

Comparison between the rectangular and axisymmetric ejector

3.1 Introduction

This chapter is dedicated to the comparison of the rectangular ejector of Lamberts et al. [27] with the adapted axisymmetric ejector, introduced in the methodology. In a first step, a comparison at the global and local scales is carried out and evinces a discrepancy between the numerical results. The exergy analysis is performed to explain these differences. Two complementary approaches were proposed: the transfer of exergy and the global exergy balance. Following this analysis, an upgraded ejector is presented in order to improve the mixing phenomena and the performance of the ejector.
In a second step, Lamberts et al. [27] shows in their paper the ability of the *compound-choking* theory to predict the on-design entrainment ratio and its limitations. However, the impact of the geometry, as well as the impact of primary temperature, has not been investigated and this chapter aims to fill this knowledge gap. As the area ratios are conserved between the two geometries, the 1D model establishes an equivalence of the results between the geometry, which will be verified in this chapter.

3.2 Characteristic curve

As a first step, the axisymmetric ejector is compared to the rectangular ejector at global scale. Characteristic curves are simulated numerically and are presented in Fig. 3.1. The variation of p_{02} with the back-pressure has been taken into account in order to compare the numerical results with the experimental data of Lamberts et al. [29] (experimental setup presented in Fig. 2.2, p. 17). Hence, the applied boundary conditions correspond to those reported in the validation (Table 2.3, p. 29).

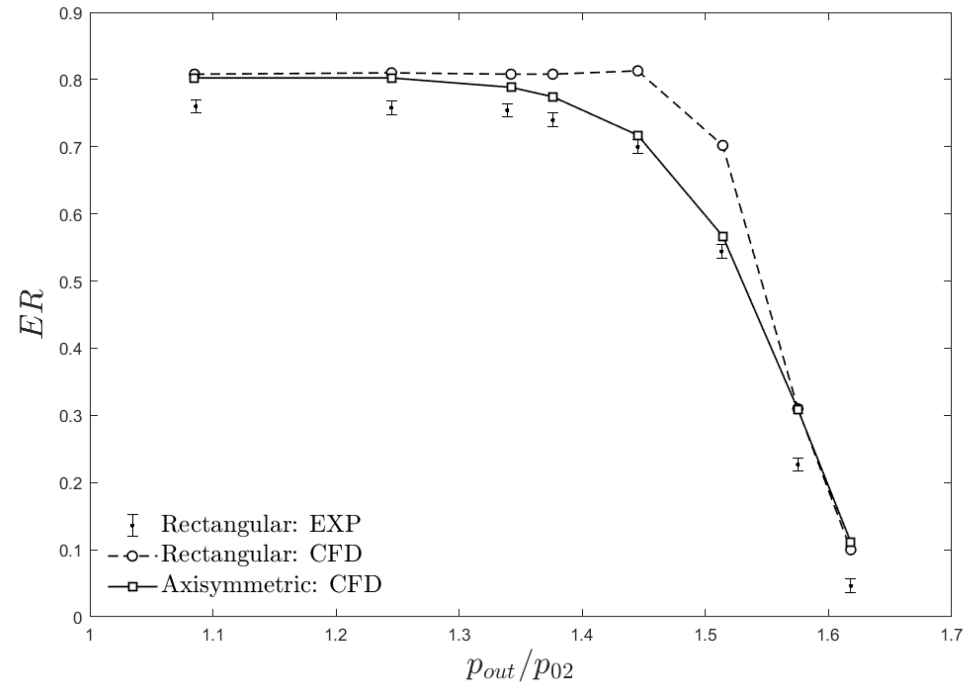

Figure 3.1: Comparison of numerical and experimental characteristic curves obtained on a rectangular and axisymmetric ejector for $p_{01} = 3.50$ [bar].

The numerical results evince a discrepancy between the two characteristic curves. The axisymmetric case shows a smoother transition between the two operating modes than the rectangular case, like the experiments. As a result, the critical back pressure is lower in the axisymmetric case. Regarding the deviation, the experimental entrainment ratio fits better with the axisymmetric case: $\delta_{\text{on-design}} = 5.7\%$ and $\delta_{\text{off-design}} = 14.3\%$, than the rectangular case: $\delta_{\text{on-design}} = 6.5\%$ and $\delta_{\text{off-design}} = 27.3\%$. Hence, the axisymmetric numerical simulation could be an alternative way to obtain the experimental results. As many authors have pointed out in their research [37, 39, 16], the axisymmetric model is quite capable of producing similar results to the three-dimensional model. However, this unfounded assumption here is not necessarily valid over a wider range of operating conditions and ejectors. Additional experimental and numerical data are required. To explain the difference in the curves, an exergy analysis is performed after the local comparison.

3.3 Static pressure profile

A second approach is used to compare the axisymmetric and the rectangular model. Due to the available experimental measurements, the profile of the static pressure at the wall is presented in Fig. 3.2. The case under consideration corresponds to the on-design conditions: $p_{01}/p_{02} = 3.63$ and $p_{out}/p_{02} = 1.24$.

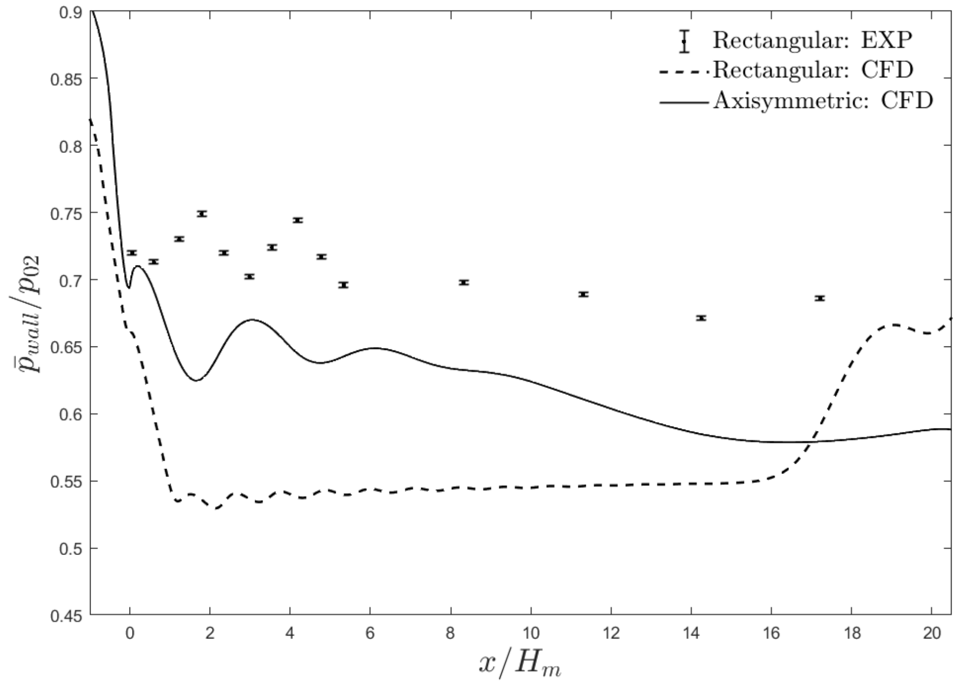

Figure 3.2: Comparison of the pressure profiles extracted from the numerical results at the wall of the secondary nozzle with the experimental measurements : $p_{01}/p_{02} = 3.63$ - $p_{out}/p_{02} = 1.24$.

As mentioned in the previous chapter, the 2D numerical simulation fails to predict the value of the static pressure acting on the wall of the mixing duct. Indeed, in the rectangular case, the CFD model underestimates the static pressure. These discrepancies are mainly due to 3D effects. In the axisymmetric case, oscillations are visible at the entry of the mixing duct, as the experiment data of the rectangular ejector. Indeed, the wall is closer to the shocks trains and the pressure is further influenced. Unfortunately, the comparison between these 2 curves is less relevant, as the geometry differs strongly between the 2 cases. Experimental data for axisymmetric geometry would be of interest and are missing from the study.

3.4 Numerical results exploited in the manuscript

As mentioned in the methodology, the variation of p_{02} has been taken into account in the experiments and the numerical simulations. However, in order to investigate the mixing and choking mechanisms, the reservoir conditions should be fixed and only the back-pressure should vary to study its impact. Hence, the slight changes in the stagnation pressure inlet observed in the experiment for off-design case are thus neglected. p_{02} is this equal to 0.969 [bar] and p_{01} is this equal to 3.50 [bar]. The resulting characteristic curves are shown in Fig. 3.3. In addition, a certain letter has been associated to each operating point in order to ease the reference to the different cases throughout the manuscript. The letter correspond to the state for both characteristic curves.

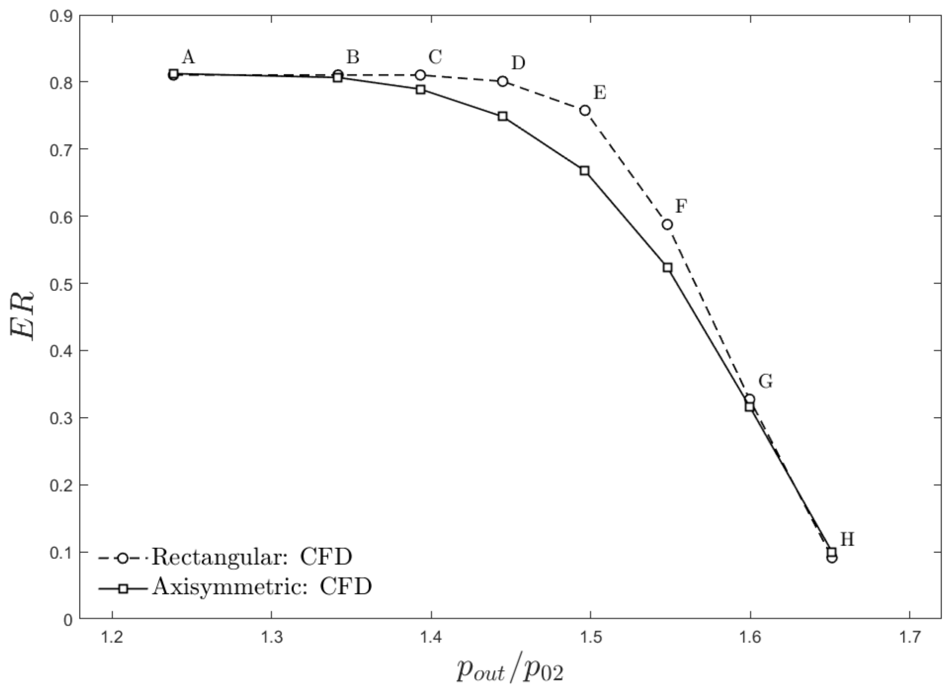

Figure 3.3: Numerical characteristic curves exploited in the manuscript

As may be seen in Fig. 3.3, the bumps (point E), that were noticeable in the numerical characteristic curves in Fig. 3.1, have disappeared due to the fixed secondary inlet pressure.

3.5 Exergy analysis

The difference between the two characteristic curves, highlighted earlier, is finally explained in depth in this section. As a reminder, the main purpose of a supersonic ejector is to give to the secondary stream the capacity to produce some work. To achieve this, a primary flow is accelerated into a nozzle and transfers its high kinetic energy to entrain the secondary flow. These transfers are directly related to the operating conditions, and thus to the shape of the characteristic curves. Therefore, to study the difference between the curves, it is necessary to investigate the difference between the transfers.

Lamberts et al. [27] propose an approach to provide novel insights into the quantification and the location of the transfers and the irreversibilities within supersonic ejectors. They performed an analysis based on classical stream tubes in order to quantify the exergy transfer between the two flows along the ejector, as well the losses. The authors introduce new quantitative indicators to assess these transfers and losses. The considered geometry was a rectangular supersonic ejector. The objective of this section is to apply this approach to an axisymmetric ejector and to compare the results to the rectangular ejector in order to explain the difference in the characteristic curves.

In this section, note that all the mathematical symbol have been selected to comply to the convention proposed by Lamberts et al. [28]. Before presenting further results, let's review the concept of exergy, tubes of transport and the computational methods.

3.5.1 The concept of exergy

As a reminder, the exergy (ξ_t) is defined as the maximum theoretical work that can be obtained from an amount of energy, expressed as follows

$$\xi_t = (h_t - h_{ref}) - T_{ref}(s - s_{ref}) \tag{3.1}$$

where h_t and s are the specific total enthalpy and the specific entropy, respectively. The subscript ref refers to the reservoir conditions of the secondary stream as the reference state, namely : $T_{ref} = T_{02}$ and $p_{ref} = p_{02}$. By doing this, the exergy of the secondary stream at reservoir condition, noted ξ_{02}, is equal to zero.

3.5.2 Local transfers

The approach aims to quantify the exchange between the two flows. In the papers of Lamberts et al. [27], the authors propose dimensionless quantities to investigate the transfers between the primary and the secondary streams along the ejector. The definition of these new quantitative indicators is recalled here.

The transfers of quantities (momentum, kinetic energy and heat) essentially occur through the shear layer and are quantified through the dividing surface, interpreted as a virtual separation between the primary and the secondary streams, as illustrated in Fig. 3.4. The local flux of a quantity Q that crosses this dividing surface is given by its total flux $\overline{F}$ and the normal vector n_j to the surface S and pointing towards the secondary stream (see Fig. 3.4) : $\overline{F}_{Q,j} \cdot n_j$. This value is positive if the quantity is transported from the primary towards the secondary flow.
The expressions of the total flux of momentum $\overline{F}_{m,j}$, of kinetic energy $\overline{F}_{K,j}$, of heat transfer $\overline{F}_{q,j}$, of exergy $\overline{F}_{\xi,j}$ are available in the research papers of Lamberts et al. [27] and are briefly explained in the appendix A. The author of this manuscript strongly advises readers to take a look at the appendix to get a clear idea of the mathematical expressions.

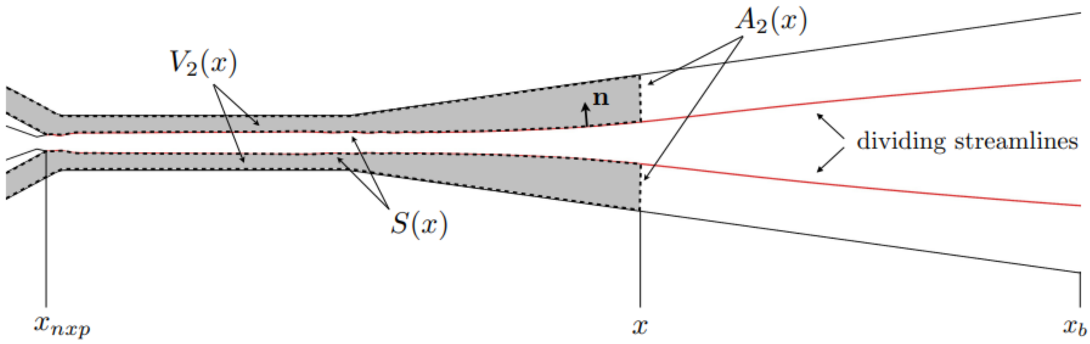

Figure 3.4: Control volume analysis [27].

The dimensionless local fluxes of the different quantities across the dividing surface are defined as

$$\overline{f}_m = \frac{A_m}{\dot{m}_1\sqrt{2\xi_{01}}}\overline{F}_{m,j} \cdot n_j \tag{3.2}$$

$$\overline{f}_K = \frac{A_m}{\dot{m}_1\xi_{01}}\overline{F}_{K,j} \cdot n_j \tag{3.3}$$

$$\overline{f}_q = \frac{A_m}{\dot{m}_1\xi_{01}}\overline{F}_{q,j} \cdot n_j \tag{3.4}$$

$$\overline{f}_\xi = \frac{A_m}{\dot{m}_1\xi_{01}}\overline{F}_{\xi,j} \cdot n_j \tag{3.5}$$

where ξ_{01} is the exergy of the primary stream at reservoir condition. Dividing by ξ_{01} allows to measure the percentage of exergy available in the primary stream that is transferred to the secondary stream. Moreover, it should be noted that, based on Equation (A.8), it follows that

$$\overline{f}_\xi = \overline{f}_K + \overline{f}_q \tag{3.6}$$

The profile of the local dimensionless transfers across the dividing surface are shown in Figs. 3.5 and 3.7 for the rectangular ejector and in Figs. 3.6 and 3.8 for the adapted axisymmetric ejector. All the graphs have been simulated numerically for different operating conditions (Point A, C, D, E, G in Fig. 3.3) and have not been taken from other sources. The similarity between these results in the study and those reported in Lamberts et al. [27], validates the post-processing computation and the results of this manuscript.

In the rectangular case, as may be seen on the figures, the transfers of momentum, mean-flow kinetic energy and exergy have essentially the same pattern for a given operating point. By contrast, the profile of the flux of exergy related to the exergy content of heat is different. Indeed, due to the temperature-correction factor, the magnitude is more important at low temperature, thus at high speed. Hence, this transfer is more important at the exit of the primary nozzle. Moreover, the magnitude of $\overline{f}_q$ is relatively low compared to the flux of mean-flow kinetic energy, $\overline{f}_K$ ($\pm 10\%$). As a result, the transfer of exergy between both streams is mainly due to a transfer of kinetic energy.
For the axisymmetric case, the transfer of momentum, mean-flow kinetic energy and exergy follows the same spatial pattern as the rectangular case. A comparison between both geometries shows that the transfer of quantities seems higher in the mixing duct of the axisymmetric ejector than the rectangular ejector. In order to assess this observation, the cumulative flux is computed in the next section to identify the order of magnitude of the transfers. Regarding the local flux of exergy content of heat, the axisymmetric geometry presents more variations, looking like instability. Moreover, the amplitude is $\pm 25\%$ less important than the rectangular case. Note that the local flux of only 3 operating point is shown to avoid overloading the figure.

In addition, for the on-design regime of both ejectors (Point A, B), a peak of the local transfer of momentum and mean-flow kinetic energy is located in the diffuser. It means that the mixing between both streams is not yet completed at the exit of the mixing duct. Finally, for a value of p_{out} close to the critical back-pressure, it seems that the peak of the local transfers is the lowest and that the transfers are more uniformly distributed all along the mixing duct. The corresponding operating point is (D) for the rectangular case and is (C) for the axisymmetric case.

Rectangular ejector

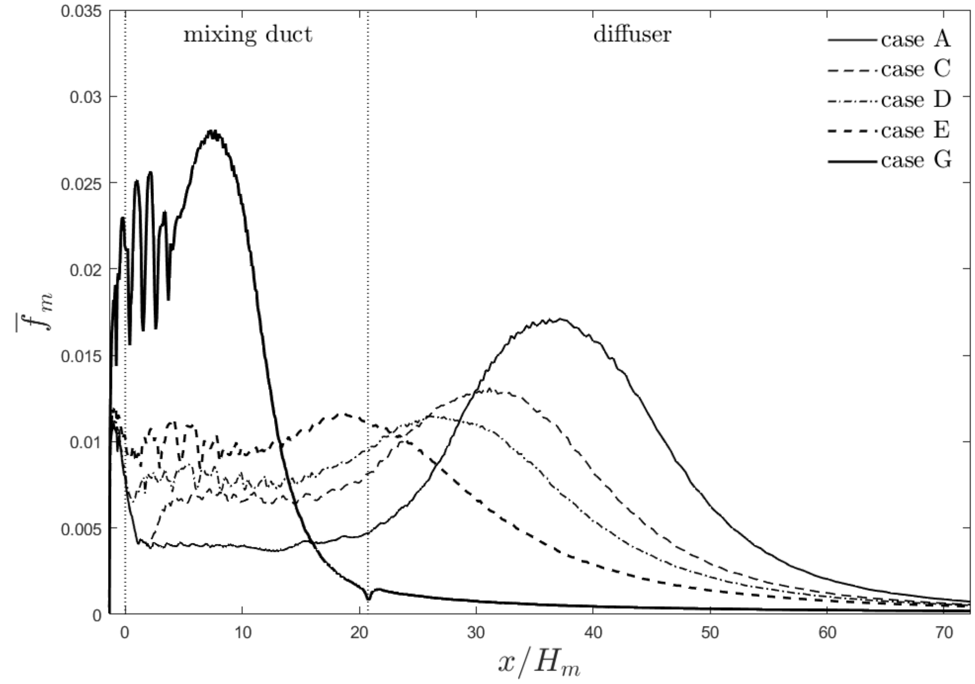

(a) momentum

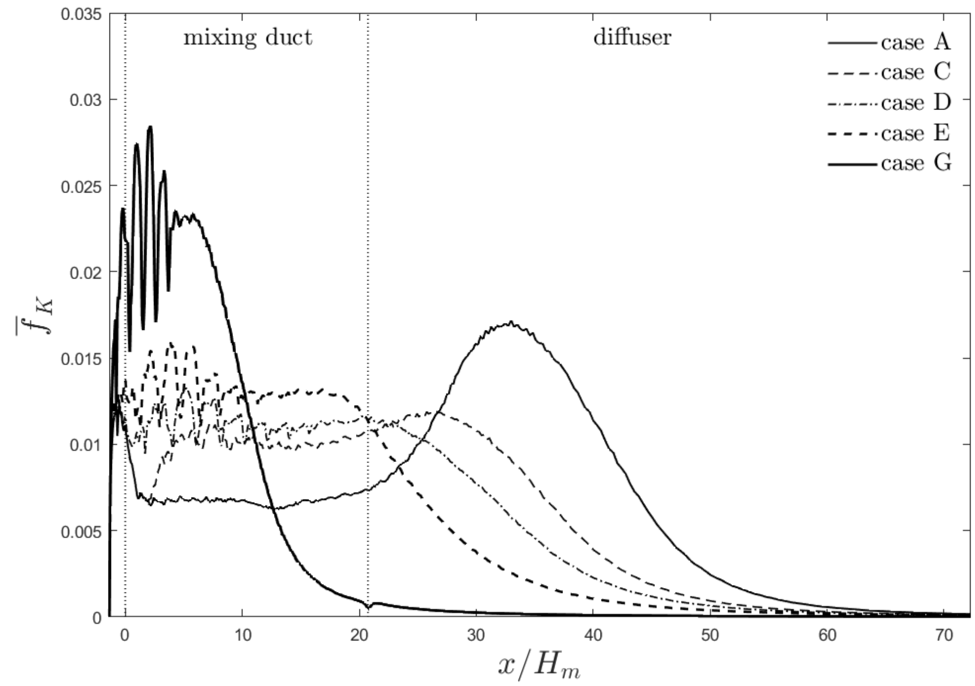

(b) mean-flow kinetic energy

Figure 3.5: Dimensionless local flux of (a) momentum and (b) mean-flow kinetic energy crossing the dividing surface for different values of the back-pressure - $p_{01}/p_{02} = 3.61$.

Axisymmetric ejector

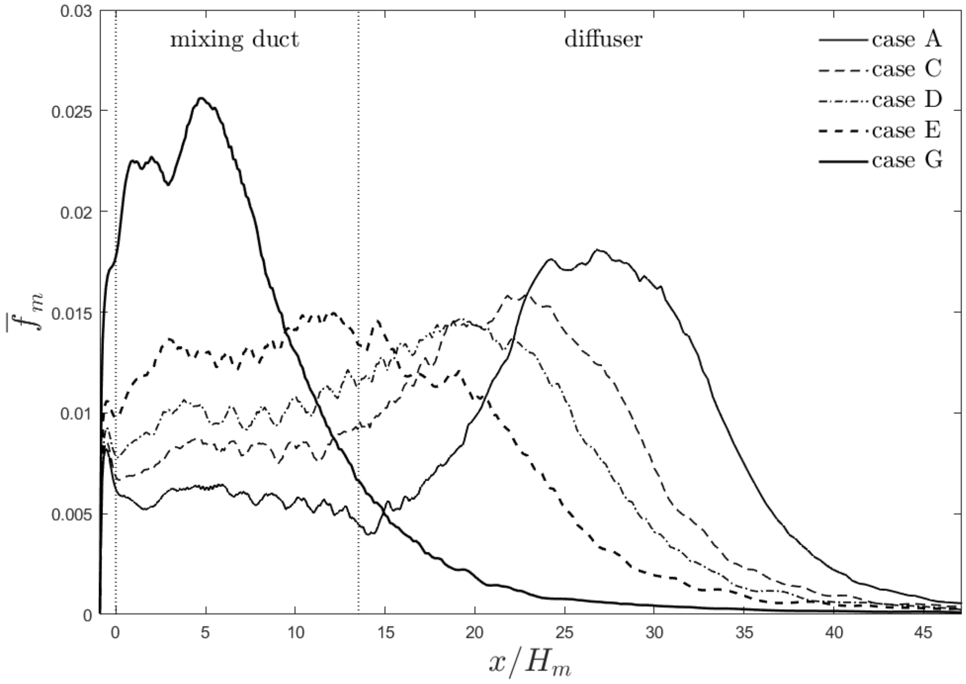

(a) momentum

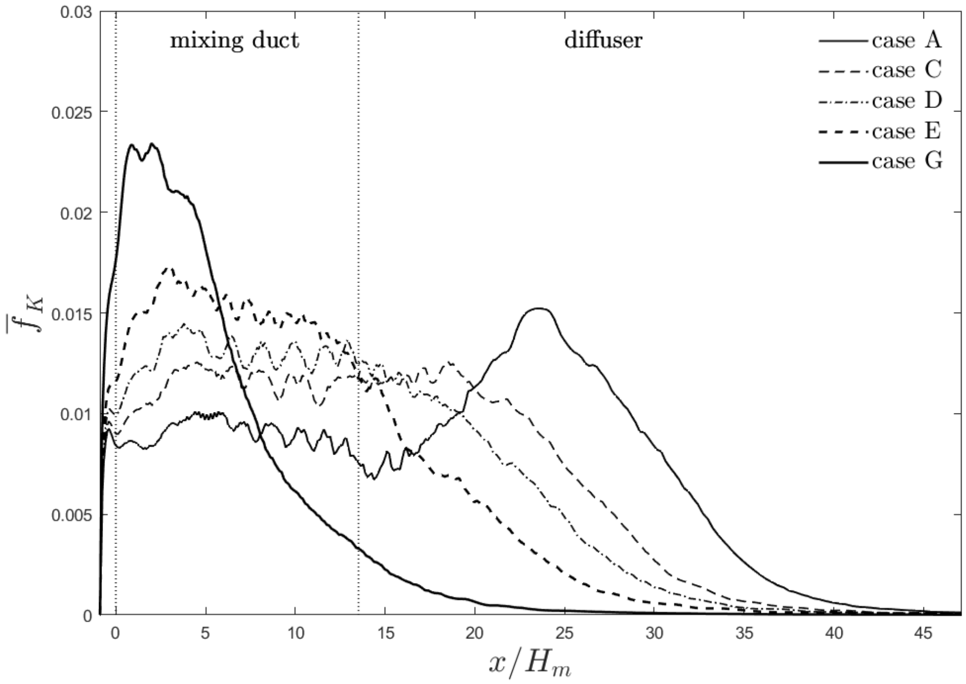

(b) mean-flow kinetic energy

Figure 3.6: Dimensionless local flux of (a) momentum and (b) mean-flow kinetic energy crossing the dividing surface for different values of the back-pressure - $p_{01}/p_{02} = 3.61$.

Rectangular ejector

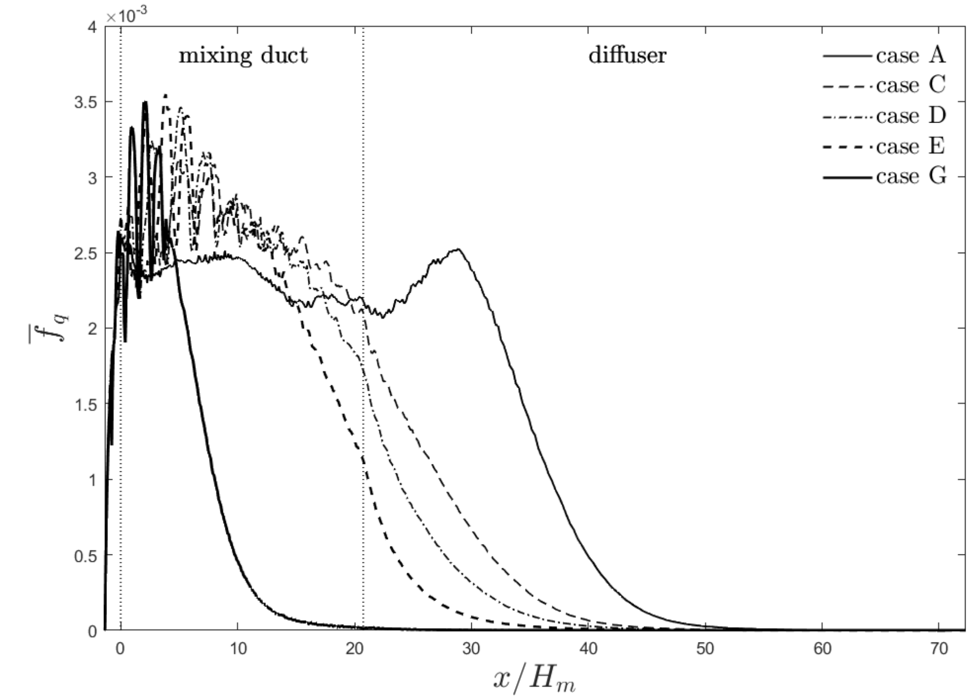

(a) exergy content of heat

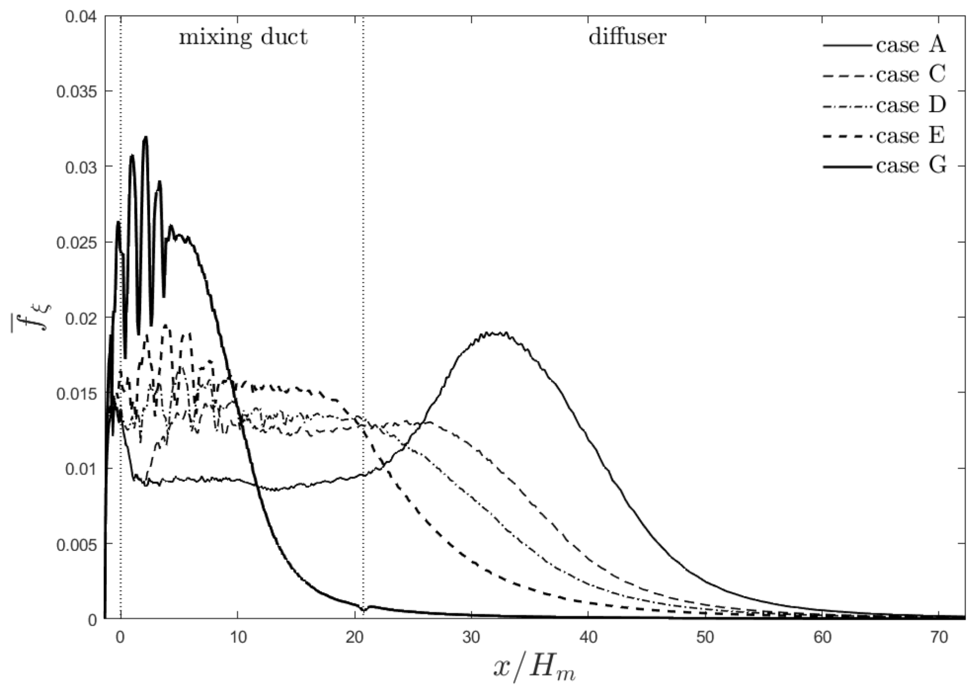

(b) mean-flow total exergy

Figure 3.7: Dimensionless local flux of (a) heat (exergy content) and (b) mean-flow total exergy crossing the dividing surface for different values of the back-pressure - $p_{01}/p_{02} = 3.61$.

Axisymmetric ejector

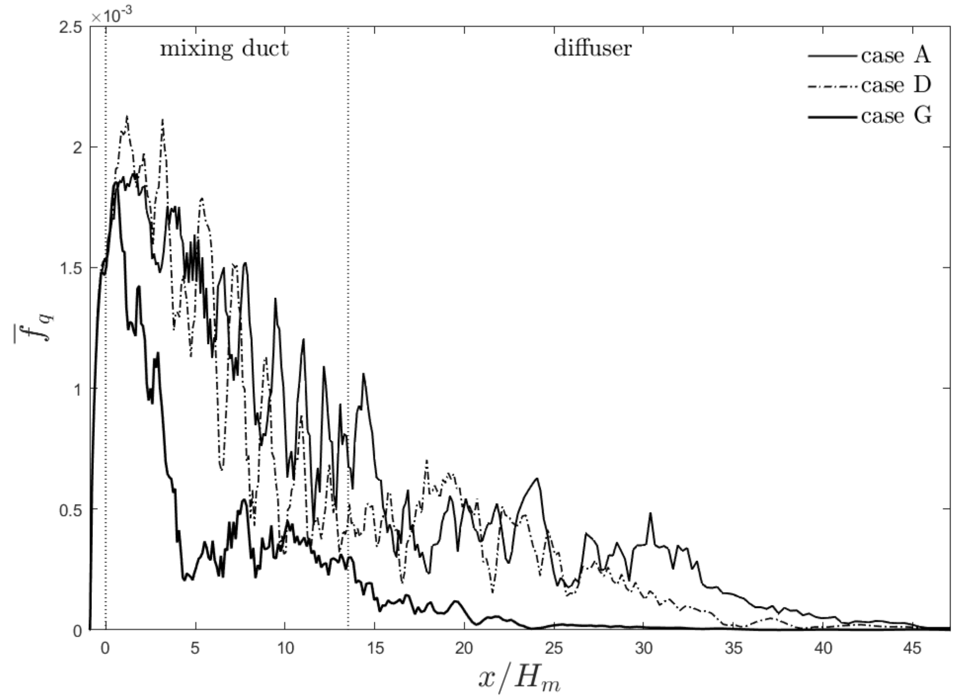

(a) exergy content of heat

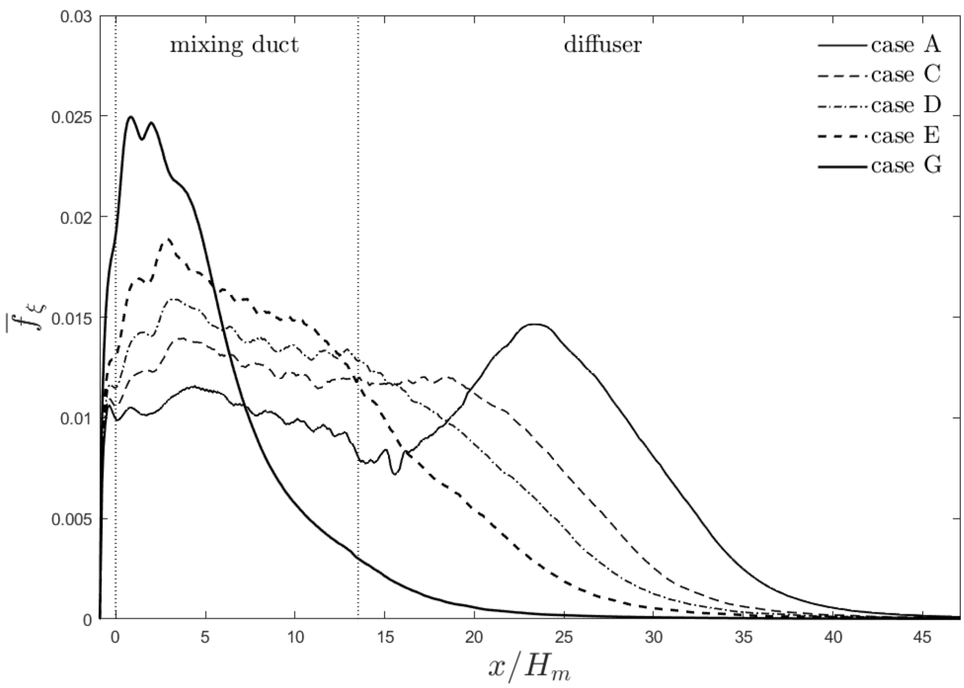

(b) mean-flow total exergy

Figure 3.8: Dimensionless local flux of (a) heat (exergy content) and (b) mean-flow total exergy crossing the dividing surface for different values of the back-pressure - $p_{01}/p_{02} = 3.61$.

3.5.3 Cumulative transfers

In order to compare the global transfer between the two geometries, the cumulative flux must be computed. A new quantitative indicator is introduced : the dimensionless cumulative transfer, $I(x)$, defined by the surface integral, of the local transfers :

$$I_m(x) = \frac{1}{A_m} \iint_{S(x)} \overline{f}_m \; ds \tag{3.7}$$

$$I_K(x) = \frac{1}{A_m} \iint_{S(x)} \overline{f}_K \; ds \tag{3.8}$$

$$I_q(x) = \frac{1}{A_m} \iint_{S(x)} \overline{f}_q \; ds \tag{3.9}$$

$$I_\xi(x) = \frac{1}{A_m} \iint_{S(x)} \overline{f}_\xi \; ds = I_K(x) + I_q(x) \tag{3.10}$$

where $S(x)$ represents the surface of the dividing surface between the nozzle exit position x_{xnp}, and the position x, taking into account the upper and lower halves of the ejector (see Fig. 3.4). In the rectangular case, this surface consists of two planes, whereas in the axisymmetric case, the surface is a cylinder. Under the axisymmetric/planar assumption, the surface integral for a quantity Q, may be rewritten as follows

$$I_Q(x) = \frac{1}{H_m} \int_{\Gamma(x)} (\overline{f}_Q) \cdot d\gamma \qquad \text{(rect.)} \tag{3.11}$$

$$I_Q(x) = \frac{2\pi}{A_m} \int_{\Gamma(x)} (r\overline{f}_Q) \cdot d\gamma \qquad \text{(axis.)} \tag{3.12}$$

with $\Gamma(x)$, the curve of the dividing streamline. Due to the limited option of the CFD-Post of Fluent, these surface integrals have been computed by MATLAB.

The profiles of $I_m(x)$, $I_K(x)$, $I_I(x)$ and $I_\xi(x)$ are shown in Figs. 3.9 and 3.11 for the rectangular ejector and Figs. 3.10 and 3.12 for the axisymmetric ejector. Since the $\overline{f}_m$, $\overline{f}_K$ and $\overline{f}_\xi$ have the same spatial pattern, I_m, I_K and I_ξ have also the same pattern for both geometries. Furthermore, in the rectangular case, the value of $I_m(x_b)$ is very close to the value of $I_K(x_b)$ for the same operating point. Whereas in the axisymmetric case, there is a difference of 20% between the $I_m(x_b)$ and $I_K(x_b)$. Concerning the exergy content of heat, I_q, the order of magnitude is twice as small in the axisymmetric ejector and slowly stabilizes due to the unsteady variations (see Fig. 3.8a). These differences of I_K and I_q between both geometries implies a difference of the global transfers I_ξ. This value corresponds to the percentage of exergy available in the primary flow transferred to the secondary flow. Finally, this analysis of the cumulative fluxes concludes that the transfers is superior in the rectangular ejector, which contradicts our previous observation.

Rectangular ejector

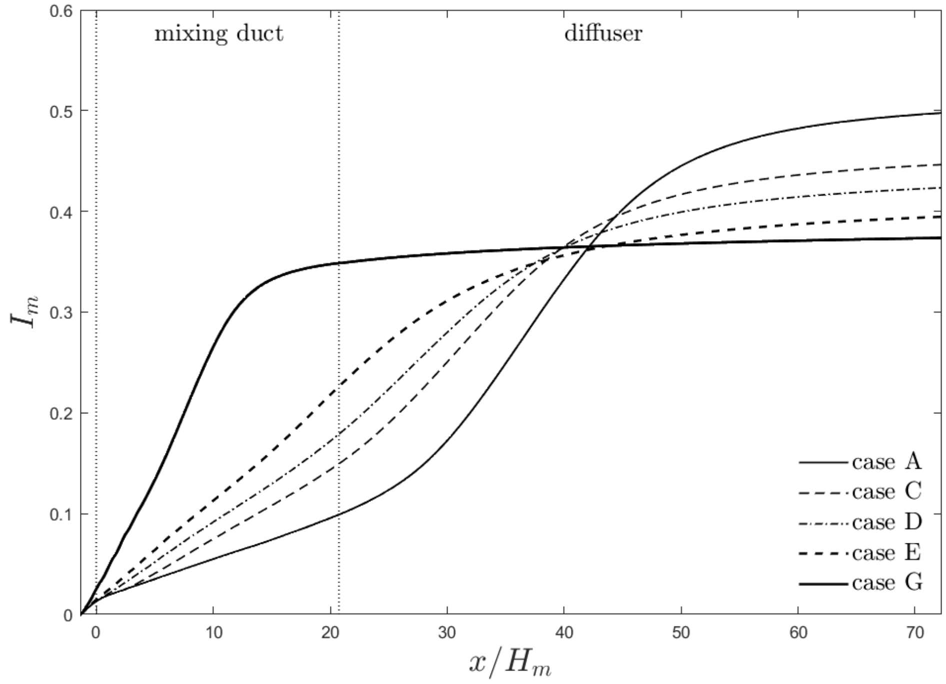

(a) momentum

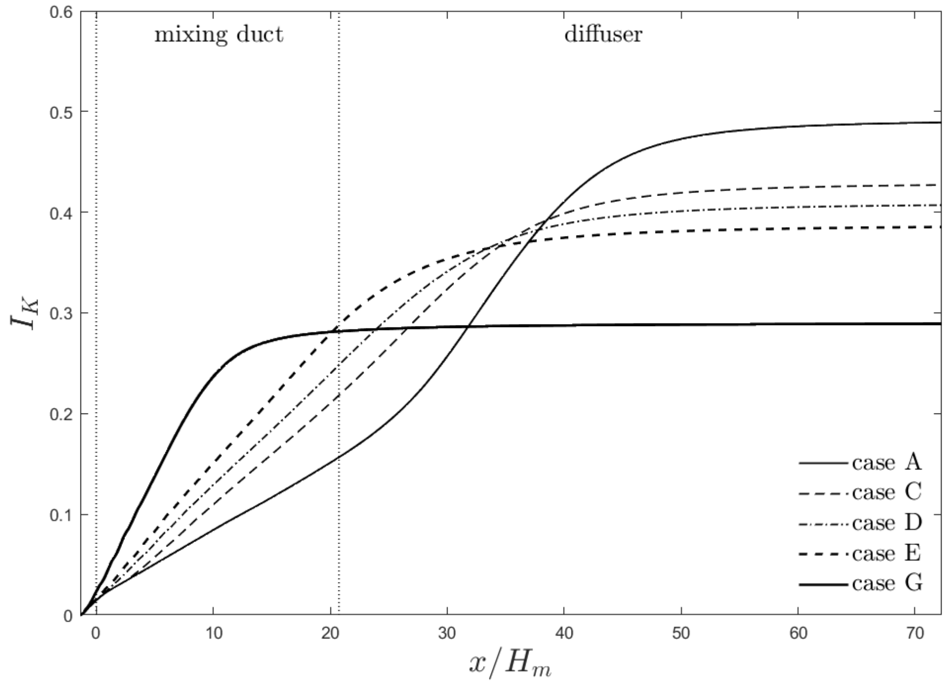

(b) mean-flow kinetic energy

Figure 3.9: Dimensionless cumulative flux of (a) momentum and (b) mean-flow kinetic energy crossing the dividing surface for different values of the back-pressure - $p_{01}/p_{02} = 3.61$.

Axisymmetric ejector

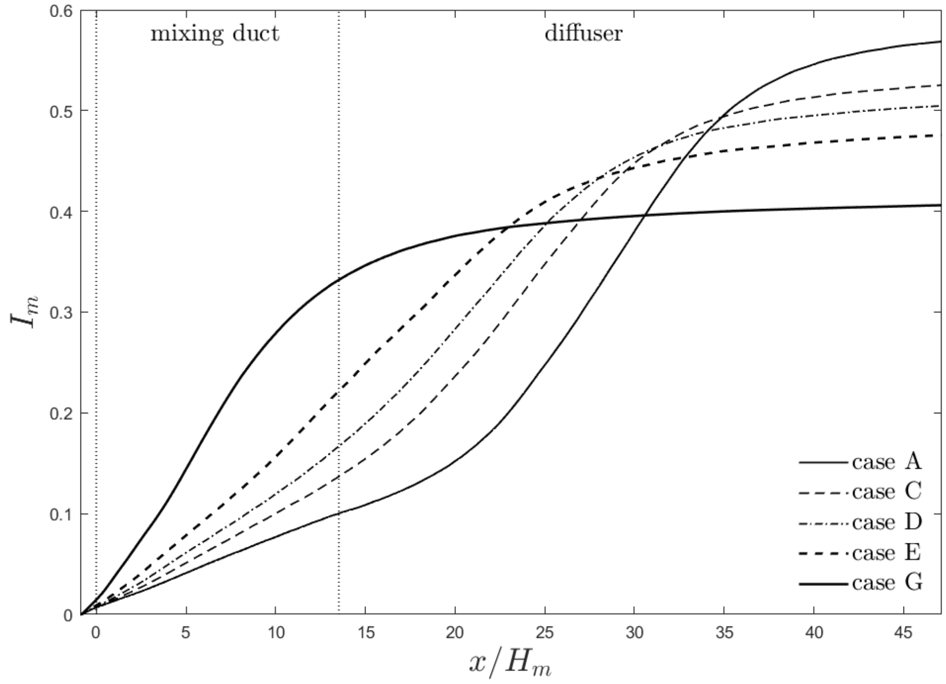

(a) momentum

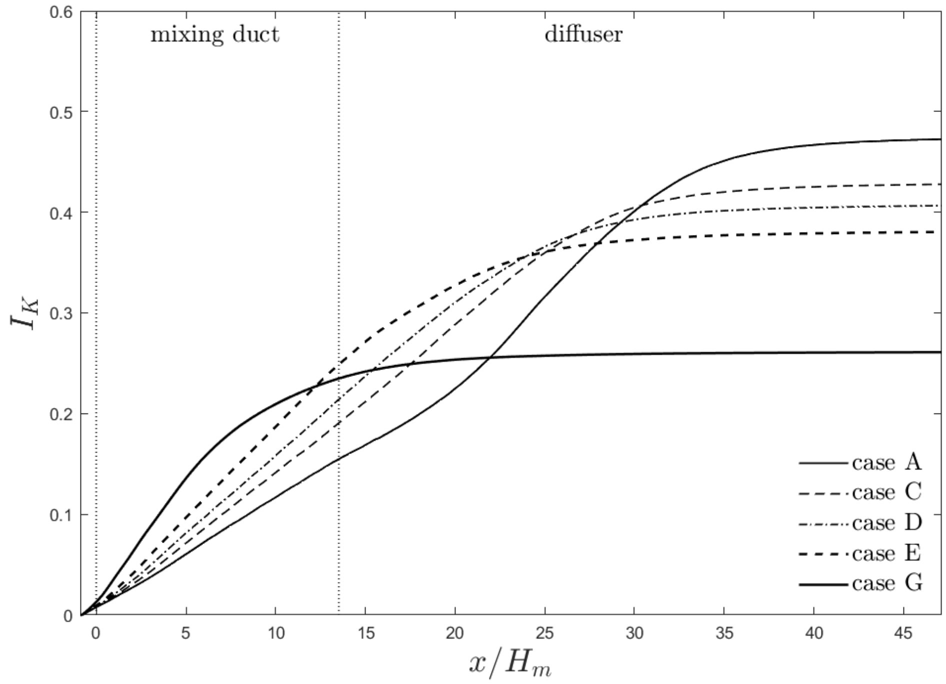

(b) mean-flow kinetic energy

Figure 3.10: Dimensionless cumulative flux of (a) momentum and (b) mean-flow kinetic energy crossing the dividing surface for different values of the back-pressure - $p_{01}/p_{02} = 3.61$.

Rectangular ejector

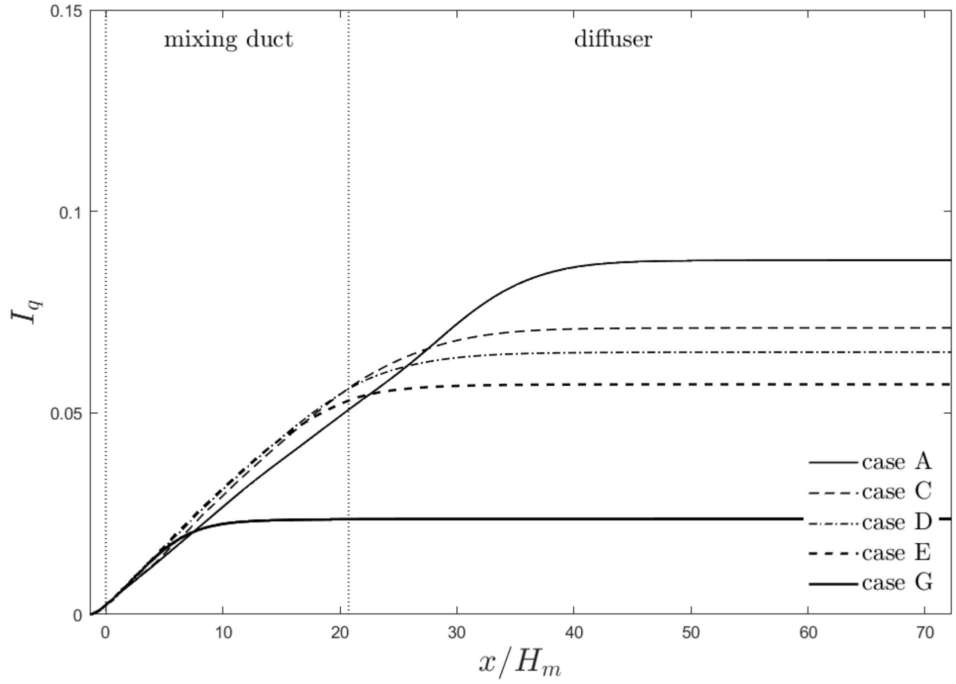

(a) exergy content of heat

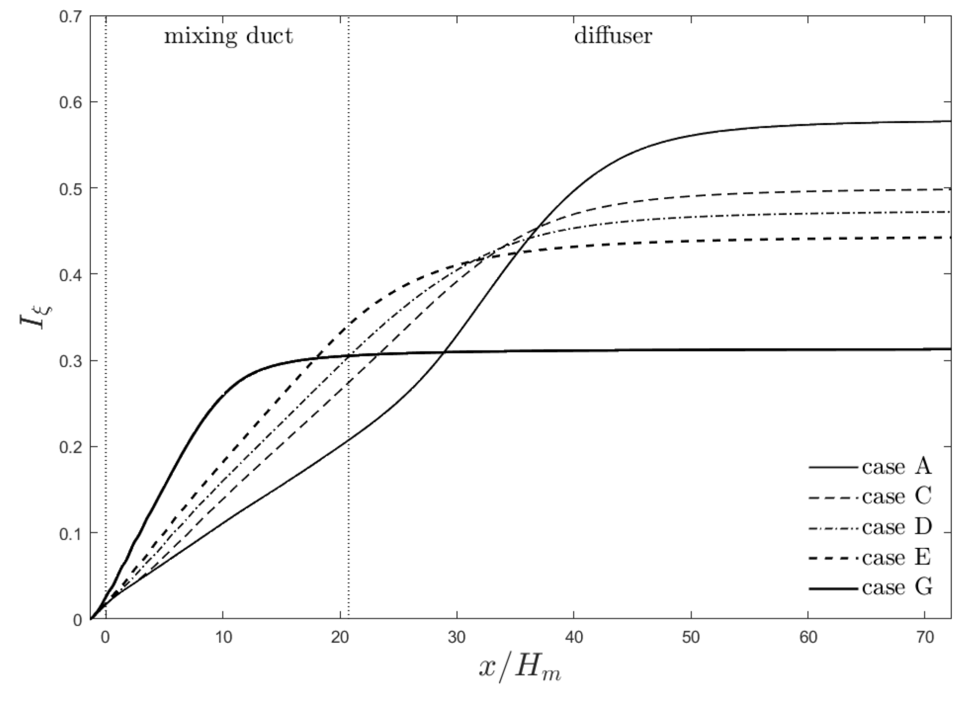

(b) mean-flow total exergy

Figure 3.11: Dimensionless cumulative flux of (a) heat (exergy content) and (b) mean-flow total exergy crossing the dividing surface for different values of the back-pressure - $p_{01}/p_{02} = 3.61$.

Axisymmetric ejector

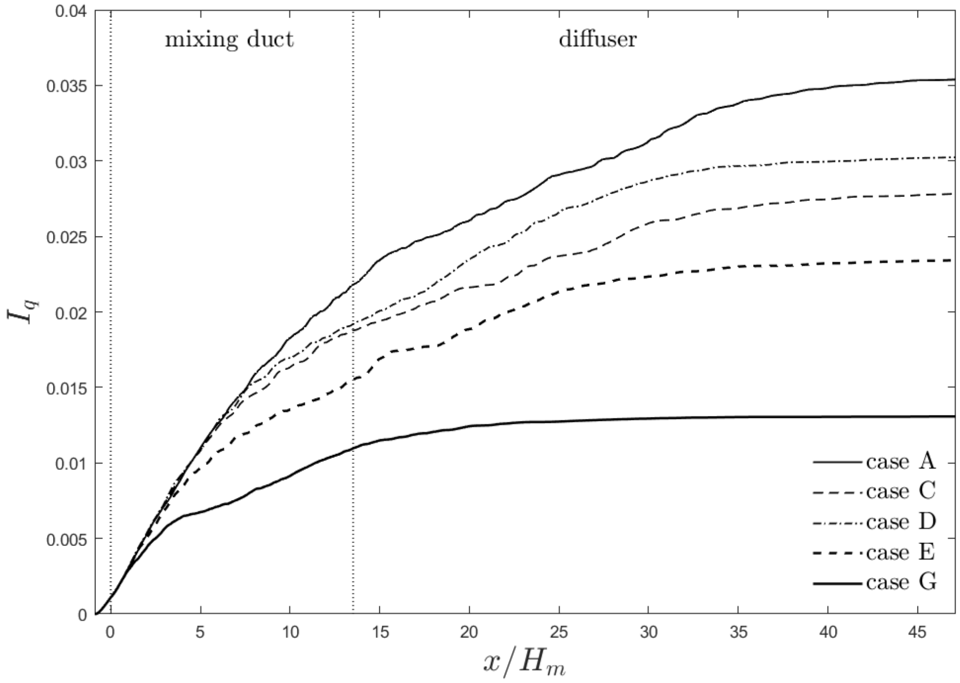

(a) exergy content of heat

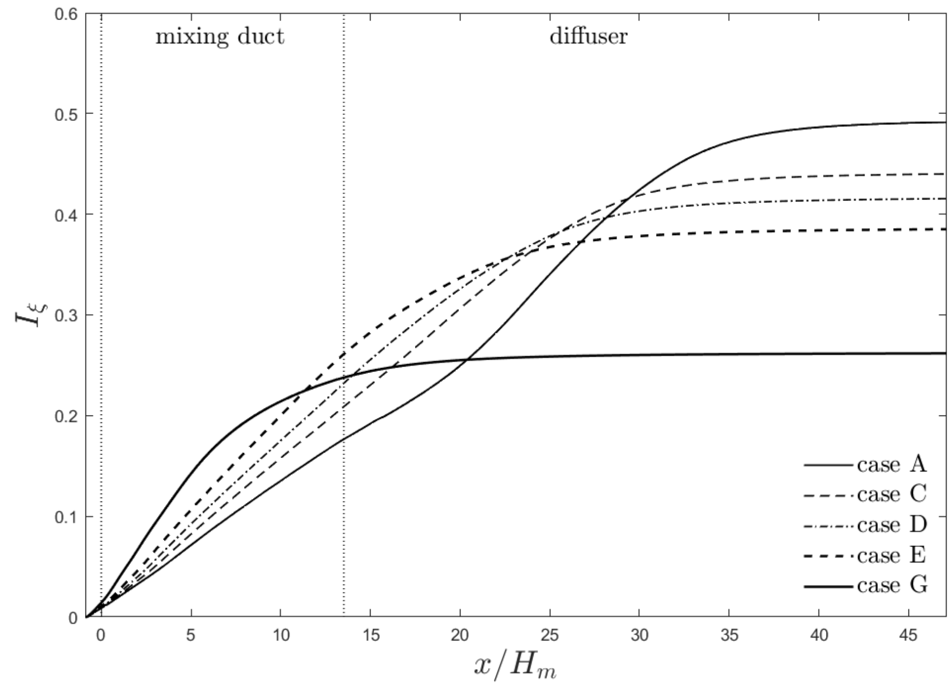

(b) mean-flow total exergy

Figure 3.12: Dimensionless cumulative flux of (a) heat (exergy content) and (b) mean-flow total exergy crossing the dividing surface for different values of the back-pressure - $p_{01}/p_{02} = 3.61$.

3.5.4 Exergy losses

The analysis of the previous section concludes that the cumulative flux of mean-flow total exergy is higher in the rectangular ejector than in the axisymmetric ejector. Furthermore, a higher value of the global transfer does not imply a maximum gain in exergy, due to the losses occurring in the secondary stream. Indeed, the net exergy gain in the secondary flow takes into account the exergy transfer from the primary flow and the exergy dissipation. This section is therefore devoted to the quantification and comparison of losses between the two geometries.

As mentioned in the appendix A, the mean-flow total exergy is dissipated in two different ways : the viscous dissipation ($T_{\text{ref}}\Phi/\hat{T}$) and the heat transfer dissipation ($T_{\text{ref}}\Phi_\Theta/\hat{T}^2$). In addition, shock waves inside the ejector lead to further exergy losses due to entropy increase ($T_{\text{ref}}\Delta s$). Nevertheless, Lamberts et al. [27] showed that these are negligible. Indeed, the authors found that these exergy losses represent less than 0.05% of the exergy at primary reservoir condition, ξ_{01}. Hence, only the two first losses are considered in this manuscript.

In order to quantify the local distribution of these terms, other quantitative indicators emerge: the local dimensionless losses in the secondary flow, computed by the surface integrals over the secondary stream cross-section, $A_2(x)$ (see Fig. 3.4, p. 36) :

$$\pi_2(x) = \frac{H_m T_{\text{ref}}}{\dot{m}_1 \xi_{01}} \iint_{A_2(x)} \frac{\Phi}{\hat{T}}\, ds \tag{3.13}$$

$$\pi_{\Theta,2}(x) = \frac{H_m T_{\text{ref}}}{\dot{m}_1 \xi_{01}} \iint_{A_2(x)} \frac{\Phi_\Theta}{\hat{T}^2}\, ds \tag{3.14}$$

where $A_2(x)$ represents the cross-section bounded by the dividing surface and through which the secondary stream virtually flows. In the rectangular case, it represents a plane surface, whereas in the axisymmetric case it represents an annular surface. As a reminder, under the axisymmetric/rectangular assumption, the surface integral for a quantity Q, may be rewritten as follows

$$\iint_{A_2(x)} Q\ ds = 2 \cdot l_m \int_{y_{divid.}(x)}^{y_{wall}(x)} Q\ dy \tag{3.15}$$

$$= \int_{r_{divid.}(x)}^{r_{wall}(x)} Q\ (2\pi r)\ dr \tag{3.16}$$

where l_m is the cross-section of the rectangular ejector (50.0 [mm]). The profiles of $\pi_2(x)$ and $\pi_{\Theta,2}(x)$ are shown in Fig. 3.13 for the rectangular ejector and Fig. 3.14 for the axisymmetric ejector. A first remark to be made on these figures is that the

irreversibilities linked to viscous dissipation are more than 10 times greater than the exergy losses linked to thermal transfers. First, these local profiles are closely similar to the profiles of local transfer. Indeed, the viscous and the turbulent fluxes ($\overline{\tau}_{ij}$ and $\overline{\tau}_{ij}^{t}$, respectively) of momentum or kinetic energy are intimately connected with the dissipation of total exergy (see in the appendix A). Secondly, as reported by Lamberts et al. [27], the peak in the profile of $\pi_2(x)$ for the case A and case G is related to the flow detachment and the corresponding zone of recirculation. In the axisymmetric, these peak in the diffuser decreases due to the lower outlet diverging angle (1.95°, 4° for the axisymmetric and rectangular case, respectively). This lower value avoids the flow detachment, and therefore the exergy losses.
The main difference between the two geometries is the amplitude of $\pi_2(x)$ and $\pi_{\Theta,2}(x)$. The losses in the axisymmetric case are twice as low as in the rectangular case. As far as heat transfer is concerned, energy losses occur mainly in the mixing duct for the rectangular case, while for the axisymmetric case they occur mainly along the diffuser.

In accordance with the above expression, in order to quantify the global losses, the dimensionless cumulative mean-flow exergy destructions are also introduced and are expressed as follows :

$$\Pi_2(x) = \frac{T_{\mathrm{ref}}}{\dot{m}_1 \xi_{01}} \iiint_{V_2(x)} \frac{\Phi}{\hat{T}} \, dV \tag{3.17}$$

$$\Pi_{\Theta,2}(x) = \frac{T_{\mathrm{ref}}}{\dot{m}_1 \xi_{01}} \iiint_{V_2(x)} \frac{\Phi_\Theta}{\hat{T}^2} \, dV \tag{3.18}$$

where $V_2(x)$ is the volume occupied by the secondary stream between the secondary inlet and the position x (see Fig. 3.4, p. 36). The results of $\Pi_2(x)$ and $\Pi_{\Theta,2}(x)$ for both geometries are presented in Figs. 3.15 and 3.16.

As may be seen on these figure, the global exergy losses due to the heat flux are much lower than those due to mean-flow viscous dissipation. Moreover, in the two geometries, the $\Pi_2(x)$ decreases initially with the back pressure and increases secondly with the back pressure. The flow therefore has a minimum overall loss, which corresponds approximately to case E in the rectangular case and to case D-E in the axisymmetric case. Finally, for the exergy destruction due to heat transfer, the cumulative losses do not stabilize in the axisymmetric due to the fact that the losses occur mainly in the diffuser rather than in the mixing duct. Even if the exergy losses are lower in the axisymmetric case, it does not necessarily imply that the net exergy gain in the secondary flow is higher in the axisymmetric case. Indeed, as observed earlier, the exergy transfer is also lower. It is therefore interesting to combine all the global results to evaluate the net exergy gain in the secondary flow, which is done in the next section.

Rectangular ejector

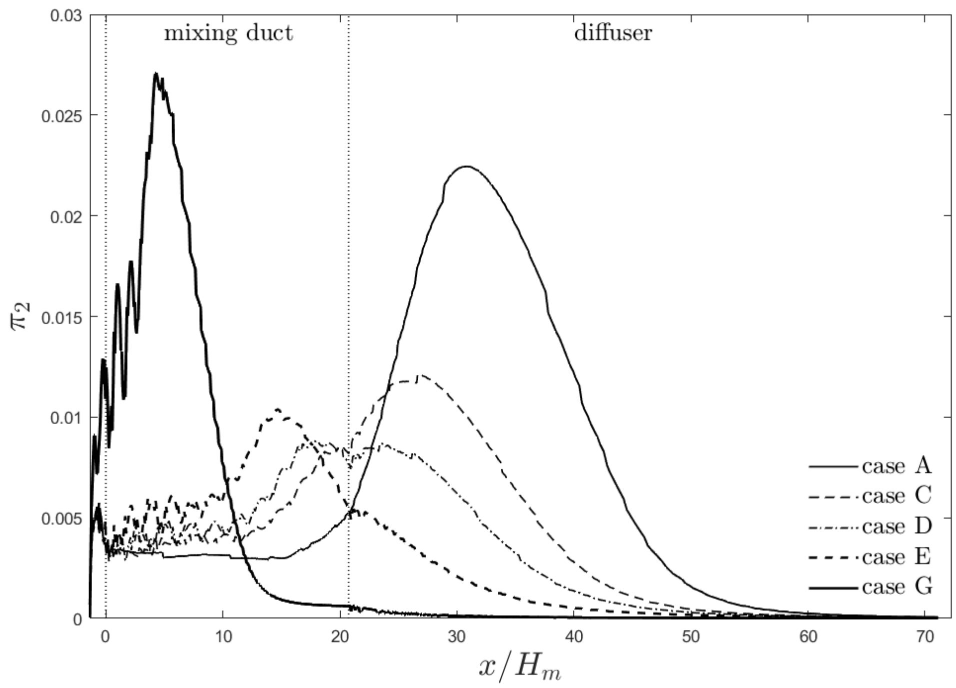

(a) viscous dissipation

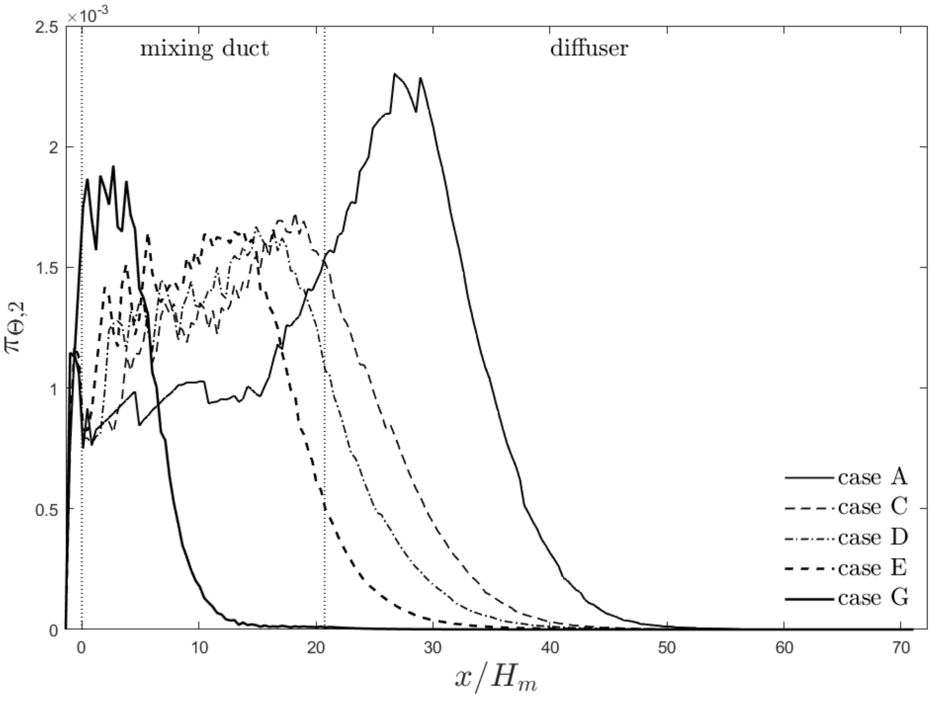

(b) heat transfer

Figure 3.13: Dimensionless local mean-flow total exergy destruction related to (a) viscous dissipation and (b) heat-transfer in the secondary stream for different values of the back-pressure - $p_{01}/p_{02} = 3.61$.

Axisymmetric ejector

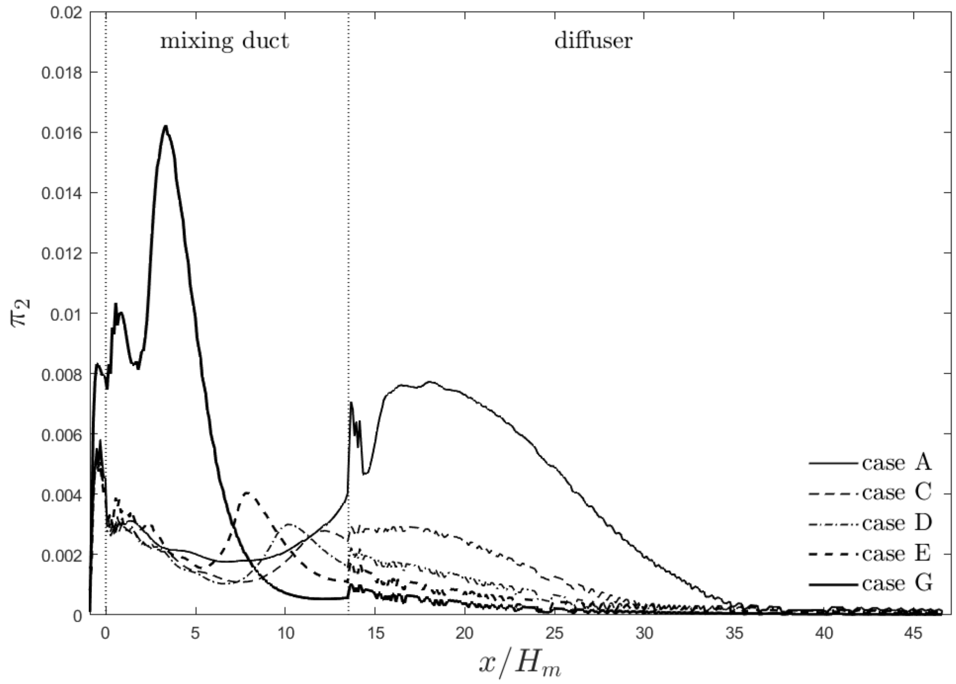

(a) viscous dissipation

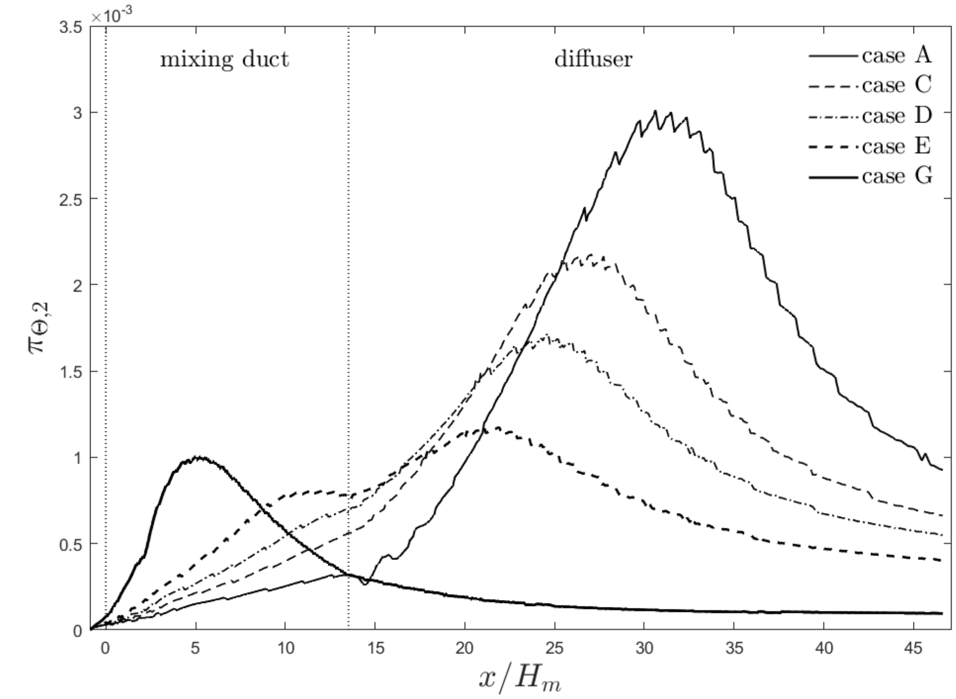

(b) heat transfer

Figure 3.14: Dimensionless local mean-flow total exergy destruction related to (a) viscous dissipation and (b) heat-transfer in the secondary stream for different values of the back-pressure - $p_{01}/p_{02} = 3.61$.

Rectangular ejector

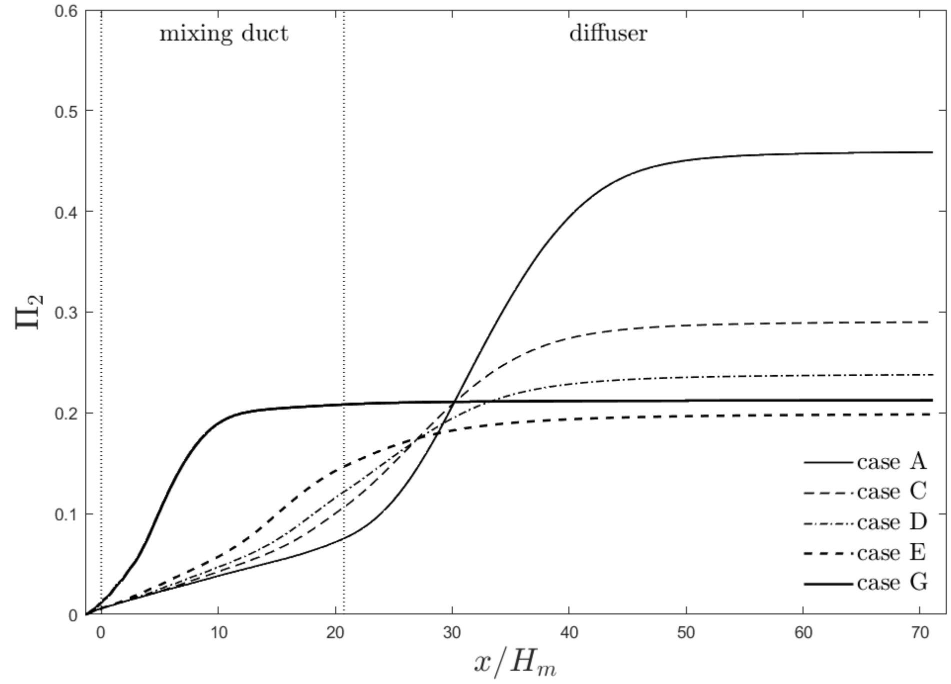

(a) viscous dissipation

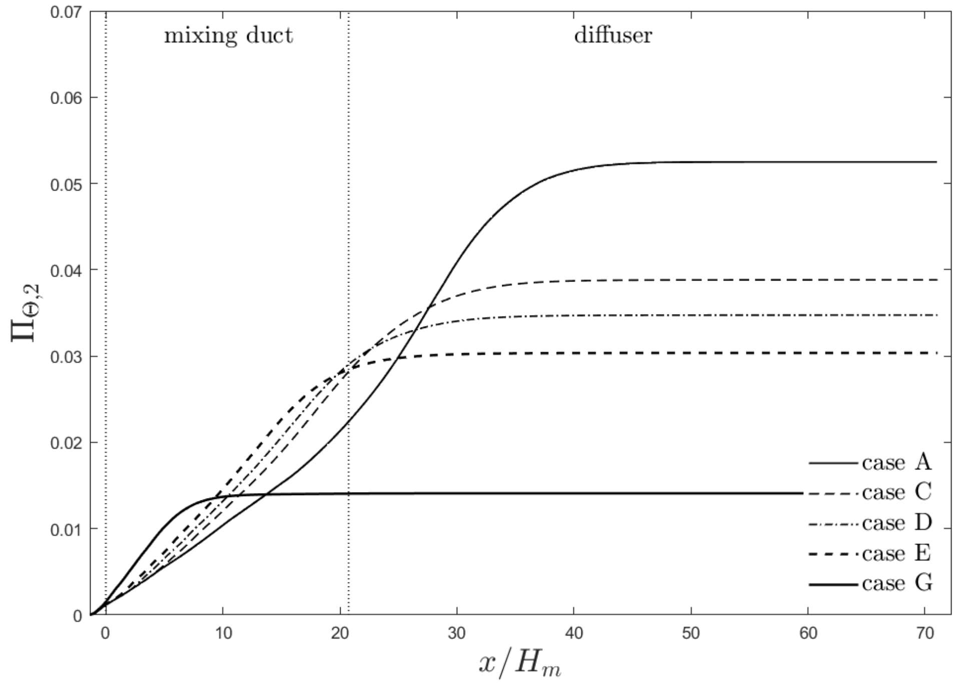

(b) heat transfer

Figure 3.15: Dimensionless cumulative mean-flow total exergy destruction related to (a) viscous dissipation and (b) heat-transfer in the secondary stream for different values of the back-pressure - $p_{01}/p_{02} = 3.61$.

Axisymmetric ejector

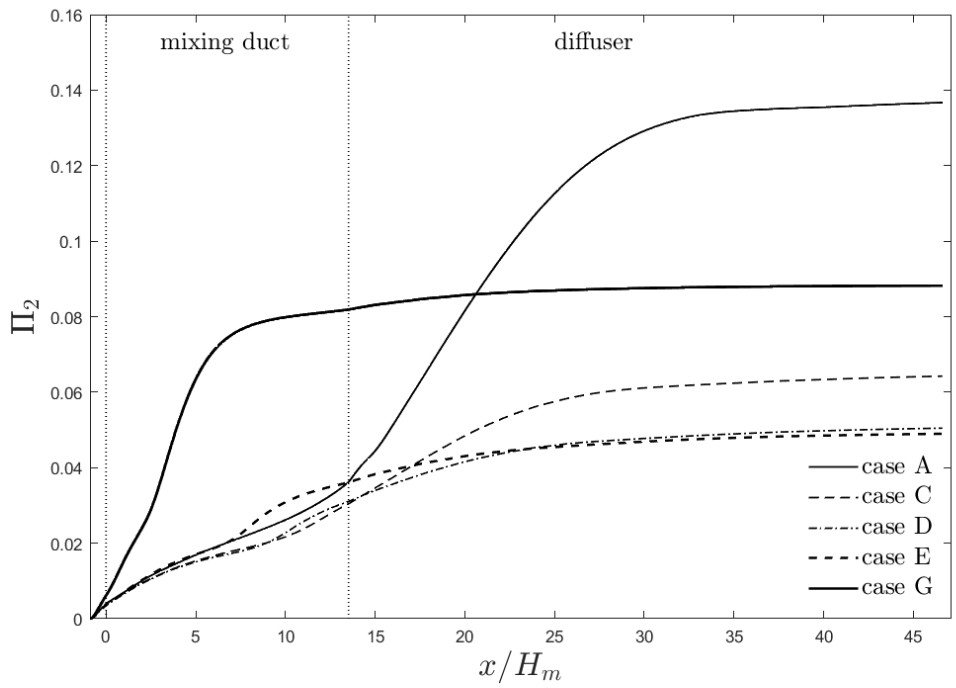

(a) viscous dissipation

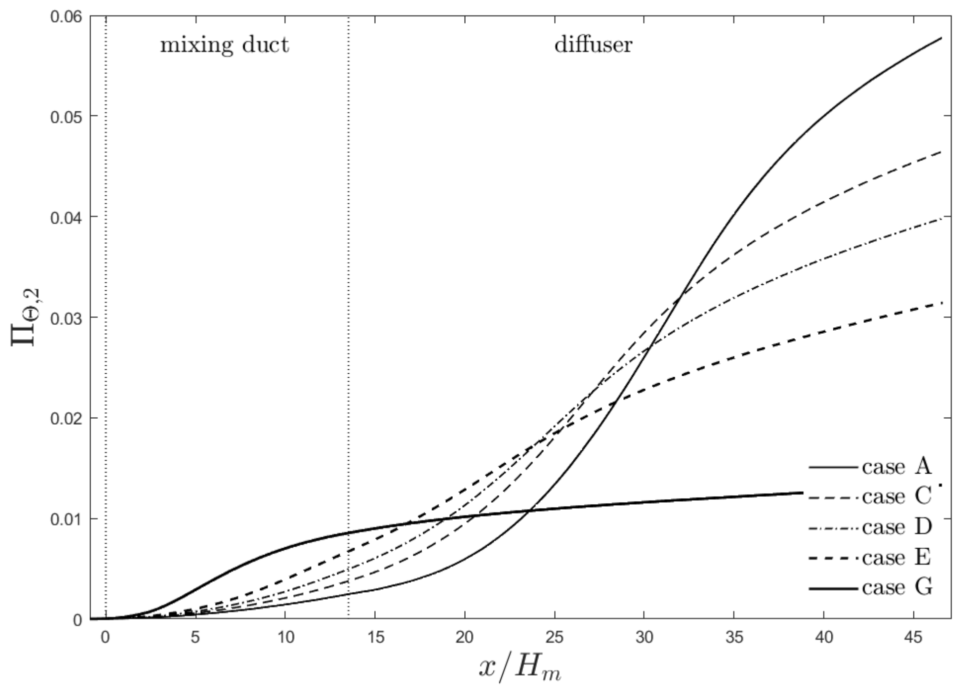

(b) heat transfer

Figure 3.16: Dimensionless cumulative mean-flow total exergy destruction related to (a) viscous dissipation and (b) heat-transfer in the secondary stream for different values of the back-pressure - $p_{01}/p_{02} = 3.61$.

3.5.5 Global exergy balance

As seen in the two previous sections, the sole analysis of the transfers of momentum, mean-flow kinetic energy and exergy is not sufficient to capture the net gain in exergy in the secondary stream. The reason behind lies in the contribution non-negligible of irreversibilities. Hence, a new indicator, $\Delta_2(x_b)$, is introduced to quantify the global net gain in exergy. This value corresponds to the cumulative transfer of exergy, $I_\xi(x_b)$, reduced by the exergy losses occurring within the secondary stream, $\Pi_2(x_b)$ and $\Pi_{\Theta,2}(x_b)$. In a dimensionless form, the relation is written as follows:

$$\Delta_2(x_b) = I_K(x_b) + I_q(x_b) - \Pi_2(x_b) - \Pi_{\Theta,2}(x_b) \tag{3.19}$$

Furthermore, as the global transfer of exergy and global losses are different in amplitude between both geometries, this net gain in exergy indicator allows the two geometries to be compared. To summarize the achieved results, Figs 3.17 and 3.18 show the evolution with the back-pressure of the different dimensionless quantities that have been introduced in the present section for the 2 geometries, respectively. Only the global parameters are considered in these figures. Note that $I_q(x_b)$ is not shown to avoid overloading the figure. It may be represented as the difference between $I_\xi(x_b)$ and $I_K(x_b)$. The results have been represented in the same way as those of Lamberts et al. [27] for ease of reading.

Rectangular ejector

In Fig. 3.17, it appears that the global transfer of total exergy, $I_\xi(x_b)$, decreases with increasing back-pressure. As mentioned above, the exergy transfer is mainly related to the kinetic energy of the mean flow, $I_K(x_b)$, accounting on average for 87% of the total exergy. As a reminder, the global value of $I_\xi(x_b)$ represents the percentage of exergy of the primary flow that is transferred to the secondary: i.e. $I_\xi = 0.58\%$ for Point A. However, due to losses, the net exergy gain remains small. Concerning the global transfer of momentum, it is consistent with the global transfer of kinetic energy, and both parameters give the same value for on-design operations. However, from a certain value of back-pressure, $I_m(x_b)$ and $I_K(x_b)$ start to differ. For the energy losses due to viscous dissipation, $\Pi_2(x_b)$, the curve decreases towards a minimum value of losses and then increases. The minimum value corresponds perfectly to the critical back pressure of the ejector (Point E), as well as to the maximum exergy gain of the secondary flow, $\Delta_2(x_b)$.

Axisymmetric ejector

As may be seen in Fig. 3.18, multiple differences from the rectangular case are visible in the figure and are highlighted in this section. Firstly, $I_K(x_b)$ represents

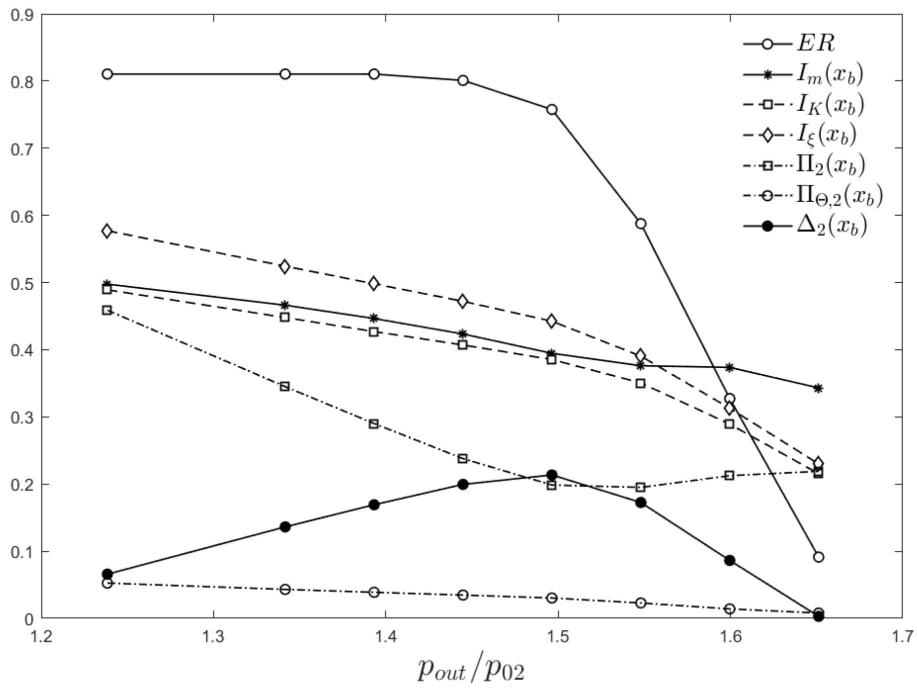

Figure 3.17: Global value of the different indicators - rectangular ejector - $p_{01}/p_{02} = 3.61$

on average ±95% of $I_\xi(x_b)$. The two curves considered are very close and overlap at certain operating condition in the off-design mode (Point F, G, H). Compared to the rectangular case, the kinetic energy of the mean flow curve ($I_K(x_b)$) is almost identical and in the same range of value. The geometry has therefore no significant influence on the transfer of kinetic energy. The main difference between both geometries lie on the exergy losses and more especially the losses related to the viscous dissipation, $\Pi_2(x_b)$. The magnitude is four times smaller in the axisymmetric geometry $(0.1 - 0.2)$ than in the rectangular geometry $(0.3 - 0.5)$. Moreover, the curve shows another minimum at a lower back-pressure, characterizing the critical back-pressure (Point D). This value is also related to the maximum net gain in exergy $\Delta_2(x_b)$. For the second losses, the global losses related to the heat transfer, $\Pi_{\Theta,2}(x_b)$, are similar to the rectangular case, while the local transfer curves are strongly different (see Figs. 3.13b and 3.14b). Finally, in both cases of geometry, the shape of the net gain in exergy curve follows approximately the shape of the entrainment ratio. On the one hand, in the rectangular case, the transition between the on-design and off-design is more marked for ER- and $\Delta_2(x_b)$-curves. While, on the other hand, in the axisymmetric case, the transition is smoother. This coincidence is not surprising, as the entrainment rate is directly related to the net exergy gain in the secondary flow. What are surprising is the high value of net gain in exergy a low back-pressure. In the rectangular case, a net increase of $\Delta_2(x_b)$ is visible in the on-design mode. The secondary flow gains more and more exergy to reach a higher output pressure, a greater capacity to produce work. Whereas in the axisymmetric geometry, the values of $\Delta_2(x_b)$ curves are high in the on-design mode and increases slowly. These results are unexpected and more investigations must be performed

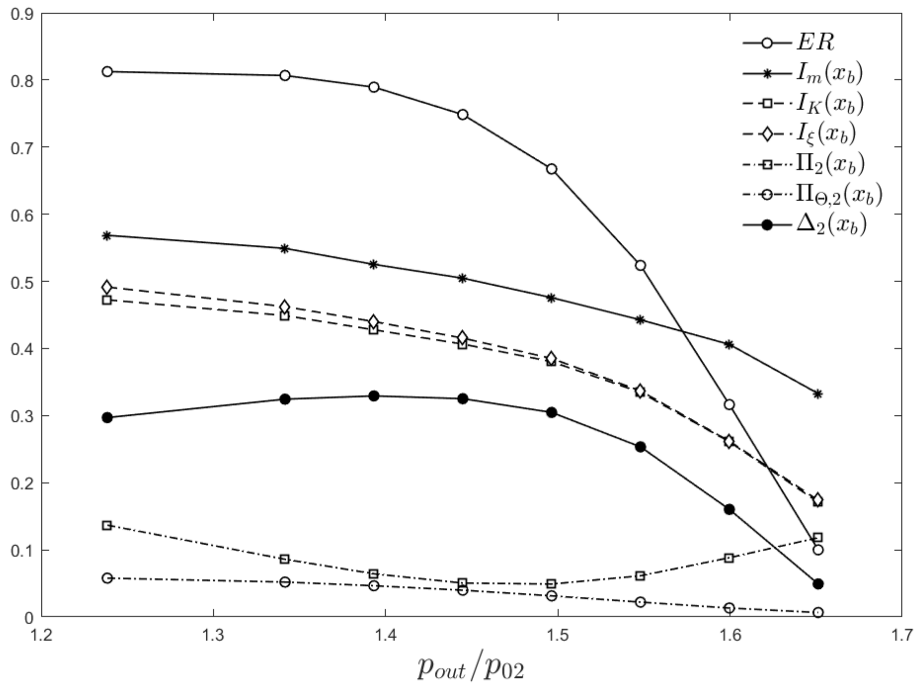

Figure 3.18: Global value of the different indicators - axisymmetric ejector - $p_{01}/p_{02} = 3.61$

3.6 Upgraded axisymmetric ejector

As mentioned previously, the mixing between both streams is not yet completed at the exit of the mixing duct (see Section 3.5.2 : Local transfers). Therefore, it would be interesting to lengthen the mixing duct to improve the mixing phenomena and the performance of the ejector. Indeed, the difference in critical back pressure between the two geometries can be explained by the length of the mixing duct, and more precisely by the mixing duct length ratio: $r_{\text{mixing}} = l_{\text{mixing}}/H_m$. In the axisymmetric ejector setup, only the lengths and the area ratios are maintained, and not the length ratio. As a consequence, the value of these ratios differs from the rectangular case : $r_{\text{mixing}} = 20.74$ to the axisymmetric case : $r_{\text{mixing}} = 13.52$.

Recently, Pianthong et al. [37] and Varga et al. [43], indicate that the mixing duct length has no significant effect on the entrainment ratio but influences the critical back pressure. This latter value increases with l_{mixing} up to an optimal length and remains constant beyond. From a physical point of view, in the mixing chamber, the secondary flow mixes with the primary flow and a transfer of momentum occurs. They accelerate together until the entry of the diffuser, where the flow velocity decreases by expansion. The longer the mixing duct length, the higher the velocity at the entry of the diffuser and the higher the critical back pressure. This length is optimal when the transfer of momentum between both streams is completed in the mixing duct. Beyond this value, the mixing length has no more influence and the critical back pressure remains constant.

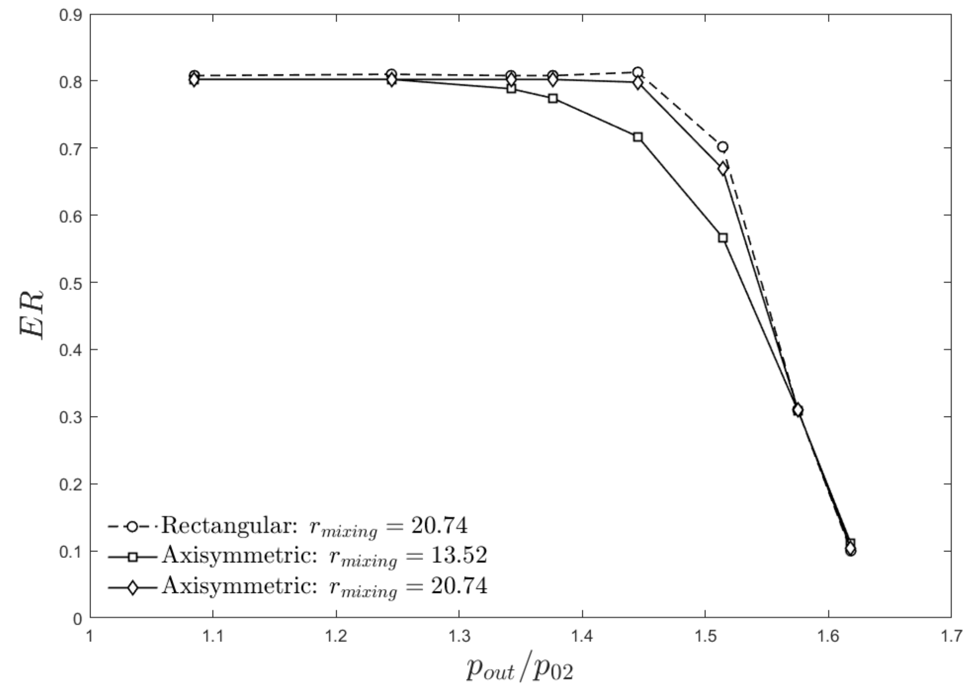

Figure 3.19: Comparison of numerical characteristic curves obtained on a rectangular and axisymmetric ejectors with different r_{mixing} for $p_{01} = 3.50$ [bar].

Fig. 3.19 displays the characteristic curve of a new axisymmetric ejector respecting

the length ratio instead of the length. The applied boundary conditions correspond to those reported in the validation (Table 2.3, p. 29) in order to use these results in subsequent experiments. Both ejectors with the same $r_{\text{mixing}} = 20.74$, present the same operating curve and same critical back pressure. Hence, the length ratios must be conserved between both geometries. It shows that in order to improve the operating range of the outlet pressure, it is important to pay attention to the mixing transfer and the mixing duct length.
Regarding the on-design mode, the entrainment ratio are the same. Indeed, as outlined in several 1D models (*Fabri-chocking* and *compound-choking* theory), the entrainment ratio mainly depends on the boundary conditions and the area ratio A_m/A_t. Since the ratio is maintained between the axisymmetric and rectangular ejector, the entrainment is also maintained.

To conclude this section, multiple indicators have been introduced to quantify the location of transfers and irreversibilities within the ejectors. For each geometry, the global value of the different indicators was calculated and compared between them. The main difference between the axisymmetric and the rectangular characteristic curve lies in the exergy losses related to viscous dissipation and heat transfer between the two flows. Indeed, their amplitudes are four times smaller in the axisymmetric case than in the rectangular case. In addition, the critical back pressure is lower in the axisymmetric case, but further analysis shows that it depends mainly on the length ratio of the mixing duct, r_{mixing}. Further research is needed to optimize this ratio.

3.7 Compound-choking theory

As highlighted in the literature, the *compound-choking* theory is in the good agreement to predict the on-design entrainment ratio of a supersonic ejector ($\delta = \pm 10\%$). Lamberts et al. [28] studied the limitation of its assumptions. To the author's knowledge, the impact of the geometry, as well as the impact of primary temperature, have not been studied yet and are investigated here. The section is structured as follows: a brief review of the theory and assumptions, a comparison between the two geometries and finally the impact of temperature.

3.7.1 Computational procedure

The compound-compressible flow theory was first proposed by Bernstein et al. [5] to analyse the behaviour of one or more gas streams flowing through a single converging-diverging nozzle. This one-dimensional theory shows that the behaviour of each stream is influenced by the presence of the other streams. The compound-choking theory states that for fixed inlet conditions and reducing the outlet pressure, there is a point where information cannot propagate upstream even if the individual stream is still subsonic. The flow is compound-choked. This theory is not described in detail here, as well as the mathematical expressions. For further information, the reader should refer to the paper [5, 28, 13]. However, a reminder of the main assumptions of the compound-choking theory is presented :

1. The flow is one-dimensional, steady, adiabatic and isentropic.

2. Each flow stream is a perfect gas with constant thermodynamic properties.

3. The static pressure is constant across all streams and only varies in the stream wise direction.

By identifying the flow in supersonic ejectors as a two-stream compound compressible nozzle flow, the computational procedure simply consists in simultaneously solving two algebraic equations, derived from the work of Bernstein et al. [5]. A more detailed explanation on the compound-choking theory and the obtained equations are presented in the appendix B. From the geometrical compatibility condition ($A_1(x) + A_2(x) = A_m$), the first algebraic equation is given by

$$\begin{aligned}\frac{\dot{m}_2}{\dot{m}_1}\sqrt{\frac{T_{02}}{T_{01}}} = &\left\{\frac{A_m}{A_1^*}\left[\left(\frac{2}{\gamma-1}\right)\left(\frac{\gamma+1}{2}\right)^{\frac{\gamma+1}{\gamma-1}}\right]^{1/2}\right.\\ &\left.-\left(\frac{p_{01}}{p_{eq}^*}\right)^{1/\gamma}\left[1-\left(\frac{p_{eq}^*}{p_{01}}\right)^{\frac{\gamma-1}{\gamma}}\right]^{-1/2}\right\}\\ &\times\left[1-\left(\frac{p_{eq}^*}{p_{02}}\right)^{\frac{\gamma-1}{\gamma}}\right]^{1/2}\left(\frac{p_{02}}{p_{01}}\right)\left(\frac{p_{eq}^*}{p_{02}}\right)^{1/\gamma}, \end{aligned}\tag{3.20}$$

The flow choked condition ($\beta = 0$, the *compound-flow indicator*) may be rewritten as

$$\frac{\dot{m}_2}{\dot{m}_1}\sqrt{\frac{T_{02}}{T_{01}}} = \left(\frac{p_{02}}{p_{01}}\right)^{\frac{\gamma-1}{\gamma}}\frac{\left\{\frac{\gamma-1}{2}\left[\left(\frac{p_{eq}^*}{p_{01}}\right)^{\frac{1-\gamma}{\gamma}}-1\right]^{-1}-1\right\}\left[1-\left(\frac{p_{eq}^*}{p_{02}}\right)^{\frac{\gamma-1}{\gamma}}\right]^{1/2}}{\left\{1-\frac{\gamma-1}{2}\left[\left(\frac{p_{eq}^*}{p_{02}}\right)^{\frac{1-\gamma}{\gamma}}-1\right]^{-1}\right\}\left[1-\left(\frac{p_{eq}^*}{p_{01}}\right)^{\frac{\gamma-1}{\gamma}}\right]^{1/2}}\tag{3.21}$$

where p_{eq}^* represents the static pressure corresponding to the compound-choking sonic regime ($\beta = 0$). Applying to the supersonic ejector, the area A_1^* is equal to the area of the throat of the primary nozzle A_t, and A_m is considered as the geometrical throat of the compound-compressible nozzle. Four dimensionless quantities $\dot{m}_2\sqrt{T_{02}}/\dot{m}_1\sqrt{T_{01}}$, p_{01}/p_{02}, A_m/A_1^* and p_{eq}^*/p_{02} can be identified in these equations. Hence, for a specific boundary condition p_{01}/p_{02}, γ, T_{01}/T_{02} and a specific geometry configuration A_m/A_t, the simultaneous resolution of the two algebraic equations provides the entrainment ratio $\dot{m}_2/\dot{m}_1$, as well as the value of the static pressure p_{eq}^*. As the area ratio is conserved between the two geometries, the 1D model establishes an equivalence of the results, which will be verified in the next section.

3.7.2 On-design entrainment ratio

Lamberts et al. [28] confirmed the ability of the *compound-choking* theory to predict the on-design entrainment ratio for a rectangular ejector, and this ability is extended for the axisymmetric case. The performances of the numerical simulations and of the compound-choking theory to predict the on-design ratio for different reservoir conditions are assessed in Fig. 3.20. The relative gap between the 2D RANS simulations and the simplified model decreases when the primary stagnation pressure, p_{01}, increases. For the axisymmetric case, the difference is close to 6.3% for

$p_{01}/p_{02} = 2.58$ and falls to 0.7% for $p_{01}/p_{02} = 5.16$. While for rectangular case, this difference also decreases from 4.1% for $p_{01}/p_{02} = 2.58$ to 1.0% for $p_{01}/p_{02} = 5.16$. Hence, for different reservoir conditions and geometry, the *compound-chocking* model yields almost the same prediction of the entrainment ratio as the CFD model.

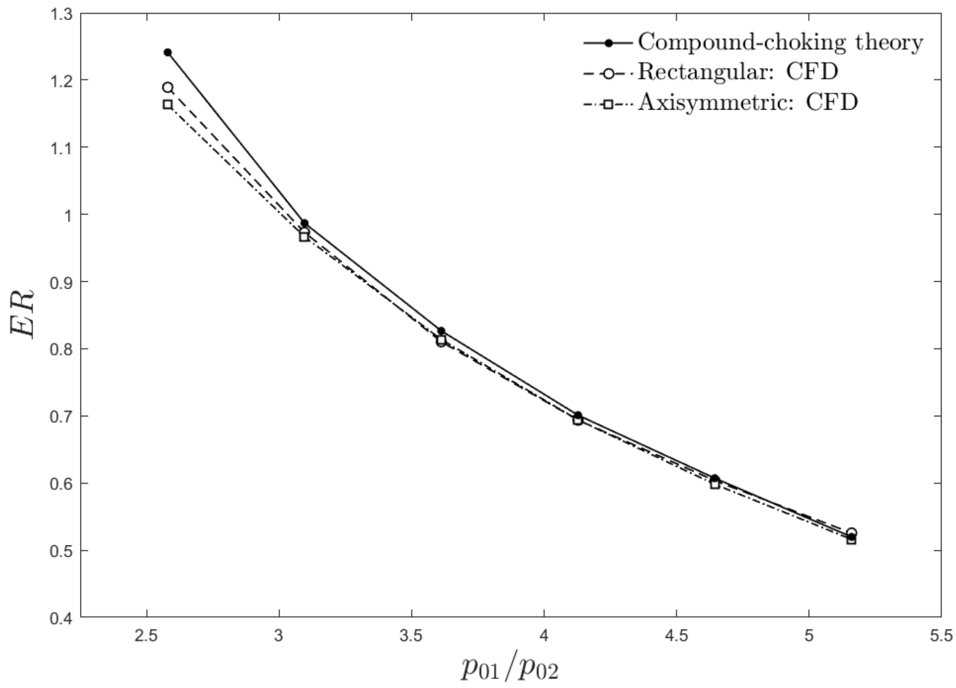

Figure 3.20: Comparison of the on-design entrainment ratio predicted by the CFD model and by the compound-choking theory on the adapted axisymmetric setup for different reservoir conditions.

Unfortunately, experimental results are missing for the axisymmetric ejector. However, the experimental data of Lamberts et al. [28] (not show in the Fig. 3.20) reveals that both approaches slightly overestimate the experimental entrainment ratios. The error made by the CFD model is comprised between 5.6% and 7.2% and the error made by the simplified model is comprised between 6.8% and 10.2%.

The prediction of the primary and of the secondary mass flow rates are also examined separately. As may be seen in Fig. 3.21, the primary mass flow rate obtained by the 1D model is in very good agreement with the numerical results for both geometry cases. The maximum relative error is around 2.1% for the rectangular case, and 1.1% for the axisymmetric case. The small difference between both geometries regarding the entrainment ratio is related to the prediction of the secondary mass flow rate, $\dot{m}_2$. This is evidenced in Fig. 3.22. For the rectangular case, the maximum difference between *compound-choking* theory and the CFD model raises the value of 6.0% and the value of 7.5% for the axisymmetric case.

Finally, based on Fig. 3.20, it appears that the performances of the compound-choking is in very good agreement with the numerical results of the axisymmetric and rectangular ejector. This result is expected since Lamberts et al. tested the ability of this model over a wide spectrum of supersonic ejectors with variable geometry. But is the performance still reliable over a wider range of temperature. This issue will be addressed in the next section.

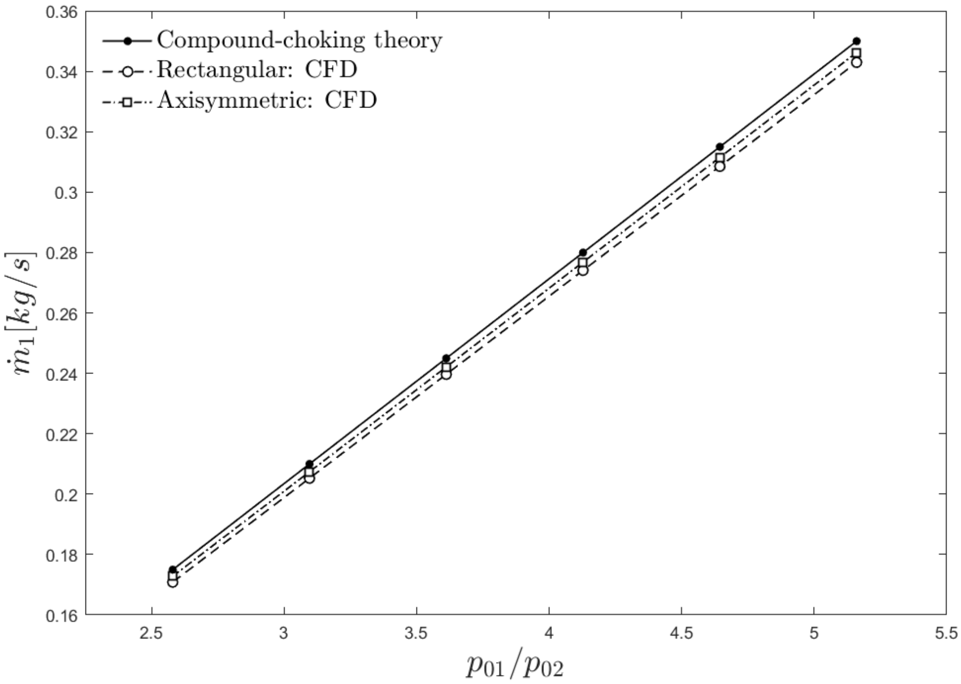

Figure 3.21: Comparison of the primary mass flow rate predicted by the CFD model and by the compound-choking theory on the adapted axisymmetric setup for different reservoir conditions.

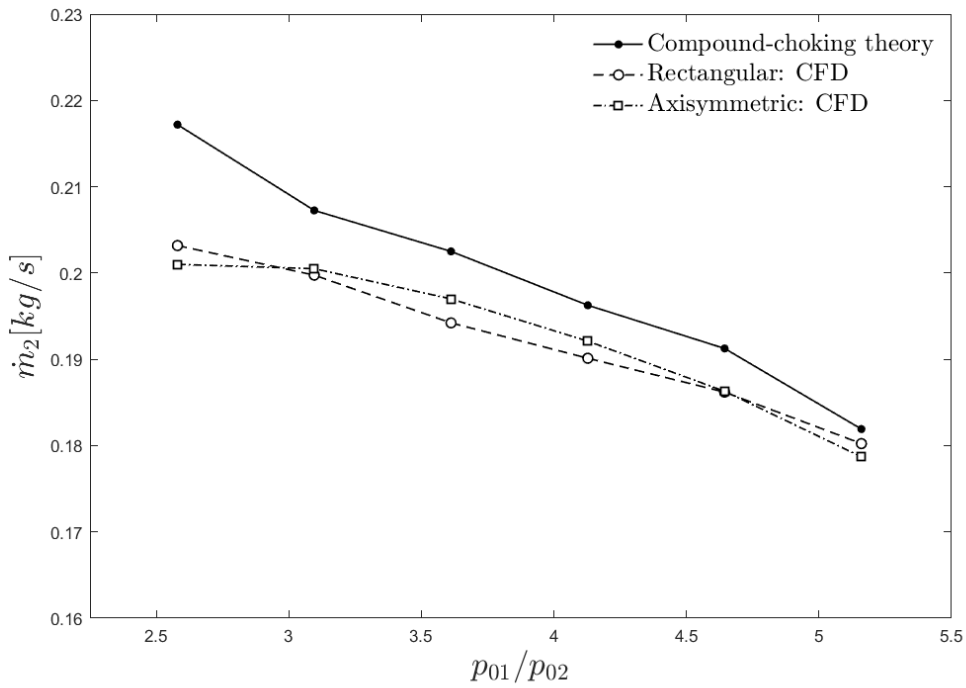

Figure 3.22: Comparison of the secondary mass flow rate predicted by the CFD model and by the compound-choking theory on the adapted axisymmetric setup for different reservoir conditions.

3.7.3 Impact of the primary temperature

The *compound-choking* theory to predict the on-design entrainment ratio has been validated for different geometries, not yet for different temperatures. This section is devoted to the capacity of this 1D model to predict the entrainment ratio over a wider range of temperature at the inlet. Due to lack of experimental data, the results of the simplified model are only compared with the numerical simulations of the axisymmetric ejector (later built at UCL). To the knowledge of the authors, the impact of the primary temperature has never been assessed in the literature.

The comparison between the *compound-choking* theory and the CFD is shown in Fig. 3.23 as a function of T_{01}/T_{02}. It appears that, for the geometry considered, the agreement between the compound-choking theory and the numerical simulations varies with the reservoir conditions. The relative difference between both predictions is very small for the lowest values of the primary stagnation temperature : $\simeq 1.2\%$ for $T_{01}/T_{02} = 1$ and 1.5. As T_{01} increases, the entrainment ratio increases, and the gap between the theory and the CFD increases also : 7.0% for $T_{01}/T_{02} = 3$.

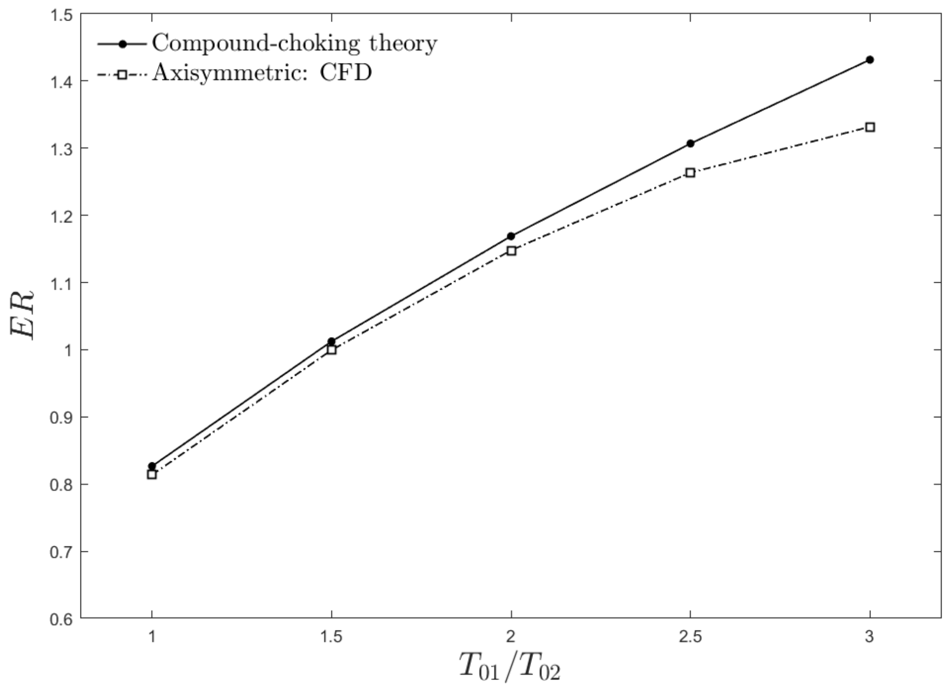

Figure 3.23: Comparison of the on-design entrainment ratio predicted by the CFD model and by the compound-choking theory on the adapted axisymmetric setup for different temperature conditions.

The overestimation of the entrainment ratio caused by the *compound-choking* theory is explained by the difference between both approaches regarding the assumptions. Compared to the numerical simulations, the *compound-choking* theory neglects the two-dimensional and the non-isentropic aspects of the flow. The entrainment limitation is essentially considered as an isentropic process. In that case, the main difference in the results should lie in the hypothesis of a constant static pressure profiles. In order to validate this assumption, the profile of the static pressure, is examined at the choking position, x_c (see Fig. 1.5, p. 11). The position is computed by post-processing the numerical results. The reader is reminded that x_c is defined, for an on-design operating point, as the first axial position where the equivalent Mach number, M_{eq} reaches unity (see appendix B).

However, due to the low and identical pressure ratio $p_{01}/p_{02} = 3.61$ for each case, the static pressure profile is nearly uniform in both streams and identical for each case, as shown in Fig. 3.24, for three different temperature ratios. As a result, the difference in the hypothesis of a constant pressure profiles does not explain the overestimation of the entrainment ratio at high temperature.

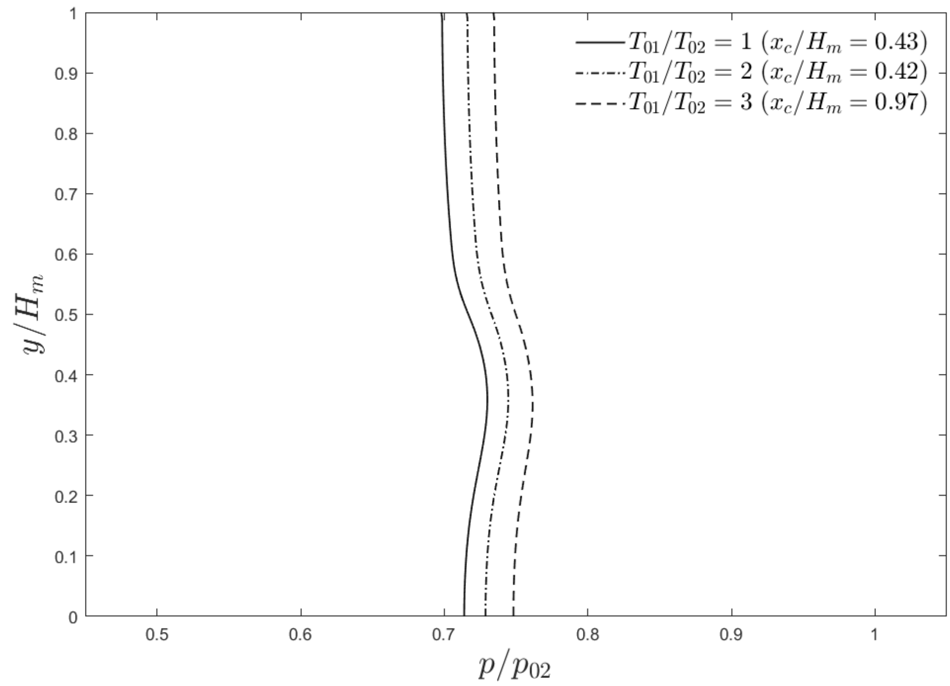

Figure 3.24: Static pressure profile at the choking position for different values of T_{01}/T_{02}. The centreline and the wall and the wall of the mixing duct correspond to $y/H_m = 0$ and $y/H_m = 1$, respectively.

The difference in the results should lie in another assumptions. As mentioned previously, the *compound-choking* theory considered the entrainment limitation as an adiabatic and isentropic process. Indeed, a high difference of temperature at the boundaries involves a high temperature gradient at the outlet of the primary nozzle. Therefore, a transfer of heat occurs between the primary and secondary flow at this location and each stream is no longer assumed to be adiabatic.

In order to verify these assumptions, the heat exchange is investigated along the dividing streamline (see Fig. 3.4, p. 36). As may be seen in Fig. 3.25, the heat flux Q, occurs contradicting the adiabatic hypothesis and increases with the difference of temperature T_{01}/T_{02}. The exergy analysis had also concluded that a transfer of heat occurs between the two streams. Hence, the flow is no longer isentropic. Indeed, by post-processing the numerical results, the difference in entropy in the secondary flow at position x ($s_2(x)$) and at the reference state (s_{ref}), is computed by the volume integral, in the same way as the exergy losses:

$$s_2(x) - s_{ref} = \iiint_{V_2(x)} s - s_{ref} \; dV \tag{3.22}$$

and for a calorically perfect gas, as a reminder, the entropy is given by

$$s - s_{ref} = c_p \ln\left(\frac{T}{T_{\text{ref}}}\right) - R \ln\left(\frac{p}{p_{\text{ref}}}\right) \tag{3.23}$$

The results is shown in Fig. 3.26. A close inspection of the curves reveals that the entropy of the secondary stream s_2, increases as heat is exchanged from the primary stream. Following the 1D assumption, the entropy should remain constant until the choking position, x_c. As evidenced in the curves, the secondary flow is no longer isentropic. Nevertheless, in the case of $T_{01} = T_{02}$, the entropy of the secondary flow remains more or less identical to the reference entropy s_{ref}. In that condition, the process can be assumed isentropic and the prediction of the 1D model is well good, with a difference of 1.2% to the CFD model.

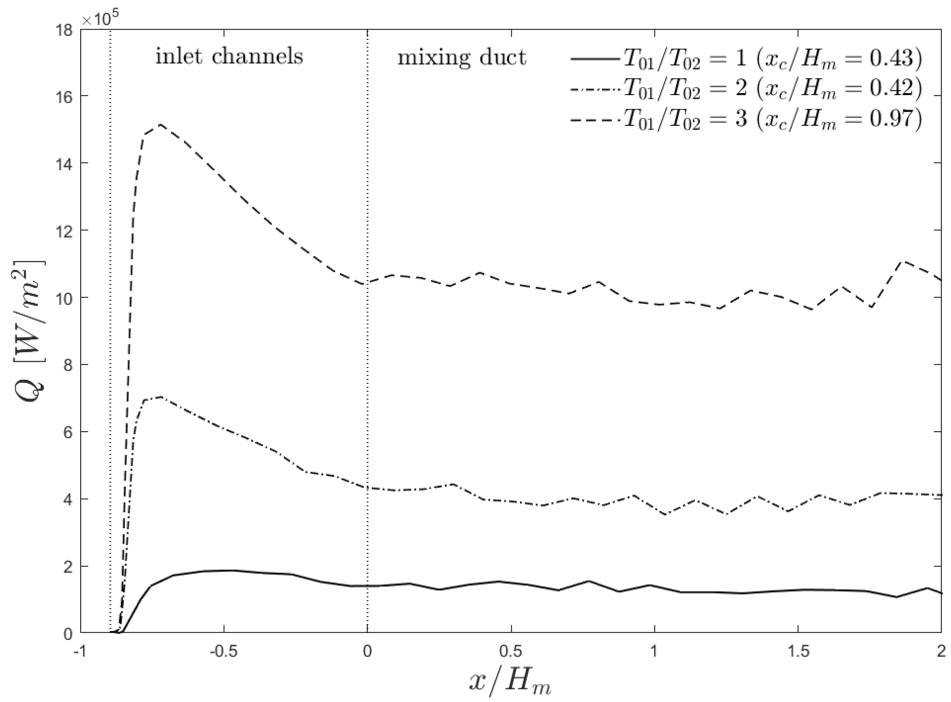

Figure 3.25: Heat flux crossing the dividing surface for different values of temperature - $p_{01}/p_{02} = 3.61$

To summarize the compound-choking section, this model predicts correctly the same entrainment ratio for both geometries, with a maximum error around 5%. The result is not surprising because the area ratio A_m/A_t, is preserved between the geometries, as well as the boundary conditions. However, when heating the primary flow, the 1D theory fails to accurately predict the on-design entrainment

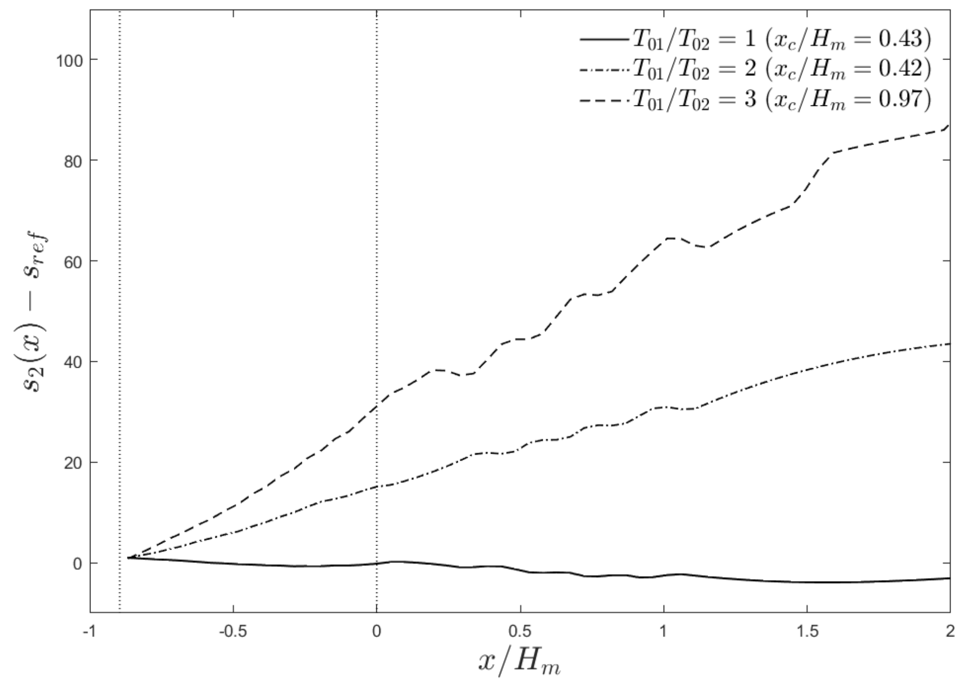

Figure 3.26: Entropy in the secondary stream for different values of temperature - $p_{01}/p_{02} = 3.61$

ratio due to the restrictive assumption of isentropic flow. Indeed, as raised in the numerical simulations, a transfer of heat occurs in the inlet channels, before the choking position, x_c.

Chapter 4

Analysis of 2 transient scenarios

4.1 Introduction

As the literature points out, the authors are mainly interested in the stationary behaviour of the ejector. However, there are few comprehensive studies on the transient mode. This chapter aims to fill the knowledge gap in this area. Many transient scenarios are possible: variation of pressure, mass flow rate, temperature... In this chapter, the focus is on one of these scenarios: the closing of the secondary valve. This process generates a vacuum chamber in the secondary channel, as in high altitude test facilities. Before presenting the results, further details are given on the calculation method and an error estimate is made to assess the accuracy of the CFD in transient mode. Then, the results are presented in depth, from evacuation performance to response time. Due to the two operating modes identified (started and un-started), two valve closures were performed, one in each mode, and compared with each other.

4.2 Computation detail

As mentioned in the methodology, the transient scenario is simulated with the $k - \epsilon$ RNG model due to its fast convergence and lower computational time. As a reminder, the computational domain corresponds to the mesh with $50,958$ elements (reported in Fig. 2.6). Regarding the flow solver, the method and discretization of the equations are identical to those of the stationary case. In terms of time, the integration is carried out using the second order implicit scheme with a fixed time step of 10^{-6} [s]. A simple check of the Courant number validates this choice. Indeed, in order to lead to accurate solutions and physical results, the Courant number must be less than 1, which gives a time step of 2×10^{-6} [s] for our supersonic ejector geometry.

Since the transition from the steady to a transient solver induces some variations ($\pm 0.5\%$), it is important to stabilize the solution of the flow in the transient mode before starting the scenario (1.5 [ms]).

4.3 Precision estimation

The CFD accuracy in a transient simulation results in the accumulation of computational errors after the end of each time step. This error increases with the number of time steps. Therefore, it becomes necessary to calculate the error where the unsteady problem is simulated over a large number of time steps. This error depends on the accuracy of the schemes used and the spatial resolution. In the present study, all the schemes used are second order accurate. A brief explanation regarding the error computation is given in the appendix C.

The error estimate for the present simulation is presented in Table 4.1. Since the mesh structure and total domain size remain the same for all the cases, the error estimation will be nearly the same for all the cases. Hence, the error estimation for only one case has been reported in the table.

Error estimate	
Simulated physical time	0.1 [s]
Time steps	1×10^{-6} [s]
Total accumulated error	0.347%
Allowable error (S_L)	1%
Allowable number of time steps (n_{max})	5.10×10^5
Reliability	5.10

Table 4.1: Precision estimation

As may be seen in the table, the simulated physical time is 0.1 [s]. This value is more than sufficient given that the studied scenarios last only a few milliseconds. The total accumulated error is around 0.347% and the reliability factor around 5.10. This ratio shows that how far the maximum allowable error (1%) is from the actual error. The higher is the ratio, the lower is the error. In this case, the number of time steps can still be increased, and the present simulation is sufficiently far away from the maximum limit. As a result, the error is controlled and the CFD accuracy of the transient simulation is guaranteed.

4.4 Scenario : Closure of the secondary valve

First, the scenario studied in this manuscript is the closing of a valve at the secondary inlet. A zero mass flow rate is imposed on it, generating a low-pressure chamber at the inlet of the secondary channel. These vacuum chambers have several application areas, such as high altitude test facilities, used for testing upper rocket engines. This section aims to improve the understanding and description of this phenomenon, and in particular the stabilization time of the vacuum chamber. The final objective is to obtain a mathematical model of this process.

For this purpose, our scenario will be simulated numerically. In our study case of valve closure, the secondary flow must be imposed at zero ($\dot{m}_2 = 0.0$ [kg/s]). However, as mentioned in the methodology, all input conditions are imposed using pressure and temperature. Therefore, it is necessary to switch from a pressure condition to a mass flow condition at the secondary inlet. First, an initial simulation is performed with pressure boundary conditions to obtain the secondary flow inlet rate. Subsequently, a second simulation is performed by imposing the secondary flow rate, previously obtained. Fixing the secondary flow in an ejector may be considered unintuitive, since the secondary flow is entrained from the atmosphere and not fixed by it. The numerical results are identical, and this mass flow condition allows us to impose our zero flow scenario. As highlighted above, the variations, following the solver changes, stabilize at 1.5 [ms]. Therefore, from this value onwards, the flow rate at the secondary inlet becomes discontinuously zero.

4.4.1 Evacuation performance

Before studying the time phenomenon, it would be interesting to study the discharge performance of the ejector. In other words, what will be the pressure at the inlet of the secondary channel for a wide range of inlet and outlet conditions ? This value will allow assessing whether our scenario has converged to its stable solution. This performance is called the evacuation performance (EP) characterized by $EP = p_2/p_A$, the ratio between the static pressure in the vacuum chamber (p_2), and the ambient pressure (p_A). The outlet pressure (p_{out}) can also be considered instead of the atmospheric pressure in the definition of the evacuation performance. However, since the outlet of the ejector corresponds to the atmosphere in the experiments and the reference pressure is usually the ambient pressure, p_A is used instead. Fig. 4.1 shows the evolution of the evacuation performance curve against the primary pressure.

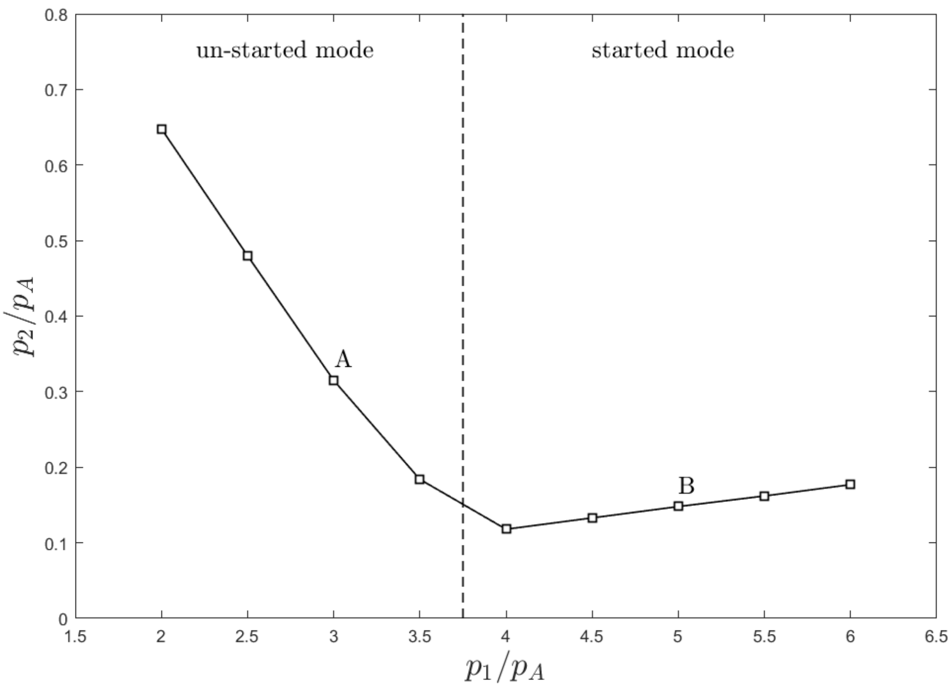

Figure 4.1: Evacuation performance (EP) of a supersonic ejector - $p_A = 1.0$ [bar].

As observed on the figure, the evacuation performance decreases sharply in a first phase, reaches a minimum at $p_1/p_A \simeq 3.75$ and increases slightly in a second phase. Two modes can then be distinguished. These modes of operation are termed as the *started mode*, and *un-started mode*, respectively. To better understand this, the flow phenomena within the ejector is investigated.

Before displaying any flow structures, let's study about the expected results. As a reminder, in this study case, the output condition is the atmosphere and does not vary. Firstly, in a nozzle, as the inlet pressure increases and exceeds a certain critical pressure, the fluid becomes sonic at the throat, accelerates into the diffuser and continues its expansion at the diffuser outlet, bounded by the spreading jet. Two different cases can therefore be identified. Indeed, when the primary pressure is low (Point A), the expansion is lower and the spreading jet does not attach the wall of the mixing duct (as may be seen in a schematic way in Fig. 4.2a for a vacuum ejector). There is a distance in between, so-called "hypothetical distance" by analogy with the 1D model of the supersonic ejector (see Fig. 1.4, p. 10). In another hand, when the primary pressure is high (Point B), the primary jet is full expands and attaches to the wall, isolating the vacuum chamber from the downstream condition. A train of shocks occurs to comply to the downstream condition (see Fig. 4.2 b). As the inlet pressure increases, this shock train moves towards the outlet exit. The optimal condition corresponds to a normal shock within the mixing duct. Finally, the vacuum condition at the secondary inlet is caused by the pumping action of the primary jet.

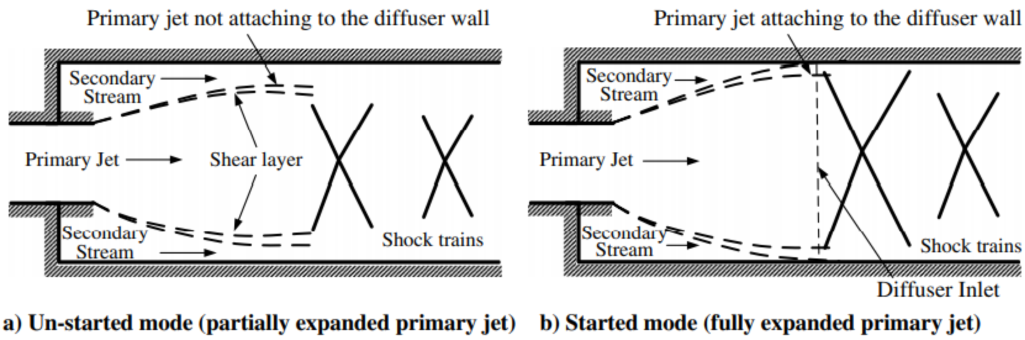

Figure 4.2: Schematic showing un-started and started modes of vacuum ejector [2]

.

As mentioned above, the evacuation performance reaches a minimum value around $p_1/p_A \simeq 3.75$, characterizing the transition between the 2 modes. From a flow point of view, it corresponds to the situation where the primary jet fits perfectly with the mixing duct and a normal shock occurs. Under these assumptions, it is possible to compute this optimum value with the normal shock theory. For an isentropic flow, the area/pressure ratio relations in terms of Mach number is given by :

$$\frac{A_t}{A_m} = \left(\frac{\frac{(\gamma+1)}{2}}{\left(1+\frac{(\gamma-1)}{2}M_1^2\right)}\right)^{\frac{(\gamma+1)}{2(\gamma-1)}} M_1 \tag{4.1}$$

$$\frac{p_{01,opt}}{p_A} = \left(1+\frac{(\gamma-1)}{2}M_1^2\right)^{\frac{\gamma}{(\gamma-1)}} \frac{\frac{(\gamma+1)}{2}}{\left(\gamma M_1^2-\frac{(\gamma-1)}{2}\right)} \tag{4.2}$$

where M_1 is the Mach number at the shock. By solving these two equations, one after the other, the optimal value $p_{01,opt}$ can be found. In our geometry case with $A_m/A_t \simeq 4.51$, the optimal ratio is given by $p_{01,opt}/p_A = 3.76$, which matches quite well with the results of the CFD model. Moreover, the vacuum pressure at the secondary inlet is equal to the pressure at the normal shock given by:

$$\frac{p_2}{p_A} = \frac{\frac{(\gamma+1)}{2}}{\left(\gamma M_1^2-\frac{(\gamma-1)}{2}\right)} \tag{4.3}$$

Which results in $p_2/p_A = 0.093$. Once again, it matches with the CFD simulations. These equations above can be used in another sense. Indeed, for a given p_{01}, these relations calculate the $A_{m,max}/A_t$ required for the starting mode. If the cross-section of the mixing duct A_m is greater than $A_{m,max}$, the mode is *un-started*. Otherwise, is the area ratio is lower, the mode is *started*.

To validate the reasoning, the flow structure of each mode (Point A and B) are investigated and presented in Figs. 4.3 and 4.4. The results are steady and as a reminder, the boundary condition of the secondary inlet is a zero mass flow condition. On the upper half part of the ejector, the Mach contours are displayed and on the lower part, the streamlines are presented. As may be observed, the *un-started* and *started* mode are represented. On Fig. 4.3, the spreading jet does not attach to the mixing duct wall. The spreading line corresponds to the dividing streamline (red line) until the shock train. The upstream state depends on the downstream condition. Recirculation bubbles are also visible in the mixing chamber. These vortex bubbles extend and retract from the secondary chamber as the primary pressure varies. On Fig. 4.4, for the *started* mode, the bubble is completely located inside the secondary channel and the spreading line attaches the wall. To conclude, thanks to the numerical simulations, the existence of the two modes has been shown and validated.

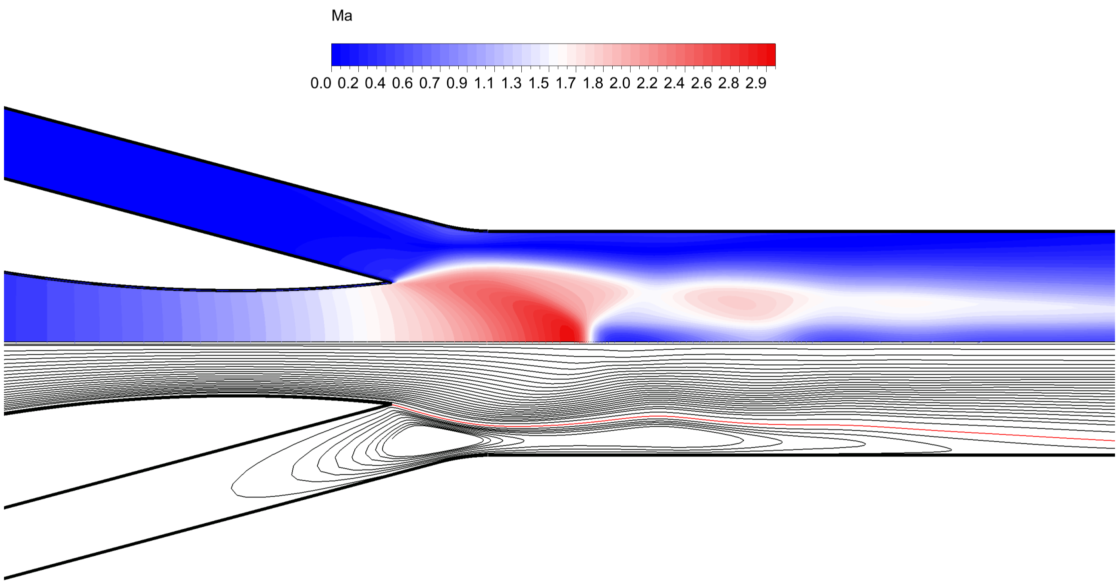

Figure 4.3: Un-started mode : Mach number contours (upper half part) and streamlines (lower half part) of a supersonic ejector with $\dot{m}_2 = 0.0$ [kg/s] - $p_{01}/p_A = 3.0$

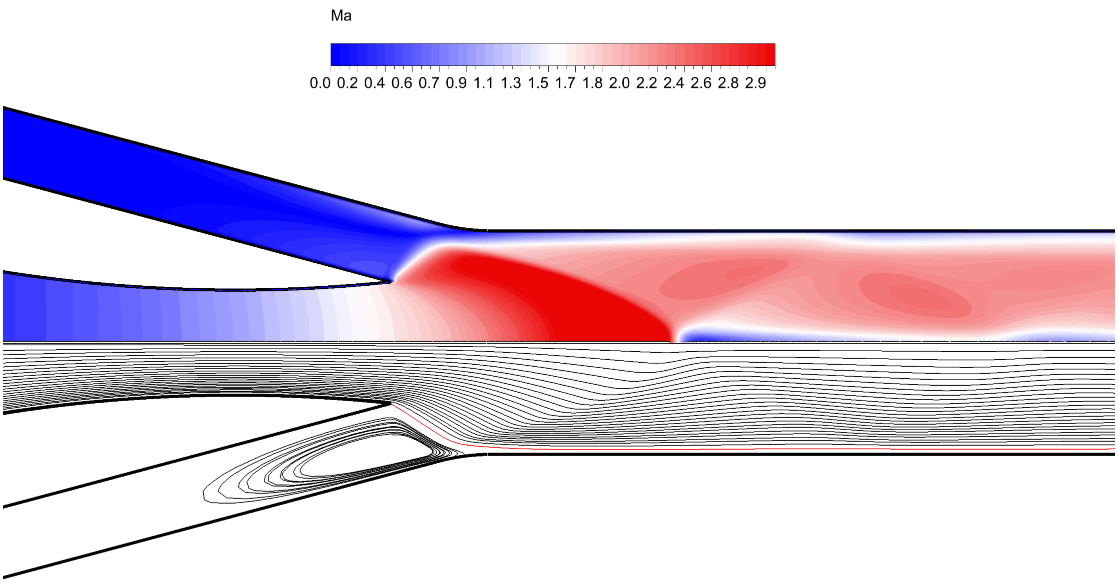

Figure 4.4: Started mode : Mach number contours (upper half part) and streamlines (lower half part) of a supersonic ejector with $\dot{m}_2 = 0.0$ [kg/s] - $p_{01}/p_A = 5.0$

4.4.2 Time response

The studied scenario consists of the closure of a valve at the secondary inlet. Once the stationary solution is stable, at 1.5 [ms], a condition of zero mass flow rate is imposed at the secondary inlet ($m_2 = 0.0$ [kg/s]). The objective of this section is to investigate the response time of the perturbation. For the time being, only the initial and the final state are known thanks to the previous section. Knowing the final state helps to define if your solution has converged or not. Now, the effort is putted on the transition between these two states.

The two studied cases here differ slightly from the evacuation performance simulation. Indeed, the outlet condition is not related to the atmosphere condition. The outlet pressure is equal to 1.20 [bar] and the inlet condition correspond to the on-design operating mode of a supersonic ejector: $p_{01} = 3.50$ [bar] and $p_{01} = 6.00$ [bar] with $p_{02} = 0.969$ [bar]. The reason for this choice is based on the fact that the supersonic ejector is used as a compressor in a refrigeration system, and not as a vacuum generator in a HAT facility. However, this difference will not impact the evacuation performance if the ambient pressure, p_A is imposed at the outlet pressure, p_{out}. By considering this on-design boundary condition, the final solution should be located in the *un-started* mode for $p_{01} = 3.50$ [bar] ($p_{01}/p_{out} = 2.92$) and in the *started* mode for $p_{01} = 6.00$ [bar] ($p_{01}/p_{out} = 5.00$). As a reminder, the optimal evacuation performance is located at $p_{01,opt}/p_{out} = 3.76$.

Our numerical results are presented here. In a first instance, the time evolution of the secondary inlet pressure is shown in Fig. 4.5. This variable is a good criterion for evaluating the response time, as the final state is known. On the figure, each black or white dot represents a data saving. Due to the low computational time step (10^{-6} [s]), the data is only recorded every 1000 time iterations, (or every 1.0 [ms]). As may be observed, for the *un-started* mode, the secondary or vacuum pressure abruptly decreases, oscillates during 3.0 [ms] and stabilizes after 4.0 [ms]. These oscillations are surprising, given that the expected result was maybe a slow and continuous decrease of pressure, such as the *started* mode. At this stage, nothing can explain these variations. Therefore, an in-depth analysis of the flow structure must be performed to explain the origin of the oscillations.

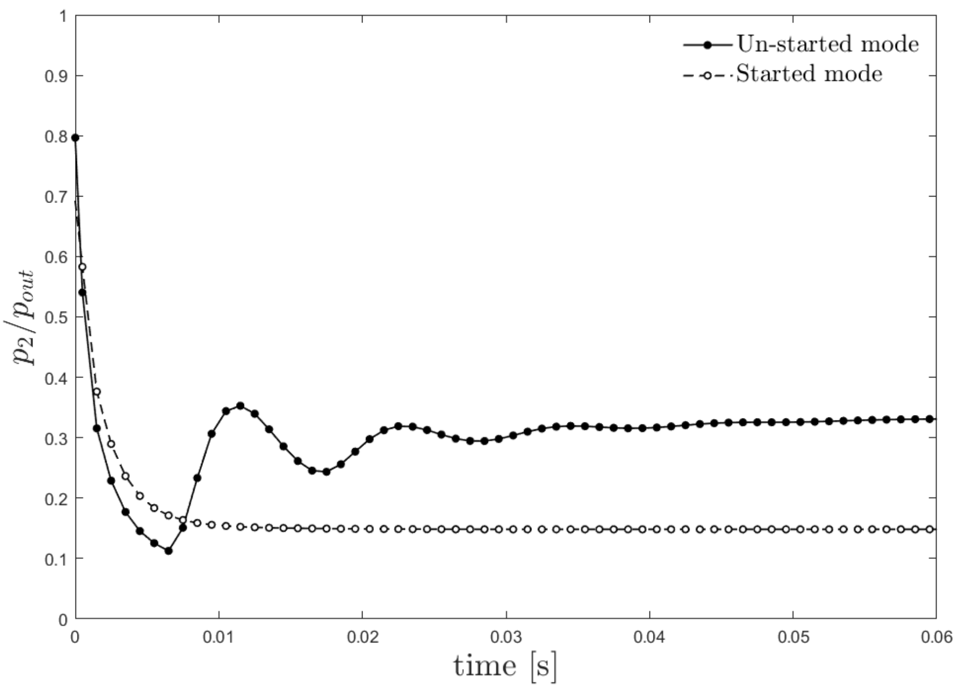

Figure 4.5: Time evolution of the secondary inlet pressure : p_2/p_{out}

It can be marked that the stabilization of the secondary inlet pressure does not necessarily imply the stabilization of the entire flow downstream. Indeed, flow phenomena may occur within the mixing chamber and the diffuser. Therefore, a second criterion is introduced, taking into account both inlet and outlet condition. Fig. 4.6 shows the time evolution of mass flow ratio between the primary inlet and the outlet. As may be seen, the curve increases after 2.0 [ms] (time to be impacted by the perturbation upstream), and oscillates in both cases. However, the stabilization occurs after 5.0 [ms] for the *un-started* mode and after 3.0 [ms] for the *started* mode. For this reason, depending on the case of application, one criterion will be used instead of the other.

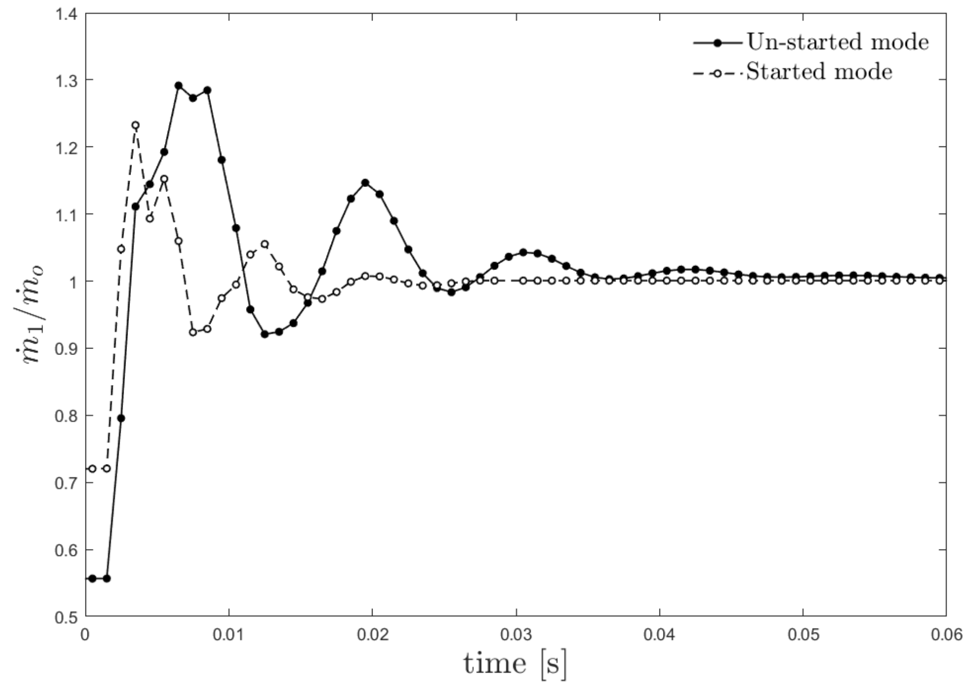

Figure 4.6: Time evolution of the mass flow ratio : $\dot{m}_1/\dot{m}_o$

4.5 Transient scenario

As mentioned in the previous section, oscillations of pressure appear in the vacuum chamber and also at the outlet boundary. An in-depth flow structure analysis must be performed to understand their origin. The perturbation at the secondary inlet occurs at $t = 0.0$ [s]. The numerical results are presented here for different flow time. Each figure is divided into 2 parts. On the upper half, the Mach number contours are plotted with the subsonic flow in blue and the supersonic flow in red, and on the lower half, the streamlines are shown.

4.5.1 Un-started mode

At the initial phase ($t < 0$ [ms], Fig. 4.7a), the valve at the secondary inlet is still opened, and the secondary flow is still entrained due to the high kinetic energy of the primary stream. The streamlines show the flow path of both stream. At the exit of the primary nozzle, the primary flow undergoes shock waves, implying a change of flow direction, not pronounced in this figure. The flow direction does not seem to be disturbed. At $t = 0$ [ms], the secondary valve closes, and the remaining fluid is drawn, decreasing the secondary pressure. Due to the lower pressure outside the primary flow, this primary jet begins to expand and accelerate. At $t = 4$ [ms] (Fig. 4.7b), the spreading line attaches to the mixing duct wall as the started mode and the typical lambda shock structure is more visible. A recirculation bubble appears at the entrance of the secondary channel in the mixing chamber. At $t = 6$ [ms], it is seen from the instantaneous streamlines in Fig. 4.8a that two circulation zones exist in the primary and secondary stream. This circulation bubbles are produced by the upstream displacement of the second shock of the diffuser. These bubbles gain in vortex energy and become larger due to the increasing tangential velocity of the vortex. At the next time, $t = 8$ [ms] (Fig. 4.9a), this vortex bounces on the Y shock pattern and dissipates in the flow downstream. During the same time, the two recirculation bubbles at the wall, merges together, disrupting the low pressure at the secondary inlet (minimum pressure in Fig. 4.5). Secondary recirculation bubbles appear also into the secondary channel (not show in the figure). Finally, these bubbles stabilize into two split bubbles due to the large primary jet expansion. The oscillation of secondary pressure can be explained by the pressure wave moving from the secondary inlet and the flow downstream. This acoustic wave is not captured by a non-reflecting boundary condition at the secondary inlet as the valve is closed from the atmosphere. This condition was only imposed at the outlet. After oscillating, the secondary pressure stabilizes at the final evacuation pressure.

4.5.2 Started mode

In contrast to the un-started mode, the secondary inlet pressure does not oscillate over time (see Fig. 4.5) and decreases continuously to its final evacuation pressure. The in-depth analysis of the flow structure will reveal this difference. At the initial phase ($t < 0$ [ms], Fig. 4.11a), the valve at the secondary inlet is still opened. As the *un-started* mode, at $t = 0$ [ms], the secondary valve closes, and the remaining fluid is drawn, decreasing the secondary pressure. Due to the lower pressure outside the primary flow, this primary jet begins to expand and accelerate. At $t = 4$ [ms] (Fig. 4.12a), the spreading line attaches to the mixing duct wall. A recirculation bubble appears at the entrance of the secondary channel in the mixing chamber.

However, in the primary streams, no circulation bubbles, moving the fluid upwards, appear. Therefore, the spreading line remains attach to the mixing duct wall, isolating the downstream flow. At $t = 10$ [ms] (Fig. 4.13a), the secondary pressure in the vacuum chamber reaches its final performance pressure. The response time is smaller in the started mode.

To conclude, as highlighted in this chapter, the closure of the secondary valve can lead to 2 different modes depending on the primary pressure : *un-started mode* and *started mode*. The difference between these two modes lie on the primary jet that attaches the wall. Depending on the operating mode, the time response is different and an in-depth analysis of the flow structure is needed to explain the reason of the oscillations at the secondary inlet pressure. Now, although the transient flow phenomenon is known, more effort must be devoted to the development of a mathematical model that characterizes the scenario. Efforts and time that the author no longer has.

Un-started mode

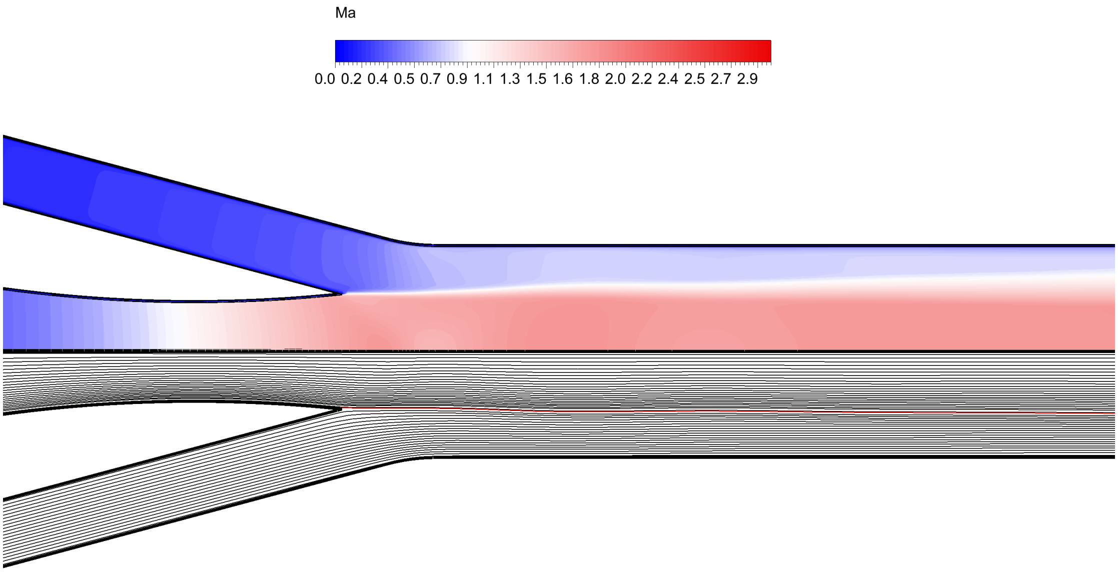

(a) Initial phase $t < 0.000$ [s]

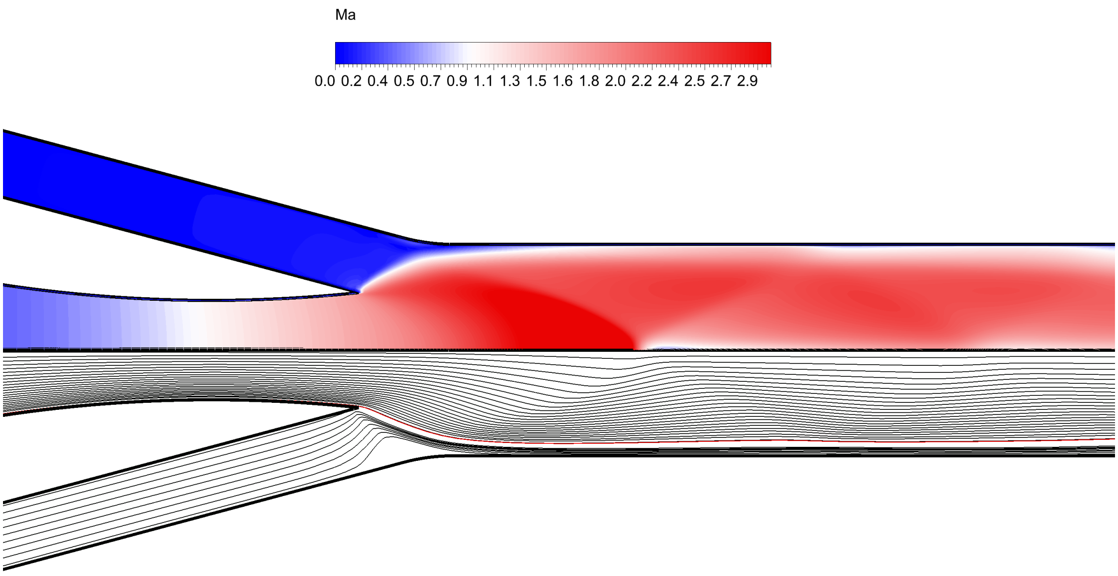

(b) $t = 0.004$ [s]

Figure 4.7: Mach number contours (upper half part) and streamlines (lower half part) of a supersonic ejector at different flow time

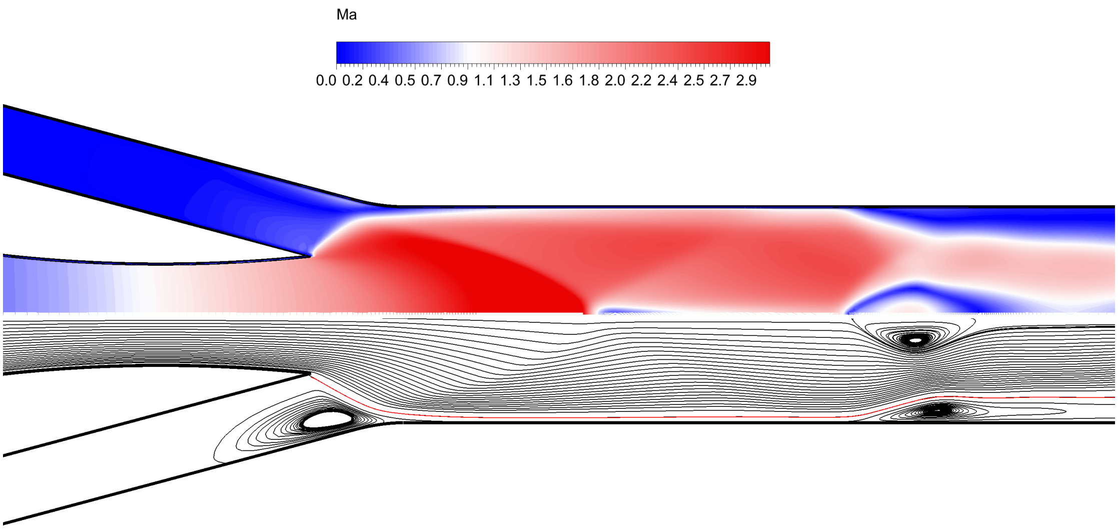

(a) $t = 0.006$ [s]

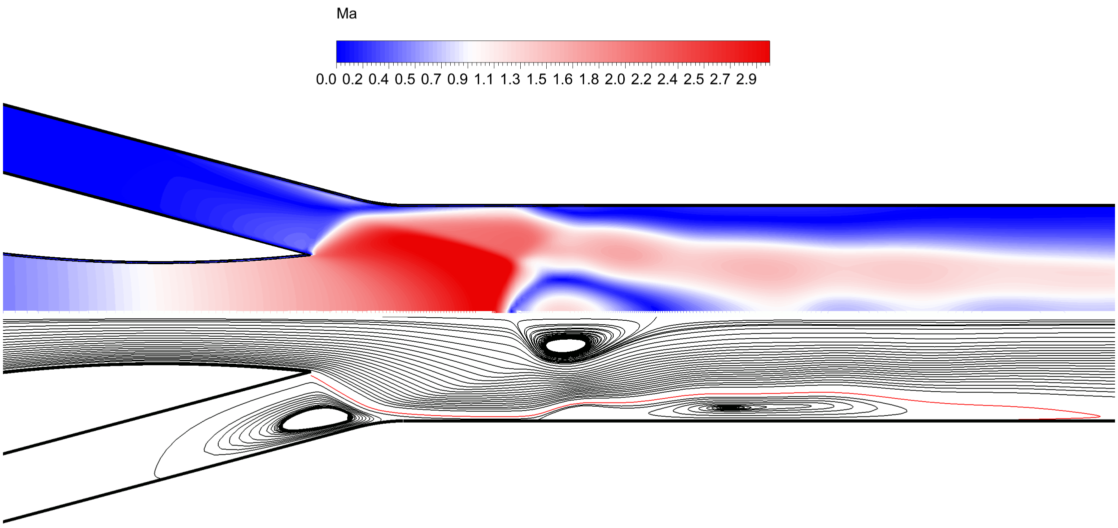

(b) $t = 0.007$ [s]

Figure 4.8: Mach number contours (upper half part) and streamlines (lower half part) of a supersonic ejector at different flow time

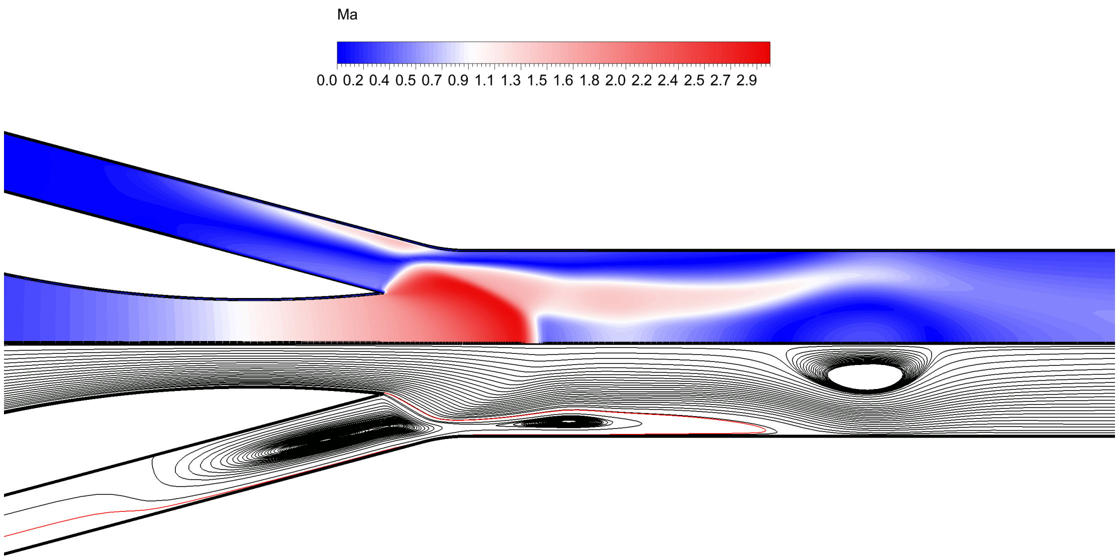

(a) $t = 0.008$ [s]

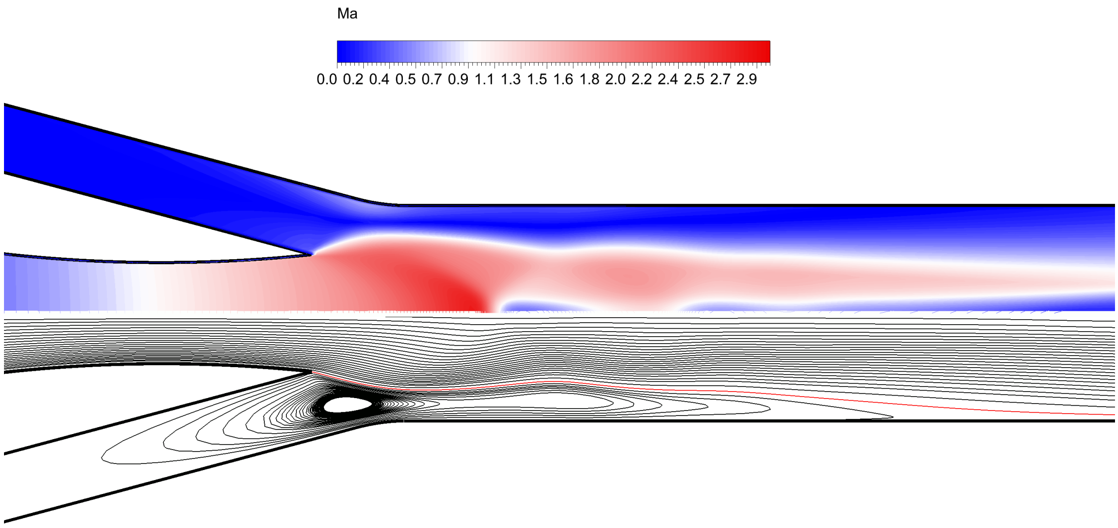

(b) $t = 0.011$ [s]

Figure 4.9: Mach number contours (upper half part) and streamlines (lower half part) of a supersonic ejector at different flow time

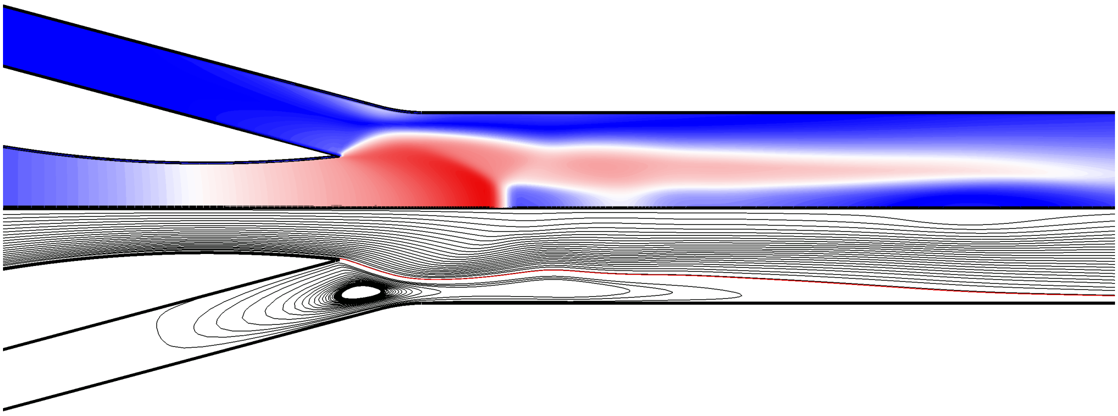

(a) $t = 0.020$ [s]

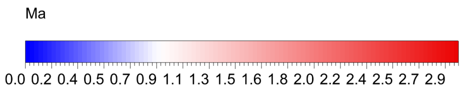

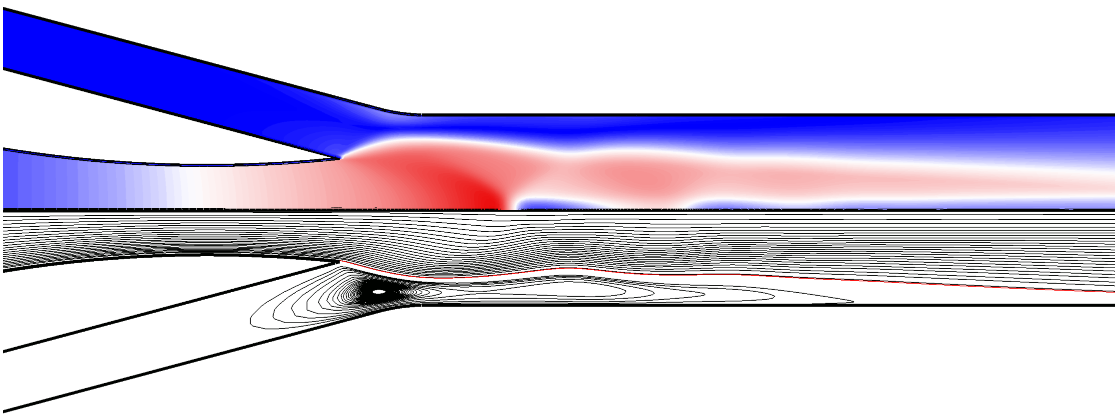

(b) $t = 0.040$ [s]

Figure 4.10: Mach number contours (upper half part) and streamlines (lower half part) of a supersonic ejector at different flow time

Started mode

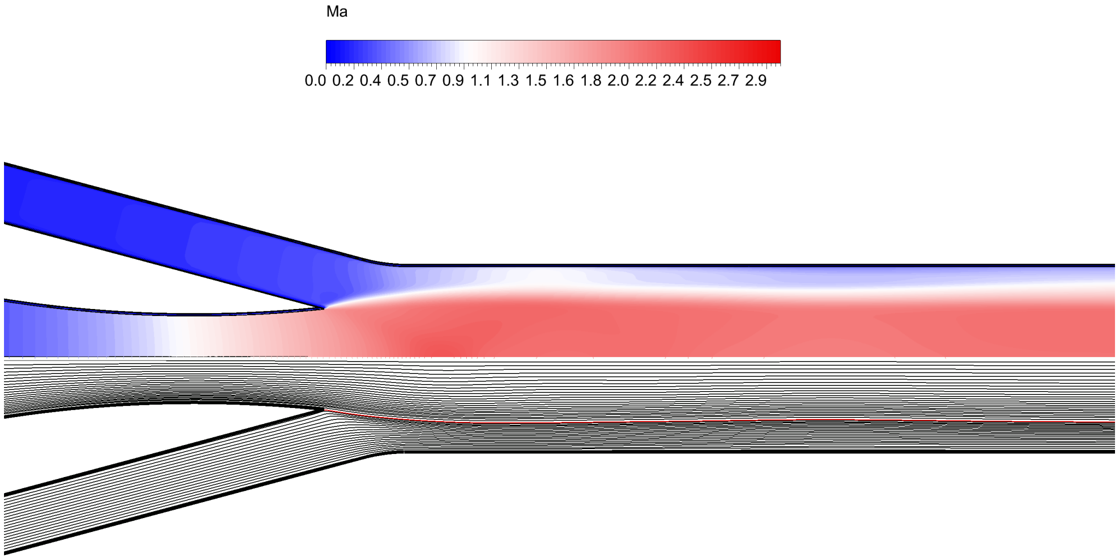

(a) Initial phase $t < 0.000$ [s]

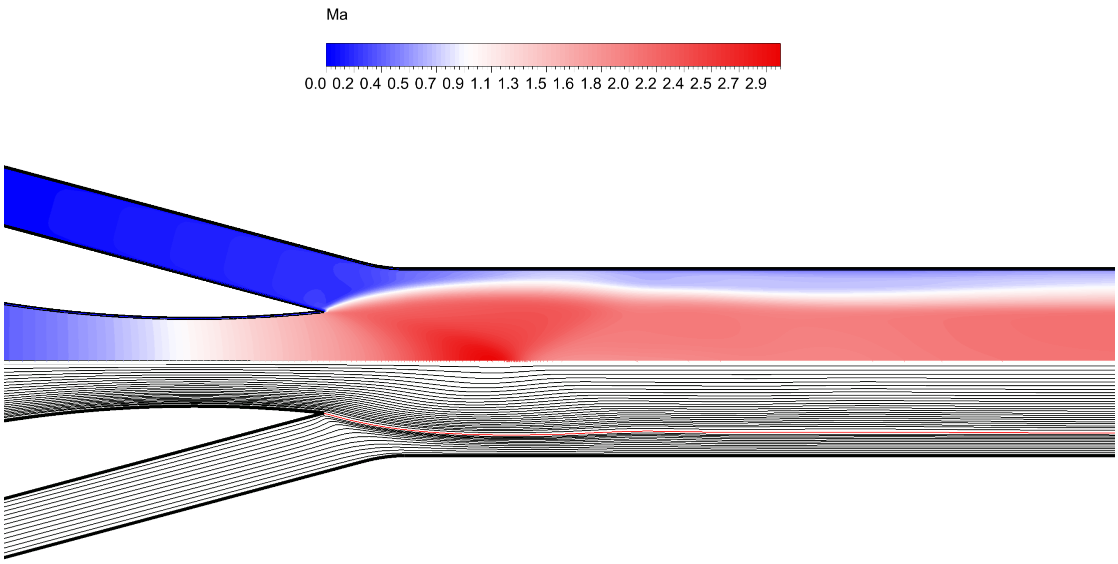

(b) $t = 0.001$ [s]

Figure 4.11: Mach number contours (upper half part) and streamlines (lower half part) of a supersonic ejector at different flow time

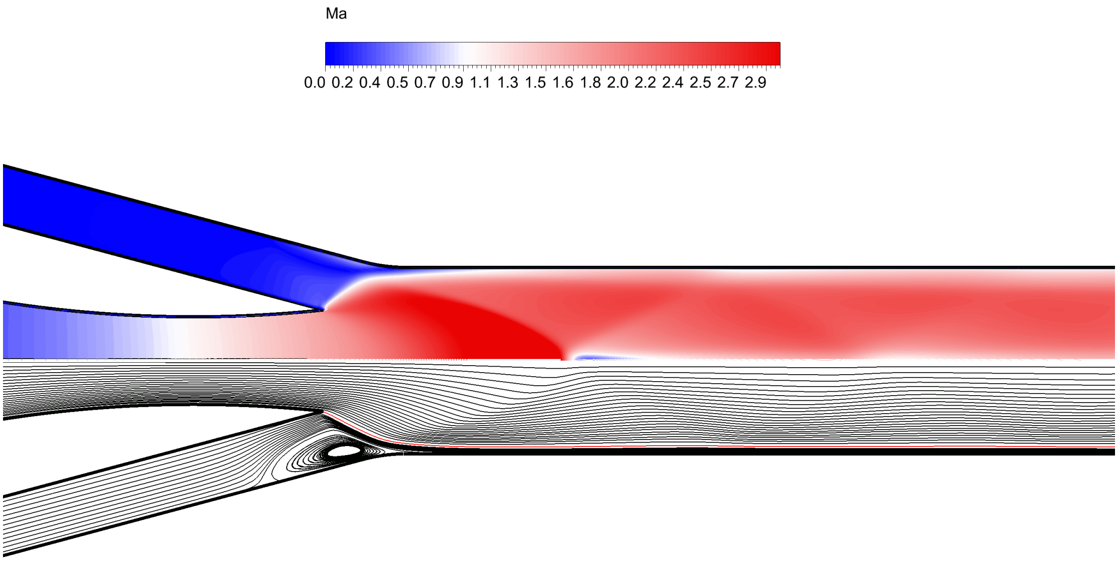

(a) Initial phase $t = 0.004$ [s]

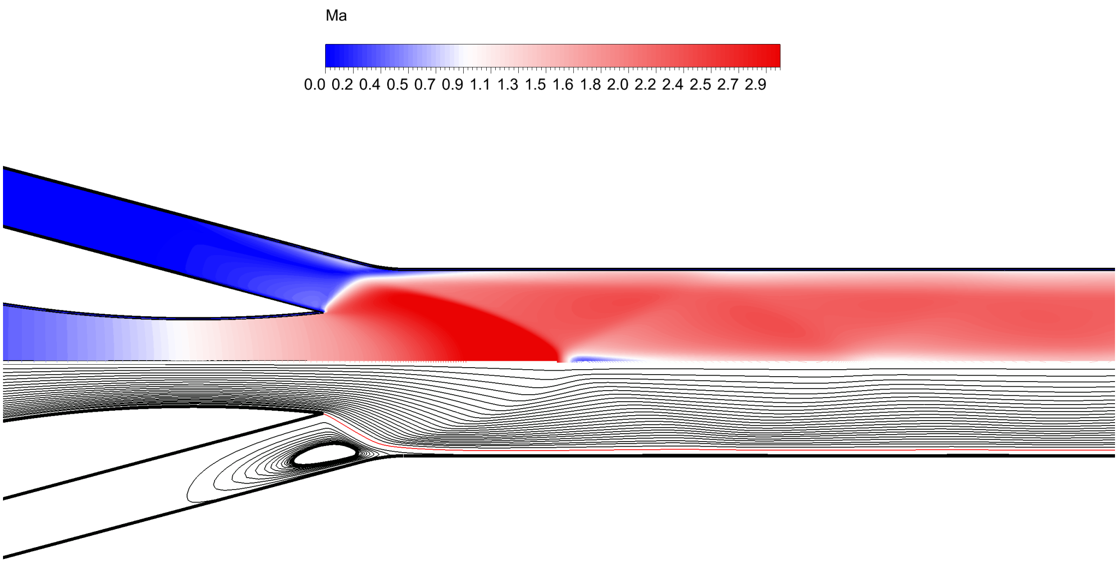

(b) $t = 0.006$ [s]

Figure 4.12: Mach number contours (upper half part) and streamlines (lower half part) of a supersonic ejector at different flow time

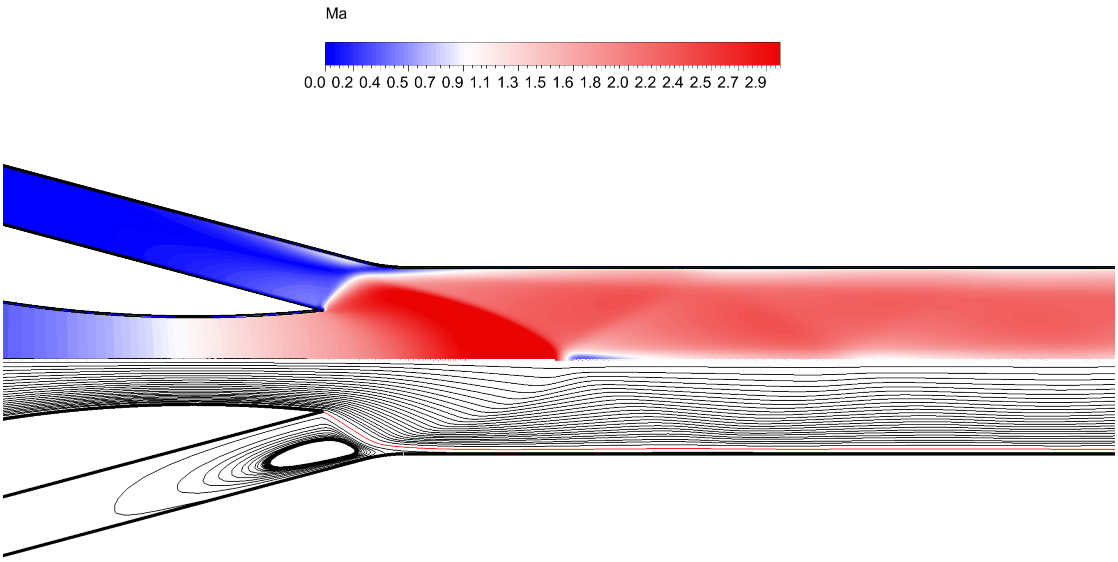

(a) Initial phase $t = 0.010$ [s]

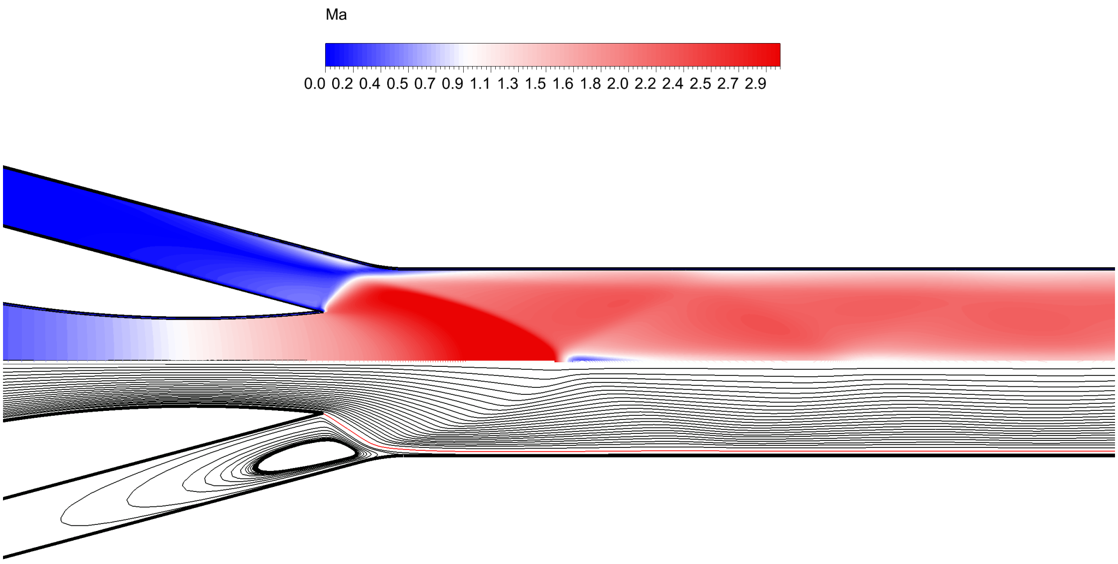

(b) $t = 0.030$ [s]

Figure 4.13: Mach number contours (upper half part) and streamlines (lower half part) of a supersonic ejector at different flow time

Chapter 5

Conclusions and perspectives

The limitation on the performance of supersonic ejectors are mainly related to the choking and the mixing mechanisms at play in such devices. In 2018, Lamberts et al. [29] greatly improved the scientific understanding of these flow phenomena within a rectangular ejector. The perspective of their work is to extend the methodology to a large number of ejector configurations in order to highlight the influence of the different geometrical parameters. Therefore, the first contribution of this paper is to adapt the analysis to an axisymmetric ejector and to study the influence of the geometry.

The approach, presented in Chapter 2, has mainly consisted in thoroughly processing the results of 2D RANS simulations of the flow in both ejector geometries (axisymmetric and rectangular) using air as working fluid. The calculations have been performed with Ansys Fluent (Release 2021 - R1) and the numerical results have been validated at the global and at the local scales with the experimental and numerical simulations of Lamberts et al. [29].

The analysis, carried out in Chapter 3, shows a difference in the characteristic curve and the critical back pressure between the axisymmetric and rectangular ejector. The exergy approach concludes that this difference results from exergy losses related to viscous dissipation and heat transfer between the two flows. Following this analysis, an upgraded ejector is implemented by lengthening the mixing duct in order to improve the mixing phenomena and the critical back pressure. It would therefore be interesting to optimize the length ratio of the mixing duct to enhance the operating range. In addition, the comparison between the two geometries was extended to a 1D model. The *compound-choking* theory is suitable for predicting the entrainment ratio in both cases. However, when heating the primary flow, 1D theory fails to predict accurately due to the restrictive assumption of isentropic flow.

Furthermore, due to the growing interest of unsteady flow phenomena, the second contribution of this thesis is the analysis of a valve closure at the secondary inlet. This process generates a vacuum chamber in the secondary channel, as in high altitude test facilities. As outlined in Chapter 4, the closure of the secondary valve can lead to two different modes depending on the primary pressure: *un-started* mode and *started* mode. Depending on the mode, the time response, evacuation performance and flow structure differ, and the *started* mode is considered more efficient.

Finally, as mentioned through the manuscript, perspectives of this thesis consist of three main paths: (i) optimization of the length ratio of the mixing duct, (ii) improvement of the *compound-choking* theory for a heated primary flow, (iii) the development of mathematical model to characterize the valve closure scenario.

Appendices

Appendix A

Total flux of quantities

Total flux of momentum

Since the linear momentum (Equation 2.2) is a vector quantity, and in the absence of body forces, the transport equation of the momentum in the ζ direction is given by

$$\frac{\partial}{\partial x_j}\left(\underbrace{\hat{u}_j\overline{\rho}\left(\hat{u}_i\zeta_i\right) - \overline{\tau}_{ij}\zeta_i - \overline{\tau}^t_{ij}\zeta_i}_{\overline{F}_{m,j}}\right) = -\frac{\partial\overline{p}}{\partial x_i}\zeta_i \tag{A.1}$$

The left-hand side of the equation consists of the divergence of the vector field of the total momentum $\overline{F}_{m,j}$, in the ζ direction. Since the flow within the ejector and the momentum is nearly aligned with the horizontal/axial direction , $\zeta_i = \mathbf{e}_x$. For a 2D planar flow, the total flux may be rewritten as

$$\overline{F}_{m,x} = \left(\hat{u}\overline{\rho}\hat{u} - \overline{\tau}_{xx} - \overline{\tau}^t_{xx}\right) \tag{A.2}$$

$$\overline{F}_{m,y} = \left(\hat{v}\overline{\rho}\hat{u} - \overline{\tau}_{xy} - \overline{\tau}^t_{xy}\right) \tag{A.3}$$

In our supersonic ejector case, the x-component of the vector field, $\overline{F}_{m,x}$ is mainly determined by the contribution of the advective flux : $\hat{u}\overline{\rho}\hat{u}$. By contrast, the y-component of the vector field, $\overline{F}_{m,y}$ depends mainly on the viscous and turbulent fluxes : $-\overline{\tau}_{xy} - \overline{\tau}^t_{xy}$.

Total flux of kinetic energy

For the determination of energy tubes, the transport equation for the mean-flow kinetic energy $K = \overline{\rho}\hat{u}_i\hat{u}_i/2$ is used to obtain the total flux of kinetic energy, $\overline{F}_{K,j}$:

$$\frac{\partial}{\partial x_j}\left(\underbrace{K\hat{u}_j - \overline{\tau}_{ij}\hat{u}_i - \overline{\tau}^t_{ij}\hat{u}_i}_{\overline{F}_{K,j}}\right) = -\hat{u}_j\frac{\partial\overline{p}}{\partial x_j} - \overline{\tau}_{ij}\frac{\partial\overline{u}_i}{\partial x_j} - \overline{\tau}^t_{ij}\frac{\partial\overline{u}_i}{\partial x_j} \tag{A.4}$$

Therefore, for a 2D planar flow, the total flux of kinetic energy may be rewritten as

$$\overline{F}_{K,x} = \left(K\hat{u} - \overline{\tau}_{xx}\hat{u} - \overline{\tau}^t_{xx}\hat{u}\right) \tag{A.5}$$

$$\overline{F}_{K,y} = \left(K\hat{v} - \overline{\tau}_{xy}\hat{u} - \overline{\tau}^t_{xy}\hat{u}\right) \tag{A.6}$$

Total flux of exergy

As a reminder, the exergy is defined as the maximum theoretical work that can be obtained from an amount of energy. The mean-flow total exergy, ξ^*_t is a state variable defined as follows

$$\xi^*_t = (h^*_t - h_{ref}) - T_{ref}(s^* - s_{ref}) \tag{A.7}$$

where the * indicates that the variable is calculated from the averaged flow quantities. Hence, the mean-flow total enthalpy, h^*_t is defined as $h^*_t = \hat{h} + \hat{u}_j\hat{u}_j/2$. The symbol s represents the entropy. The subscript ref refers to the reservoir conditions of the secondary stream as the reference state, namely $T_{ref} = T_{02}$ and $p_{ref} = p_{02}$.

From the transport equation of the mean-flow total enthalpy, of mean-flow specific entropy, and mass conservation, Lamberts et al. [27] expressed the transport equation of ξ^*_t and obtained the vector field $\overline{F}_{\xi,j}$:

$$\frac{\partial}{\partial x_j}\left[\underbrace{\hat{u}_j\left(\overline{\rho}\xi^*_t\right) + \left(\overline{q}_j + \overline{q}^t_j\right)\left(1 - \frac{T_{\mathrm{ref}}}{\hat{T}}\right) - \overline{\tau}_{ij}\hat{u}_i - \overline{\tau}^t_{ij}\hat{u}_i}_{\overline{F}_{\xi,j}}\right] = -T_{\mathrm{ref}}\left(\frac{\Phi}{\hat{T}} + \frac{\Phi_\Theta}{\hat{T}^2}\right) \tag{A.8}$$

For further information about the development of the equation, the reader should refer to [27]. Therefore, for a 2D planar flow, the vertical and horizontal components of the total flux of exergy may be rewritten as

$$\overline{F}_{\xi,x} = \hat{u}\left(\overline{\rho}\xi^*_t\right) + \left(\overline{q}_x + \overline{q}^t_x\right)\left(1 - \frac{T_{\mathrm{ref}}}{\hat{T}}\right) - \overline{\tau}_{xx}\hat{u} - \overline{\tau}^t_{xx}\hat{u} \tag{A.9}$$

$$\overline{F}_{\xi,y} = \hat{v}\left(\overline{\rho}\xi^*_t\right) + \left(\overline{q}_y + \overline{q}^t_y\right)\left(1 - \frac{T_{\mathrm{ref}}}{\hat{T}}\right) - \overline{\tau}_{xy}\hat{u} - \overline{\tau}^t_{xy}\hat{u} \tag{A.10}$$

The 2 terms of the right-hand side of the equation, Φ and Φ_Θ are related to the entropy generation by viscous dissipation and by heat transfer, respectively, expressed as follows :

$$\Phi = \overline{\tau}_{ij}\frac{\partial \hat{u}_i}{\partial x_j} + \overline{\tau}^t_{ij}\frac{\partial \hat{u}_i}{\partial x_j} \tag{A.11}$$

$$\Phi_\Theta = -\left(\overline{q}_j + \overline{q}^t_j\right)\left(\frac{\partial \hat{T}}{\partial x_j}\right) \tag{A.12}$$

Applying $\overline{F}_{\xi,j}$ to the exergy transport, we obtain :

$$\iint_{A_{in}} \overline{F}_{\xi,j} n_j \; ds + \iint_{A_{out}} \overline{F}_{\xi,j} n_j \; ds = -T_{\text{ref}} \iiint_\Omega \left(\frac{\Phi}{\hat{T}} + \frac{\Phi_\Theta}{\hat{T}^2}\right) \; dV \tag{A.13}$$

where $\mathbf{n}$ is the outward directed normal to the control volume, Ω. Hence, the difference of exergy between inlet A_{in} and the outlet A_{out} is caused by the integral effects of sinks, due to negative sign. It means that the flux of total exergy going out of a transport tube is lower than the flux entering the tube.

Total flux of heat transfer

Regarding the heat transfer between the primary and the secondary stream, the focus should be put on its exergy content. Hence, the flux of exergy associated with the mean heat flux and the turbulent transport of heat is defined as

$$\overline{F}_{q,j} = \left(\overline{q}_j + \overline{q}^t_j\right)\left(1 - \frac{T_{\text{ref}}}{\hat{T}}\right) \tag{A.14}$$

Therefore, for a 2D planar flow, the total flux of exergy content of heat may be rewritten as

$$\overline{F}_{q,x} = \left(\overline{q}_x + \overline{q}^t_x\right)\left(1 - \frac{T_{\text{ref}}}{\hat{T}}\right) \tag{A.15}$$

$$\overline{F}_{q,y} = \left(\overline{q}_y + \overline{q}^t_y\right)\left(1 - \frac{T_{\text{ref}}}{\hat{T}}\right) \tag{A.16}$$

Appendix B

Compound-choking theory

A more detailed explanation on the compound-choking theory and the obtained equations are presented here. The compound-choking theory of Bernstein et al. [5] has been derived from the concept of a one-dimensional compound-compressible nozzle flow, shown in Fig. B.1.

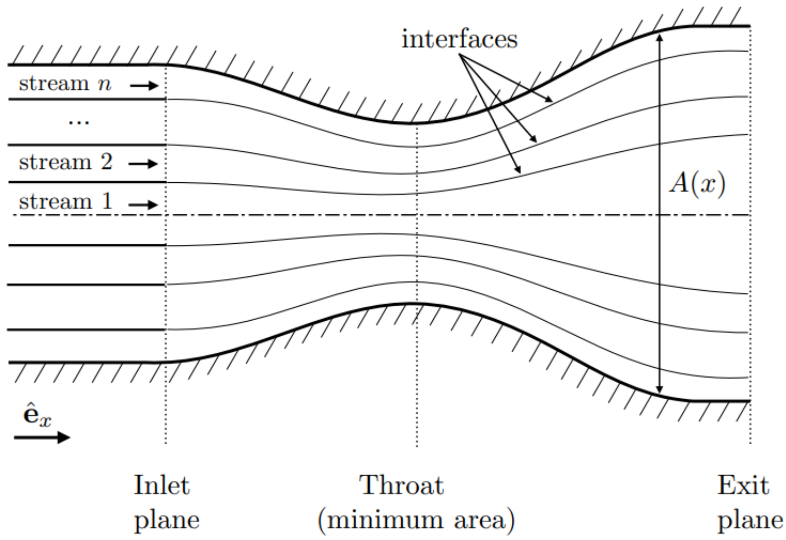

Figure B.1: Schematic of the compound-compressible nozzle flow [28]

The flow through the nozzle is divided into several parallel substreams with individual stagnation conditions and thermodynamic properties (γ, R). However, in this present case, all the streams are assumed to have identical thermodynamic properties. The general case of perfect gases with different thermodynamic properties is presented in [5].

The compound-choking theory states that for fixed inlet conditions and reducing the outlet pressure, there is a point where information cannot propagate upstream even if some individual streams are still subsonic, i.e. the flow is compound-choked. The main assumptions of the original compound-choking theory are :

1. The flow is one-dimensional, steady, adiabatic and isentropic.
2. Each flow stream is a perfect gas with constant thermodynamic properties.
3. There is no mixing between streams.
4. The static pressure is constant across all streams and only varies in the stream wise direction.

Compound-flow indicator

In comparison with the classical single-gas theory, which determines the choking condition according to the local Mach number, the compound-choking theory defines a *compound-flow indicator*, $\beta(x)$, as the choking criterion :

$$\beta(x) = \sum_{i=1}^{n} \frac{A_i(x)}{\gamma} \left(\frac{1}{M_i^2(x)} - 1 \right) \tag{B.1}$$

where $A_i(x)$ and $M_i(x)$ denote the local flow area and the local Mach number of the i^{th} stream, respectively. The flow regimes are divided as follows : $\beta > 0$, $\beta = 0$ and $\beta < 0$ corresponds to the so-called *compound-subsonic*, *compound-sonic* and *compound-supersonic* regime, respectively. A closer inspection of the equation leads to the conclusion that, when a compound flow is choked ($\beta = 0$), the individual stream Mach numbers will not necessarily be equal to one. Indeed, in the case of a flow involving two streams, one stream must be supersonic, yielding $1/M_i^2 < 1$, while the other must be subsonic, i.e $1/M_i^2 > 1$, to have $\beta = 0$.

Equivalent Mach number

As proposed by Hedges et al. [19], it is convenient to define an equivalent Mach number, $M_{eq}(x)$, such that

$$M_{eq}(x) = \left(\gamma \frac{\beta(x)}{A(x)} + 1 \right)^{-1/2} \tag{B.2}$$

where $A(x)$ is the local total flow area. This equivalent Mach number offers the advantage of being analogous with the Mach number in single-stream flows with regard to its interpretation. Indeed, M_{eq} will be the unity for compound-sonic flow ($\beta = 0$), less than unity for compound-subsonic flow ($\beta < 0$) and greater than unity for compound-sonic flow ($\beta < 0$).

Computational procedure

First, under the assumptions, the mass flow rate of the i^{th} stream may be written as a function of the local pressure $p(x)$ and the local flow area $A_i(x)$ only

$$\dot{m}_i = \frac{A_i(x)p_{0i}}{\sqrt{T_{0i}}}\left(\frac{p(x)}{p_{0i}}\right)^{\frac{1}{\gamma}}\sqrt{\frac{2}{R}\left(\frac{\gamma}{\gamma-1}\right)\left[1-\left(\frac{p(x)}{p_{0i}}\right)^{\frac{\gamma-1}{\gamma}}\right]} \tag{B.3}$$

Using the previous equation, and by isolating the flow area, the geometrical compatibility condition for two streams, i.e. $A_1(x)+A_2(x) = A(x)$, may be written at any point in the nozzle :

$$\begin{aligned}\frac{\dot{m}_2}{\dot{m}_1}\sqrt{\frac{T_{02}}{T_{01}}} =& \left\{\frac{A(x)}{A_1^*}\left[\left(\frac{2}{\gamma-1}\right)\left(\frac{\gamma+1}{2}\right)^{\frac{\gamma+1}{\gamma-1}}\right]^{1/2}\right.\\ &\left. - \left(\frac{p_{01}}{p(x)}\right)^{1/\gamma}\left[1-\left(\frac{p(x)}{p_{01}}\right)^{\frac{\gamma-1}{\gamma}}\right]^{-1/2}\right\}\\ &\times\left[1-\left(\frac{p(x)}{p_{02}}\right)^{\frac{\gamma-1}{\gamma}}\right]^{1/2}\left(\frac{p_{02}}{p_{01}}\right)\left(\frac{p(x)}{p_{02}}\right)^{1/\gamma}\end{aligned} \tag{B.4}$$

In our ejector case, the flow is assumed to be isentropic in the primary nozzle, A_1^* will be equal to the area of the throat of the primary nozzle, A_t. Hence, the primary mass flow rate $\dot{m}_1$, may be written as

$$\dot{m}_1 = \frac{A_t\ p_{01}}{\sqrt{T_{01}}}\sqrt{\frac{\gamma}{R}\left(\frac{\gamma+1}{2}\right)^{\frac{1+\gamma}{\gamma-1}}} \tag{B.5}$$

In both equation, all boundary condition are fixed, only the local pressure $p(x)$, and the secondary mass flow rate $\dot{m}_2$, are unknown. Under choked flow conditions (on-design), a second equation arises from the fact that the compound-flow indicator, $\beta(x)$, must fall to zero in the mixing duct of a supersonic ejector. Indeed, the flow is compound-choked and the cross-section of the mixing duct A_m, is identified as the geometrical throat of the compound-compressible nozzle flow, see Fig. B.1. By using the relation between the Mach number and the ratio of total to static pressure for an isentropic flow, i.e.,

$$M_i^2(x) = \frac{2}{\gamma - 1}\left[\left(\frac{p_{0i}}{p(x)}\right)^{\frac{\gamma-1}{\gamma}} - 1\right] \tag{B.6}$$

The choked condition ($\beta = 0$) may be rewritten as

$$\frac{\dot{m}_2}{\dot{m}_1}\sqrt{\frac{T_{02}}{T_{01}}} = \left(\frac{p_{02}}{p_{01}}\right)^{\frac{\gamma-1}{\gamma}} \frac{\left\{\frac{\gamma-1}{2}\left[\left(\frac{p^*_{eq}}{p_{01}}\right)^{\frac{1-\gamma}{\gamma}} - 1\right]^{-1} - 1\right\}\left[1 - \left(\frac{p^*_{eq}}{p_{02}}\right)^{\frac{\gamma-1}{\gamma}}\right]^{1/2}}{\left\{1 - \frac{\gamma-1}{2}\left[\left(\frac{p^*_{eq}}{p_{02}}\right)^{\frac{1-\gamma}{\gamma}} - 1\right]^{-1}\right\}\left[1 - \left(\frac{p^*_{eq}}{p_{01}}\right)^{\frac{\gamma-1}{\gamma}}\right]^{1/2}} \tag{B.7}$$

where p^*_{eq} represents the static pressure corresponding to compound-sonic regime. Finally, for a specified geometry configuration and boundary condition, the simultaneous resolution of these two independent equations provides the value of local pressure p^*_{eq}, and the value of the secondary mass flow rate $\dot{m}_2$, and therefore the entrainment ratio for the choked condition (on-design regime).

Appendix C

Precision estimation

A brief explanation regarding the error computation in transient simulation is described below. For further information about the error estimation, the reader could also refer to the research papers of Smirnov et al. [41].

The relative error S_i is presented as a result of the integration in the i^{th} direction and is proportional to the ratio of mean cell size (ΔL) to the domain size (L_i) in the same direction :

$$S_i \simeq \left(\frac{\Delta L}{L_i}\right)^{k+1} \tag{C.1}$$

For uniform grid, the error could be $S_i \simeq (1/N_i)^{k+1}$, where N_i is the number of cells in the direction of integration. The power k, depends on the accuracy of the scheme. In the present study, all the schemes used are second order accurate. In the multi-directional problems, the error is given by the summation of errors in all the direction.

$$S_{err} \simeq \sum_{i=1}^{3} S_i \tag{C.2}$$

Finally, the total accumulated error S_{err}^n after n time steps is proportional to the square root of the number of time steps at the end of the simulation :

$$S_{err}^n \simeq S_{err} \cdot \sqrt{n} \tag{C.3}$$

To ensure the CFD accuracy, this error should be less than a tolerance limit (S_L). As suggested by past researches [41, 7], the tolerance limit should be between 1% and 5%. Since the error is dependent on the number of time steps, there will be a limit on the maximum number of time steps for a particular simulation. The maximum number of time steps is given by :

$$n_{max} = \left(\frac{S_L}{S_{err}} \right)^2 \tag{C.4}$$

A last important characteristic for the results of transient simulations is the reliability (R_s). It's the ratio of the maximum allowable number of time steps and the actual number of time steps used at the end of simulation. This ratio shows that how far the maximum allowable error is from the actual error.

$$R_s = n_{max}/n \tag{C.5}$$

The higher is the ratio, the lower is the error. On tending R_s to unity, the error tends to the maximal allowable value.

Bibliography

[1] Ansys FLUENT 2021 - Theory guide, Ansys, Fluent , 15.0.

[2] R. Arun Kumar and G. Rajesh. Effect of Geometric Configurations on the Starting Transients in Vacuum Ejector. *AIAA Journal*, 57(7):2905–2922, July 2019. Publisher: American Institute of Aeronautics and Astronautics.

[3] Y. Bartosiewicz, Zine Aidoun, P. Desevaux, and Yves Mercadier. CFD-Experiments Integration in the Evaluation of Six Turbulence Models for Supersonic Ejectors Modeling. *Integrating CFD and Experiments Conference, Glasgow, UK*, 2003.

[4] Y. Bartosiewicz, Zine Aidoun, P. Desevaux, and Yves Mercadier. Numerical and experimental investigations on supersonic ejectors. *International Journal of Heat and Fluid Flow*, 26(1):56–70, February 2005.

[5] A. Bernstein, W. H. Heiser, and C. Hevenor. Compound-Compressible Nozzle Flow. *Journal of Applied Mechanics*, 34(3):548–554, September 1967.

[6] Giorgio Besagni, Nicolò Cristiani, Lorenzo Croci, Gaël Raymond Guédon, and Fabio Inzoli. Computational fluid-dynamics modelling of supersonic ejectors: Screening of modelling approaches, comprehensive validation and assessment of ejector component efficiencies. *Applied Thermal Engineering*, 186:116431, March 2021.

[7] V.B. Betelin, R.M. Shagaliev, S.V. Aksenov, I.M. Belyakov, Yu.N. Deryuguin, D.A. Korchazhkin, A.S. Kozelkov, V. Nikitin, A.V. Sarazov, and D.K. Zelenskiy. Mathematical simulation of hydrogen–oxygen combustion in rocket engines using LOGOS code. *Acta Astronautica*, 96:53–64, March 2014.

[8] Ghanshyam Bharate and Arun Kumar R. Starting transients in second throat vacuum ejectors for high altitude testing facilities. *Aerospace Science and Technology*, 113:106687, June 2021.

[9] WeiXiong Chen, Ming Liu, DaoTong Chong, JunJie Yan, Adrienne Blair Little, and Yann Bartosiewicz. A 1D model to predict ejector performance at critical and sub-critical operational regimes. *International Journal of Refrigeration*, 36(6):1750–1761, September 2013.

[10] Weixiong Chen, Chaoyin Shi, Shuangping Zhang, Huiqiang Chen, Daotong Chong, and Junjie Yan. Theoretical analysis of ejector refrigeration system performance under overall modes. *Applied Energy*, 185:2074–2084, January 2017.

[11] S. D. Clou, M. J. Brooks, W. Lear, S. Sherif, and E. Khalil. An Ejector Transient Performance Model for Application in a Pulse Refrigeration System. 2011.

[12] S. Croquer, S. Poncet, and Z. Aidoun. Turbulence modeling of a single-phase R134a supersonic ejector. Part 1: Numerical benchmark. *International Journal of Refrigeration*, 61:140–152, January 2016.

[13] Sergio Croquer, Yu Fang, Antoine Metsue, Yann Bartosiewicz, and Sébastien Poncet. Compound-choking theory for supersonic ejectors working with real gas. *Energy*, 227:120396, July 2021.

[14] Dianne DeTurris. Fabri Choking in a Two-Dimensional Reacting Flow Mixer-Ejector. In *48th AIAA Aerospace Sciences Meeting Including the New Horizons Forum and Aerospace Exposition*. American Institute of Aeronautics and Astronautics, 2010. _eprint: https://arc.aiaa.org/doi/pdf/10.2514/6.2010-384.

[15] J. Fabri and R. Siestrunck. Supersonic Air Ejectors. 1958.

[16] Jerzy Gagan, Kamil Smierciew, Dariusz Butrymowicz, and Jaroslaw Karwacki. Comparative study of turbulence models in application to gas ejectors. *International Journal of Thermal Sciences*, 78:9–15, April 2014.

[17] J. García del Valle, J. Sierra-Pallares, P. Garcia Carrascal, and F. Castro Ruiz. An experimental and computational study of the flow pattern in a refrigerant ejector. Validation of turbulence models and real-gas effects. *Applied Thermal Engineering*, 89:795–811, October 2015.

[18] Javier García del Valle, José M. Sáiz Jabardo, Francisco Castro Ruiz, and Julio San José Alonso. A one dimensional model for the determination of an ejector entrainment ratio. *International Journal of Refrigeration*, 35(4):772–784, June 2012.

[19] K. R. Hedges and P. G. Hill. Compressible Flow Ejectors: Part II—Flow Field Measurements and Analysis. *Journal of Fluids Engineering*, 96(3):282–288, September 1974.

[20] Amel Hemidi, François Henry, Sébastien Leclaire, Jean-Marie Seynhaeve, and Yann Bartosiewicz. CFD analysis of a supersonic air ejector. Part I: Experimental validation of single-phase and two-phase operation. *Applied Thermal Engineering*, 29(8):1523–1531, June 2009.

[21] HAROLD J. HOGE and RONALD A. SEGARS. Choked flow - A generalization of the concept and some experimental data. *AIAA Journal*, 3(12):2177–2183, 1965. Publisher: American Institute of Aeronautics and Astronautics _eprint: https://doi.org/10.2514/3.3343.

[22] B. J. Huang, J. M. Chang, C. P. Wang, and V. A. Petrenko. A 1-D analysis of ejector performance. *International Journal of Refrigeration*, 22(5):354–364, August 1999.

[23] Ali Jafarian, Mohammad Azizi, and Pezhman Forghani. Experimental and numerical investigation of transient phenomena in vacuum ejectors. *Energy*, 102:528–536, May 2016.

[24] S. K. Karthick, Srisha M. V. Rao, G. Jagadeesh, and K. P. J. Reddy. Experimental parametric studies on the performance and mixing characteristics of a low area ratio rectangular supersonic gaseous ejector by varying the secondary flow rate. *Energy*, 161:832–845, October 2018.

[25] J. H. Keenan and E. P. Neumann. A Simple Air Ejector. *Journal of Applied Mechanics*, 9(2):A75–A81, 1942.

[26] J. H. Keenan, E. P. Neumann, and F. Lustwerk. An Investigation of Ejector Design by Analysis and Experiment. *Journal of Applied Mechanics*, 17(3):299–309, 1950.

[27] Olivier Lamberts, Philippe Chatelain, and Yann Bartosiewicz. Numerical and experimental evidence of the Fabri-choking in a supersonic ejector. *International Journal of Heat and Fluid Flow*, 69:194–209, February 2018.

[28] Olivier Lamberts, Philippe Chatelain, Nicolas Bourgeois, and Yann Bartosiewicz. The compound-choking theory as an explanation of the entrainment limitation in supersonic ejectors. *Energy*, 158:524–536, September 2018.

[29] Bartosiewicz Y. Lamberts O. and P. Chatelain. Chocking and mixing phenomena in supersonic ejectors. 2018.

[30] W.E. Lear, S.A. Sherif, and G.M. Parker. Effect of Fabri choking on the performance of two-phase jet pumps. In *Collection of Technical Papers. 35th Intersociety Energy Conversion Engineering Conference and Exhibit (IECEC) (Cat. No.00CH37022)*, volume 2, pages 1190–1197 vol.2, July 2000.

[31] V Lijo, H D Kim, G Rajesh, and T Setoguchi. Numerical simulation of transient flows in a vacuum ejector-diffuser system. *Proceedings of the Institution of Mechanical Engineers, Part G: Journal of Aerospace Engineering*, 224(7):777–786, July 2010. Publisher: IMECHE.

[32] Federico Mazzelli, Adrienne B. Little, Srinivas Garimella, and Yann Bartosiewicz. Computational and experimental analysis of supersonic air ejector: Turbulence modeling and assessment of 3D effects. *International Journal of Heat and Fluid Flow*, 56:305–316, December 2015.

[33] J. Munday and D. Bagster. A New Ejector Theory Applied to Steam Jet Refrigeration. 1977.

[34] Byung Hoon Park, Ji Hyung Lee, and Woongsup Yoon. Studies on the starting transient of a straight cylindrical supersonic exhaust diffuser: Effects of diffuser length and pre-evacuation state. *International Journal of Heat and Fluid Flow*, 29(5):1369–1379, October 2008.

[35] H. Pearson, J. B. Holliday, and S. F. Smith. A Theory of the Cylindrical Ejector Supersonic Propelling Nozzle. *The Aeronautical Journal*, 62(574):746–751, 1958. Publisher: Cambridge University Press.

[36] Andrija Petrovic, Milos Z. Jovanovic, Srbislav Genic, Ugljesa Bugaric, and Boris Delibasic. Evaluating performances of 1-D models to predict variable area supersonic gas ejector performances. *Energy*, 163:270–289, November 2018.

[37] K. Pianthong, W. Seehanam, M. Behnia, T. Sriveerakul, and S. Aphornratana. Investigation and improvement of ejector refrigeration system using computational fluid dynamics technique. *Energy Conversion and Management*, 48(9):2556–2564, September 2007.

[38] Natthawut Ruangtrakoon, Tongchana Thongtip, Satha Aphornratana, and Thanarath Sriveerakul. CFD simulation on the effect of primary nozzle geometries for a steam ejector in refrigeration cycle. *International Journal of Thermal Sciences*, 63:133–145, January 2013.

[39] Navid Sharifi and Masoud Boroomand. An investigation of thermo-compressor design by analysis and experiment: Part 1. Validation of the numerical method. *Energy Conversion and Management*, 69:217–227, May 2013.

[40] Chaoyin Shi, Huiqiang Chen, Weixiong Chen, Shuangping Zhang, Daotong Chong, and Junjie Yan. 1D Model to Predict Ejector Performance at Critical and Sub-critical Operation in the Refrigeration System. *Energy Procedia*, 75:1477–1483, August 2015.

[41] N. N. Smirnov, V. B. Betelin, V. F. Nikitin, L. I. Stamov, and D. I. Altoukhov. Accumulation of errors in numerical simulations of chemically reacting gas dynamics. *Acta Astronautica*, 117:338–355, December 2015.

[42] T. Sriveerakul, S. Aphornratana, and K. Chunnanond. Performance prediction of steam ejector using computational fluid dynamics: Part 1. Validation of the CFD results. *International Journal of Thermal Sciences*, 46(8):812–822, August 2007.

[43] Szabolcs Varga, Armando C. Oliveira, and Bogdan Diaconu. Influence of geometrical factors on steam ejector performance – A numerical assessment. *International Journal of Refrigeration*, 32(7):1694–1701, November 2009.

[44] M. T. Zegenhagen and F. Ziegler. A one-dimensional model of a jet-ejector in critical double choking operation with R134a as a refrigerant including real gas effects. *International Journal of Refrigeration*, 55:72–84, July 2015.

[45] Yinhai Zhu, Wenjian Cai, Changyun Wen, and Yanzhong Li. Numerical investigation of geometry parameters for design of high performance ejectors. *Applied Thermal Engineering*, 29(5):898–905, April 2009.

UNIVERSITÉ CATHOLIQUE DE LOUVAIN
École polytechnique de Louvain
Rue Archimède, 1 bte L6.11.01, 1348 Louvain-la-Neuve, Belgique | **www.uclouvain.be/epl**